

MOLECULAR DYNAMICS SIMULATION OF NANO-INDENTATION  
PROCESS OF SILICON: EFFECTS OF INITIAL TEMPERATURE AND  
GRAIN SIZE

A Thesis  
Submitted to the Graduate Faculty  
of the  
North Dakota State University  
of Agriculture and Applied Science

By

Yachao Wang

In Partial Fulfillment of the Requirements  
for the Degree of  
MASTER OF SCIENCE

Major Department:  
Industrial and Manufacturing Engineering

March 2014

Fargo, North Dakota

# North Dakota State University

## Graduate School

---

**Title**

MOLECULAR DYNAMICS SIMULATION OF  
NANO-INDENTATION PROCESS OF SILICON: EFFECTS OF  
INITIAL TEMPERATURE AND GRAIN SIZE

---

**By**

Yachao Wang

---

The Supervisory Committee certifies that this *disquisition* complies with North  
Dakota State University's regulations and meets the accepted standards for the degree  
of

**MASTER OF SCIENCE**

SUPERVISORY COMMITTEE:

Jing Shi

---

Chair

Xinnan Wang

---

David Wells

---

Val Marinov

---

Fardad Azarmi

---

Approved:

04/14/2014

---

Date

Canan Bilen-Green

---

Department Chair

## ABSTRACT

In this study, a comprehensive investigation on nano-scale indentation of monocrystal and polycrystalline silicon is carried out by adopting molecular dynamic (MD) simulation. Five levels of initial temperature (30K, 100K, 300K, 500K and 700K) are configured in this study and the simulation results reveal the amount of  $\beta$ -5 silicon atoms at the maximum indentation position is not significantly affected by the initial temperature, substantially less  $\beta$ -silicon atoms are observed with higher temperatures. The temperature effect on the unloading process is also discussed.

Meanwhile, indentation force curves for polycrystalline silicon (grain size ranging from 6.45 nm to 20.48 nm) and single crystalline silicon is compared. The result shows that the normal Hall-Petch effect is not seen in the nano-indentation process of silicon. The grain boundary increases local stress during the indentation process and results in less formation of  $\beta$ -silicon phase, but it hardly affects the formation of  $\beta$ -5 silicon.

## ACKNOWLEDGEMENTS

This work is for my parents, my friends, for their unconditional love, support and encouragement.

I am very thankful to my major advisor, Dr. Jing Shi, for his long-term guidance and help, understanding, and support throughout this study. I gained a lot from him especially through his questions and suggestions regarding my research work.

I want to thank my Co-advisor, Dr. Xinnan Wang, for his guidance, help and support for my research throughout these years. I am also grateful for the access to the equipment in his laboratory.

I appreciate Dr. David L. Wells for his valuable suggestions and questions on my thesis paper and his continuous support throughout my degree. Meanwhile, I appreciate Dr. Fardad Azarmi and Dr. Val R. Marinov for serving on my supervisory committee.

I also want to acknowledge the Center for Computationally Assisted Science and Technology (CCAST) of NDSU, for generously providing me hardware and software resource for my research over the years.

# TABLE OF CONTENTS

ABSTRACT.....	iii
ACKNOWLEDGEMENTS.....	iv
LIST OF TABLES.....	viii
LIST OF FIGURES.....	ix
CHAPTER 1. PROBLEM STATEMENT.....	1
1.1. Background.....	1
1.2. Problem definition.....	3
CHAPTER 2. LITERATURE REVIEW.....	7
2.1. Stress induced phase transformation of silicon.....	7
2.2. Grain size effect on material properties.....	10
2.2.1. Hall-Petch relation.....	11
2.2.2. Inverse Hall-Petch relation.....	12
2.4. MD simulation and its applications.....	16
2.4.1. MD simulation in nano-indentation of silicon.....	16
2.4.2. MD simulation in nano-machining of silicon.....	19
CHAPTER 3. MOLECULAR DYNAMICS SIMULATION MODEL.....	22
3.1. Energy calculation.....	23
3.1.1. Potential energy function.....	23
3.1.2. Kinetic energy and temperature modelling.....	24
3.1.3. Temperature control.....	26

3.3. MD simulation model and parameter selection .....	26
3.3.1. General model construction .....	27
3.3.2. MD model for indentation of polycrystalline indentation .....	31
3.3.3. Simulation cases details .....	33
3.4. Indentation force and stress calculation .....	33
3.5. Indenter/workpiece interface stress distribution .....	34
3.6. Procedures of MD simulation of nano-indentation process .....	36
3.7. Software package .....	37
CHAPTER 4. NANO-INDENTATION EXPERIMENT VERIFICATION .....	39
4.1. Brief introduction of AFM .....	39
4.2. Experimental preparation and real-size MD simulation .....	40
4.3. Comparison between experiment and MD simulation model .....	42
CHAPTER 5. TEMPERATURE EFFECT ON NANO-INDENTATION OF MONOCRYSTALLINE SILICON .....	46
5.1. Phase transformation during nano-indentation process .....	46
5.2. Equivalent stress distribution during nano-indentation .....	50
5.3. Temperature distribution .....	53
5.4. Temperature effect on phase transformation .....	55
5.5. Temperature effect on stress distribution on indenter/workpiece interface .....	63
5.6. Temperature effect on unloading process .....	65
CHAPTER 6. GRAIN SIZE EFFECT ON NANO-INDENTATION OF POLYCRYSTALLINE SILICON .....	72

6.1. Effect of grain size on indentation force.....	73
6.2. Effect of grain size on equivalent stress .....	76
6.3. Effect of grain size on phase transformation .....	78
6.4. Grain size effect on stress distribution on indenter/workpiece interface.....	84
6.5. Grain size effect on unloading process .....	86
CHAPTER 7. CONCLUSIONS AND FUTURE RESEARCH .....	89
7.1. Conclusions.....	89
7.2. Future research.....	92
REFERENCES .....	94

## LIST OF TABLES

<u>Table</u>	<u>Page</u>
3.1. Tersoff parameters for atom interactions in silicon indentation by diamond tools (Tersoff, 1986; Tersoff, 1988) .....	31
3.2. Nano-indentation parameters for all simulation cases .....	33
6.1. Structural information for polycrystalline copper workpieces .....	72

## LIST OF FIGURES

<u>Figure</u>	<u>Page</u>
2.1. Flattening of the original tetrahedron diamond cubic structure during indentation, (a) tetrahedron before indentation, (b) during indentation and (c) at maximum indentation. (Cheong & Zhang, 2000).....	8
2.2. Atomic structures of (a) $\beta$ -silicon, and (b) bct-5 silicon (Zhang et al., 2012).....	8
2.3. Predicted yield stress for nano-structured copper as a function of grain size based on Hall-Petch and modified Hall-Petch relations (Mohammadabadi & Dehghani, 2008) .....	13
2.4. Relative motion of atoms in grain boundaries during 0.4% deformation of copper with the average grain size of 5.2 nm (green atoms move up, red atoms move down) (Schjøtz et al., 1998).....	15
2.5. Maximum normal stress and von Mises stress as a function of grain size for tensile process of tantalum obtained by MD simulation. (Tang et al., 2013).....	15
2.6. Silicon phase transformation (a) at maximum indentation, atoms beneath the indenter (circled by the dotted line) have a crystalline order different from that of the original diamond cubic structure; (b) crystalline to amorphous transition upon unloading (Cheong & Zhang, 2000).....	17
2.7. Effect of crystal anisotropy on phase transformation in nano-indentation (a) nanoindentation on Si (100) surface (b) nanoindentation on Si (111) surface.....	18
2.8. Distribution frequency of interatomic bond length in undeformed silicon workpiece material in chip formation zone at different cutting distances (Cai et al., 2007).....	19
2.9. Si-I to amorphous phase transition during nano-machining process (a) with negative rake angle (b) with positive rake angle. (Wang & Shi, 2013) .....	21
3.1. Schematic of MD simulation model constriction.....	27

3.2. Periodic boundary conditions. The center box (white) is shown along with its first periodic images. The circle round green color atom is of radius $l_{box}/2$ while the box encompasses the nearest periodic image of each of the other molecules (Cheung, 2002).....	29
3.3. Schematic of Voronoi polygons .....	32
3.4. Schematic of MD simulation model for indentation of polycrystalline silicon (grain size 20.48nm).....	32
3.5. Atom grouping for stress distribution analysis along the indenter/work interface .	35
3.6. Flow diagram of MD simulation for nano-indentation process .....	37
4.1. Schematic of AFM scanning .....	40
4.2. AFM nano-indentation experimental set-up.....	41
4.3. MD simulation model for AFM nano-indentation verification.....	42
4.4. AFM nano-indentation and cross section analysis .....	43
4.5. Comparison of cross-section profile for MD simulation and AFM scanning: (a) AFM nano-indentation made at 25 $\mu$ N, (b) cross section analysis comparison of AFM and MD nano-indentation.....	45
4.6. Force with respect to residual indent depth for MD simulation and AFM nano-indentation experiment .....	45
5.1. Three side cross-sectional views of phase transformation distribution at indentation depths of (a) 28 Å, (b) 50 Å, (c) 77 Å and (d) the corresponding top cross-sectional view ss' .....	47
5.2. Phase transformation evolution with respect to indentation stress for 300K initial temperature.....	49
5.3. Phase transformation comparison for various initial temperatures (data is taken at indentation stress of 13 GPa).....	50

5.4. Three side cross-sectional views of equivalent stress distribution at indentation depths of (a) 28 Å, (b) 50 Å, (c) 77 Å, as well as (d) one top cross-sectional view at the depth of 77 Å .....	52
5.5. Temperature distributions at the maximum indentation depth at the initial temperatures of (a) 30K, (b) 100K, (c) 300K, (d) 500K, and (e) 700K .....	53
5.6. Indentation force evolution at different initial temperatures .....	56
5.7. Number of atoms with bct-5 silicon phase structure with respect to indentation depth .....	57
5.8. Stress distribution at indentation depth of 40.5 Å for the initial temperatures of (a) 30K and (b) 700K .....	57
5.9. Number of atoms with β-silicon phase structure vs. indentation depth .....	58
5.10. Phase transformation distribution at the maximum indentation depth at the initial temperatures of (a) 30K (b) 100K (c) 300K (d) 500K and (e) 700K .....	60
5.11. Equivalent stress distributions at the maximum indentation depth at the initial temperatures of (a) 30K (b) 100K (c) 300K (d) 500K and (e) 700K .....	62
5.12. Temperature effect on the normal force distribution on indenter/workpiece interface .....	64
5.13. Temperature effect on the tangential force distribution on indenter/workpiece interface .....	65
5.14. Indentation force with respect to retraction distance during the unloading process with respect to the initial temperature .....	66
5.15. Number of atoms with bct-5 silicon phase structure with respect to indenter retraction distance.....	68
5.16. Number of atoms with β-silicon phase structure with respect to indenter retraction distance.....	68

5.17. Residual indentation morphologies and phase transformation distributions at the initial temperatures of (a) 30K, (b) 100K, (c) 300K, (d) 500K, and (e) 700K ..	70
6.1. Indentation force with respect to indentation depth for different grain sizes .....	75
6.2. Maximum indentation force with respect to grain size .....	75
6.3. Equivalent stress distributions in indentation polycrystalline silicon with different grain sizes: (a) 20.48nm (b) 12.9nm (c) 10.24nm (d) 7.81nm and (e) 6.45nm.....	77
6.4. Phase transformation in indentation process of polycrystalline silicon workpieces with different grain sizes, (a) 20.48nm, (b) 12.9nm, (c) 10.24nm, (d) 7.81nm, and (e) 6.45nm *Red color indicates bct-5 atoms and green color indicates $\beta$ -silicon atoms. ....	79
6.5. Effect of grain size on the formation of bct-5 silicon during loading .....	81
6.6. Effect of grain size on the formation of $\beta$ -silicon atoms during loading.....	81
6.7. Comparison of equivalent stress distributions for (a) polycrystalline silicon with grain size of 20.48 nm (b) monocrystalline silicon .....	83
6.8. Grain size effect on the normal force distribution on the indenter/workpiece interface .....	85
6.9. Grain size effect on the tangential force distribution on the indenter/workpiece interface .....	85
6.10. Indentation force vs. depth during unloading process with respect to different grain size.....	86
6.11. Effect of grain size on the formation of bct-5 silicon during unloading .....	87
6.12. Effect of grain size on the formation of $\beta$ -silicon during unloading .....	87

# CHAPTER 1. PROBLEM STATEMENT

## 1.1. Background

Nanomaterial is defined as any particle smaller than 100 nm in at least one dimension. Compared with bulk materials at macro level, nanomaterials have some unique properties such high purity, significant surface and interfacial effects, resulting in drastic difference in mechanical/chemical properties. For example, the hardness of single crystalline copper nanoparticles smaller than 50 nm are at least 50 times higher, and do not exhibit the same malleability and ductility as the bulk copper (Qian et al., 2005). The yield strength of silver at nano scale is 12 times higher than that at macro scale (Leach et al., 2007). Bulk gold and platinum are non-magnetic but at the nano size they act as magnetic particles (Kim et al., 2006). Nanomaterials also have unconventional optical properties as they are small enough to confine their electrons and produce quantum effects. Gold particles exhibit red color at the dimension of 10-20 nm, while they exhibit yellow color with the size of 2-5 nm (Nath et al., 2002). Extensive research about nanomaterials has been carried out for a few decades. Due to the outstanding and distinct mechanical/chemical properties, nanomaterials have been widely adopted in a variety of applications, including next-generation computer chips, better insulation materials, tougher and harder cutting tools, high-sensitivity sensors, aerospace components, and so forth.

Meanwhile, silicon (Si) material carries significant importance for commercial applications and scientific research in medical, semiconductor, and sustainable energy industries. For instance, silicon is a fundamental material for MEMS (Micro Electric Mechanical System) devices. As such, the mechanical and physical property of silicon could have significant effect on the performance of components. Meanwhile, the deformation, phase transformation, and failure mechanism of silicon at micro/nano scales alter the properties of produced silicon components. This relationship indicates that Si material processing at smaller scales needs to be thoroughly studied.

Nano-indentation is a useful technique to determine material mechanical properties at small scales by driving an indenter with a known geometry into the specimen. With the advancement of manufacturing technologies as well as the increasing application of MEMS or NEMS devices, the size of many precision parts and the thickness of thin films in semiconductor components are being continuously reduced. Also, more complicated nano-indentation instruments are needed to achieve the precise measurement of material properties. At micro and nano scales, MD simulation is an effective tool in studying various complex phenomena during the indentation process, such as material phase transformation, dislocation occurrence and propagation, tool/work interaction stress distribution in material, all of which used to be challenging for experimental study or conventional simulation method (e.g., finite element analysis).

## 1.2. Problem definition

In this research, two key unsolved problems in the nano-indentation process are addressed: (1) temperature effect on the formation and evolution of different Si phases; (2) how the grain size of polycrystalline silicon affects its mechanical properties and phase transformation.

First, temperature is an important consideration in various manufacturing processes because it brings significant changes to materials properties and deformation mechanism. It is well known that many manufacturing processes are carried out within tailored temperature ranges, such as the adoption of high temperature to deform metals to reduce loading requirement and improve forming limit (Okonkwo et al., 2012), and ultra-low temperature in machining to facilitate the chip removal and improve the surface integrity properties (Shi et al., 2004). More examples include laser assisted machining for difficult-to-machine materials such as ceramics where the laser beam is used to preheat the material before the machine tool engages it (Sun et al., 2010); cryogenic abrasive jet machining of materials to improve the machining efficiency (Gradeen et al., 2012; Urbanovich et al., 1992). Temperature also significantly affects the properties and manufacturing processes of silicon. For instance, the electricity resistance of silicon under pressure is found to be dependent on the environmental temperature (Salehpour et al., 2006). Thermal conductivity of silicon nanowire (SiNW) is found to be dependent on temperature in the range of 0-600K (Donadio, 2010). High temperature of 1580K is

helpful in producing oxygen-containing single crystal silicon (Misiuk, 2000). Very limited number of studies in literature investigates the effect of temperature on silicon phase transformation. For example, Khayyat et al. (2003) perform Raman microscopy scanning of residual silicon indentations that are made at room temperature and 77K. No Si-III is found from the residual indentations made at 77K, but Si-III is found from the indentation made at room temperature. Similarly, another Raman scanning study discovers that higher temperatures increase the formation of Si-III/XII phase (Ruffell et al., 2009).

On the other hand, stress induced phase transformation widely exists in many deformation, loading/unloading, and manufacturing processes. Therefore, it is considered as an important cause of physical/chemical property change of material, especially for brittle materials. To our best knowledge, the scarce existing studies that investigate the effect of temperature on silicon phase transformation only focus on the spectrum analysis of residual indentation. The approach is not capable of revealing the dynamic evolution of complex phase transformation within material during the indentation process. The research gap motivates this thesis research.

Meanwhile, the existing studies on MD simulation of nano-scale indentation usually adopt the defect-free monocrystalline. The most popular ones have been monocrystal copper, aluminum, and silicon. Nevertheless, the vast majority of engineering materials exist in polycrystalline (instead of monocrystalline) forms. It is not

difficult to understand that indenting polycrystalline structures may yield different results compared with indenting monocrystalline structures. The same reason is applicable for other more complex manufacturing processes such as machining, scratching, and etching. The effect of grain size and grain boundary on material mechanical properties has been well discussed for many metal materials. Usually, the well-known Hall-Petch relationship is widely accepted. This relationship indicates that material strength increases with the decrease of grain size. However, for very fine nano-structured materials, this relationship may no longer hold. The critical grain size for the maximum material strength of copper is extensively reported as 10-15 nm. However, to our best knowledge, most of existing research about grain size effect on mechanical property is for metals, while similar investigation for non-metal brittle material has not been performed. Meanwhile, there is distinct difference between the deformation mechanisms of ductile and brittle materials. In the case of machining, as revealed by Shi (2006), the phase transition observed in the silicon cutting process is the distinguishing difference between silicon machining and copper machining. Due to the above reasons, investigating the grain size effect of brittle material in nano-indentation process is meaningful.

Besides, the tool/material interaction during nano-indentation also provides important insights for other manufacturing process, such as machining and scratching. The intriguing issue of phase transformation, tribological behavior along indenter/work material interface in nano-indentation process can be directly adopted to reveal the

interface between the cutting tool and work material in machining process (Wang and Shi, 2013). Therefore, nano-indentation provides a simple and convenient way to investigate the fundamental issues related to complicated nano-manufacturing processes.

## CHAPTER 2. LITERATURE REVIEW

### 2.1. Stress induced phase transformation of silicon

Monocrystalline silicon owns a diamond cubic crystalline structure under ambient pressure and room temperature. When the diamond cubic silicon is subject to elevated hydrostatic pressures, it transforms into other phases with different crystalline structures. To date, there are a total of twelve different structures phases reported under varying hydrostatic pressures. At 11-15 GPa, the first phase transformation occurs from diamond cubic (Si-I) to intermediate metastable tetragonal body-centered structure Si-II ( $\beta$ -silicon), while  $\beta$ -silicon often diminishes during the loading release process (Jamieson, 1963; Hu et al., 1986; Khayyat, 2003; Gridneva et al., 1972). The Si-I to Si-II transformation leads to a significant increase of electrical conductivity and a volume decrease of 22%. Note that Si-II can also be formed at the lower pressure of about 8.5 GPa in the presence of shear pressure. At higher hydrostatic pressures, five other phases can be identified, namely, Si-XI, Si-V, Si-VI, and Si-VII (Hu et al., 1986). Si-III (bc8, body-centered-cubic structure) and Si-XII (R8, rhombohedra structure) are formed during slow pressure release, while two tetragonal polymorphs, Si-VII and Si-IX as well as amorphous silicon are formed instead during rapid pressure release (Crain et al., 1994; Crain et al, 1994; Pfrommer et al., 1997). Among all above-mentioned phases of silicon, Si-II ( $\beta$ -silicon) and bct-5 silicon are the most frequently observed in nano-indentation process of crystalline silicon. Cheong and Zhang (2000) indicate that the change from diamond

cubic Si-I silicon to Si-II ( $\beta$ -silicon) when subject to load is due to the flattening of the tetrahedron structure in diamond cubic silicon, as presented in Figure 2.1. Diamond cubic silicon is four-fold coordinated with all of the four neighbors at distance of 2.35 Å. Bct-5 silicon has five-fold coordination structure with one neighbor atom at the distance of 2.31 Å and other four at 2.44 Å.  $\beta$ -silicon is six-fold coordinated with four nearest neighbors at the distance of 2.42 Å and two at the slightly larger distance of 2.57 Å, as shown in Figure 2.2.

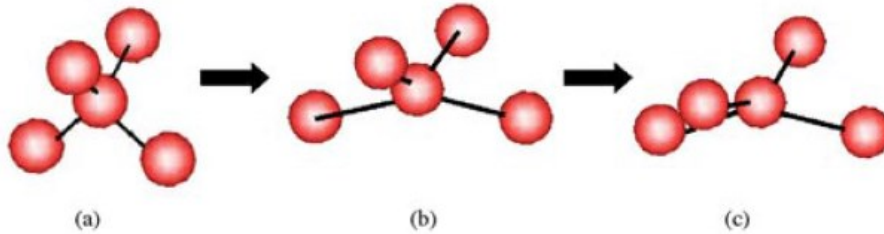


Figure 2.1. Flattening of the original tetrahedron diamond cubic structure during indentation, (a) tetrahedron before indentation, (b) during indentation and (c) at maximum indentation. (Cheong & Zhang, 2000)

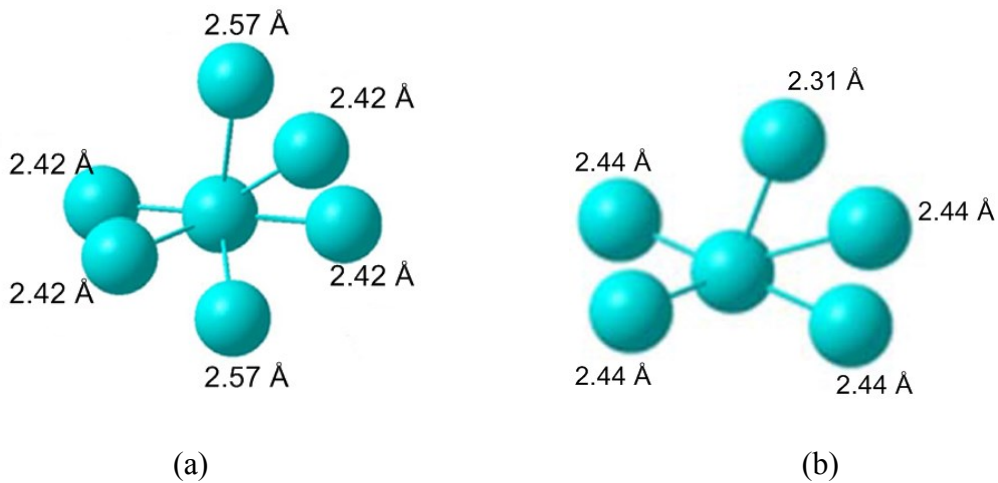


Figure 2.2. Atomic structures of (a)  $\beta$ -silicon, and (b) bct-5 silicon (Zhang et al., 2012)

Phase transformation of silicon in nano-manufacturing is a critical phenomenon, which determines the silicon material properties and performance during service. In literature, many experimental investigations have been carried out. Crain et al. (1994) report the reversible pressure-induced structural transition between metastable phases of silicon by using X-ray diffraction technique. Hu and Spain (1984) report the phase transformation evolution of silicon at pressure up to 25 GPa. Kunz et al. (1995) adopt cross-sectional transmission electron microscopy (XTEM) to investigate the nanocrystalline silicon aggregates imbedded in a predominantly amorphous silicon layer. It is observed that the crystalline-to-amorphous phase transition may be caused by photoelectron stimulated hydrogen desorption. Bradby et al. (2000) use XTEM to study the phase transformation process of spherical indentation. It is found that the silicon material undergoes different phase transformation processes when subject to different indentation loads. Raman micro-spectroscopy is applied to obtain two-dimensional distribution of the residual phase transformation, which exhibits strong anisotropic characteristic (Gerbig et al., 2011). Similarly, with the aid of Raman micro-spectroscopy, the relationship between residual stress and residual phase transformation is discussed for indentation process (Gerbig et al., 2010). However, at very small scales such as nano-scale, the traditional experimental methods only provide limited information about the phase transformation of silicon. In other words, the formation and evolution of

various phases of silicon under elevated hydrostatic pressures could not be effectively analyzed by the means of the above-mentioned experimental approaches. As such, in this study, we apply molecular dynamics (MD) simulation to study this issue in nano-indentation.

## **2.2. Grain size effect on material properties**

The effect of grain size and grain boundary on material properties has been well discussed. Yang and Vehoff (2007) investigate the dependency of hardness upon grain size in nano-indentation experiments. With the indentation depth of less than 100 nm, it is revealed that the local interaction between dislocations and grain boundaries causes various hardness dependences on indentation depth. Zhang et al. (2004) carry out nano-indentation experiments on copper with grain sizes from 10 to 200 nm. It is found that at short dwell-times, the hardness increases significantly with the decreasing grain size. However, the difference substantially diminishes at longer times due to the rapid grain growth under the indenter. Similar reverse proportion relations between grain size and hardness are observed in indentation experiments at micro-scale in literature. Li and Reece (2000) discover that grain size has a significant effect on surface fatigue behavior, and increasing grain size reduces the threshold for crack nucleation. Also, Lim and Chaudhri (2002) show that in the grain size range of 15-520  $\mu\text{m}$ , the initial higher dislocation density for smaller grains is believed to cause higher Vickers hardness. More

importantly, the rapid advance of numerical simulation techniques has enabled more detailed analysis of dislocations and grain boundaries in deformation of polycrystalline.

### **2.2.1. Hall-Petch relation**

The influence of grain boundary on material properties can be significant, but it depends on the exact conditions of deformation and the particular material used. In the following, we intend to explain the change of indentation forces with respect to grain size in the indentation of polycrystalline coppers. Usually, the strength of polycrystalline materials is expected to increase if the grain size decreases. For coarse-grain materials, the grain size effect on flow stress can be captured by the empirical Hall-Petch relation, which suggests that the yield stress increases with decreasing grain size by following:

$$\sigma = \sigma_0 + K / \sqrt{d} \quad (2.1)$$

where  $\sigma_0$  is the yield stress,  $K$  is the Hall-Petch slope, and  $d$  is the grain size. The Hall-Petch strengthening is also called grain boundary strengthening, and it is a popular method of strengthening materials by changing the average grain size. It is usually explained as a mechanism that the grain boundaries impede the movement and propagation of dislocations inside material. Also, the number of dislocations within a grain has an effect on how easily dislocations can transverse grain boundaries and propagates from one grain to another. As a result, the dislocation movement and material yield strength could be affected with a different grain size.

### 2.2.2. Inverse Hall-Petch relation

In recent years, it has been discovered that when the grain size of nano-structured materials is smaller than a critical value, the Hall-Petch relation could be inversed (Lu & Sui, 1993; Schiøtz & Jacobsen, 2003; Koch, 2003). In other words, as the fraction of grain boundary atoms increases to a significant level, work softening becomes dominant. The inverse Hall-Petch relation indicates that the a smaller grain size increases the volume fraction of grain boundary, which facilitates the activation of other deformation mechanisms such as grain boundary sliding, and thereby lowers the material strength. Mohammadabadi and Dehghani (2008) develop a modified Hall-Petch equation, which incorporates the negative slope observed between grain size and yield stress. It is in the following form,

$$\sigma = \sigma_0 + K / \sqrt{d} - \sigma_{in} f_{gb} \quad (2.2)$$

where  $\sigma_{in}$  is internal stress along grain boundary that depends on parameters such as grain boundary thickness, lattice distortions and grain size,  $f_{gb}$  is the volume fraction of grain boundary. Figure 2.3 shows that the yield stress of polycrystalline copper is a function of grain size for both the conventional and modified Hall-Petch relations. It can be seen that if the conventional Hall-Petch relation is followed, the yield stress should increase exponentially with the grain size reduction. However, the modified Hall-Petch relation indicates that with the decrease of grain size, the yield stress grows at a slower pace to its peak position when the grain size is around 14 nm, and then it starts to drop if the grain

size is below this critical value. Note that there are also other literature reporting that for some metals, the critical grain size for the inverse Hall-Petch to take over is about 10-15nm (Schiøtz & Jacobsen, 2003; Schiøtz, 2004; Sanders et al., 1997; Schuh & Nieh, 2002).

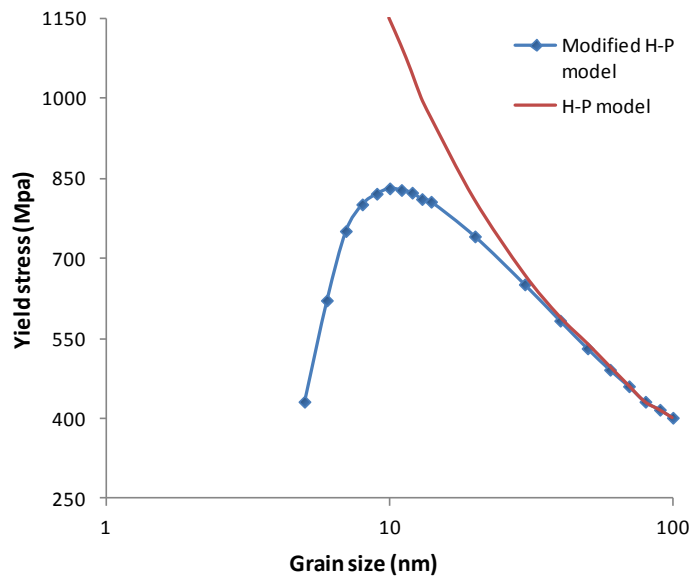


Figure 2.3. Predicted yield stress for nano-structured copper as a function of grain size based on Hall-Petch and modified Hall-Petch relations (Mohammadabadi & Dehghani, 2008)

A few other studies also show that the flow stress of ultrafine nano-structured materials can decrease as a result of the grain size reduction. With the inverse Hall-Petch effect, the deformation is no longer dominated by dislocation motion, while atomic sliding in grain boundaries starts to play the major role (Morris, 2001). Narayan (2004) experimentally studies this phenomenon by using pulsed laser deposition to produce nano-crystalline materials. It is discovered that when the copper nanocrystal is less than

10 nm, material hardness decreases with the decrease of grain size. The decrease in slope of Hall-Petch curve and eventually the decrease in hardness below a certain grain size can be explained by a model of grain-boundary sliding (Wei & Anand, 2004). Because of this, as the grain size decreases from 61 to 30 nm, the overall material strength increases, but further decrease in the grain size may result in a decrease of strength.

More importantly, the rapid advance of numerical simulation techniques has enabled more detailed analysis of dislocations and grain boundaries in deformation of polycrystallines. With the aid of MD simulation technique, the grain-boundary sliding theory is supported by researchers (Van & Derlet, 2001; Schiøtz et al., 1998), where the small and independent slip events in the grain boundary are seen in the uniaxial tension deformation process of fcc metal with very small grain size (less than 12 nm). As shown in Figure 2.4. Tang et al. (2013) firstly perform MD simulation to demonstrate the transition of regular Hall-Petch to inverse Hall-Petch relationship in the tensile process of Tantalum. The dependence of maximum von Mises stress on grain size is plotted in Figure 2.5.

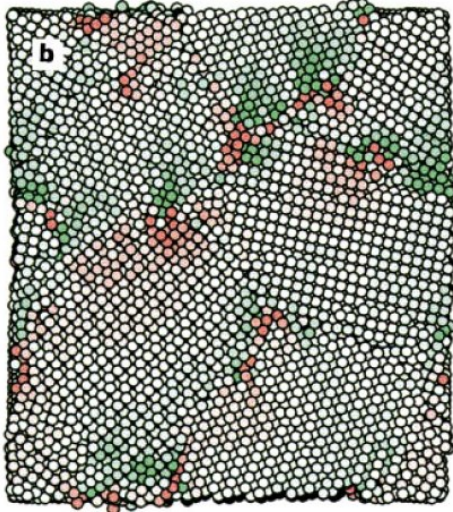


Figure 2.4. Relative motion of atoms in grain boundaries during 0.4% deformation of copper with the average grain size of 5.2 nm (green atoms move up, red atoms move down) (Schjøtz et al., 1998)

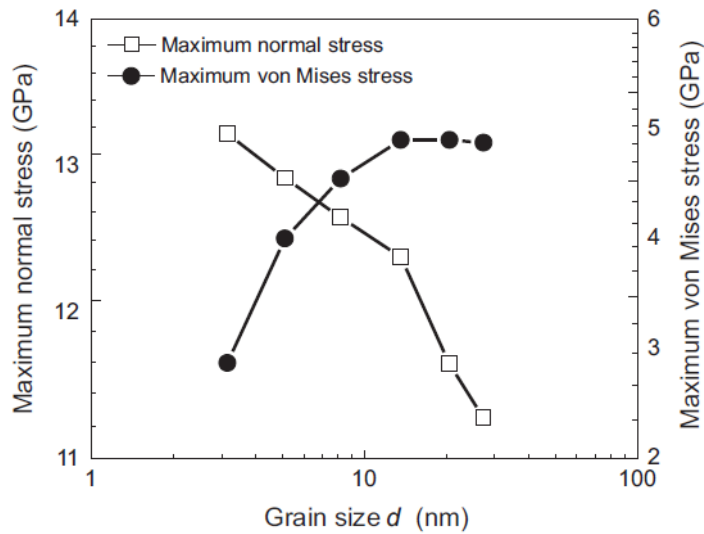


Figure 2.5. Maximum normal stress and von Mises stress as a function of grain size for tensile process of tantalum obtained by MD simulation. (Tang et al., 2013)

The interaction of dislocations with the  $\Sigma=5(210)[001]$  grain boundary is analyzed, and the transmission of dislocation across the grain boundary is observed (Jang & Farkas, 2007). Another MD simulation study indicates that compared to bulk diamond

crystal, substitution energies are found to be significantly lower for grain boundaries (Zapol et al., 2001).

## **2.4. MD simulation and its applications**

Molecular dynamics (MD) simulation is widely applied in studying various complex, dynamic processes that occur from atomistic level to submicron level. MD simulation is based on solving the equation of motion of particles in a multi-body system, and its statistical mechanics is able to link microscopic simulations and macroscopic properties of materials. MD simulation was firstly performed to study the interaction of hard spheres by Alder and Wainwright early in 1957. The subsequent major breakthrough of MD simulation was made in 1964, when a realistic potential was applied in the simulation for liquid argon (Rahman, 1964). Realistic potential for water was firstly applied by Stillinger and Rahman in 1974 (Stillinger & Rahman, 1974). To date, MD simulation is suitable for variety of systems, including simple atomic structures, isolated molecules, molecular liquids, proteins, DNA and polymers.

### **2.4.1. MD simulation in nano-indentation of silicon**

Many MD simulation studies can be found in literature on phase transformation of silicon alone. The pioneering MD simulation work performed by Cheong and Zhang (2000) shows that diamond cubic silicon transforms into  $\beta$ -silicon upon loading of

indentation process, as shown in Figure 2.6. It is also found that the body-centered tetragonal silicon transforms to amorphous phase during unloading and this transition is reversible by conducting the second indentation.

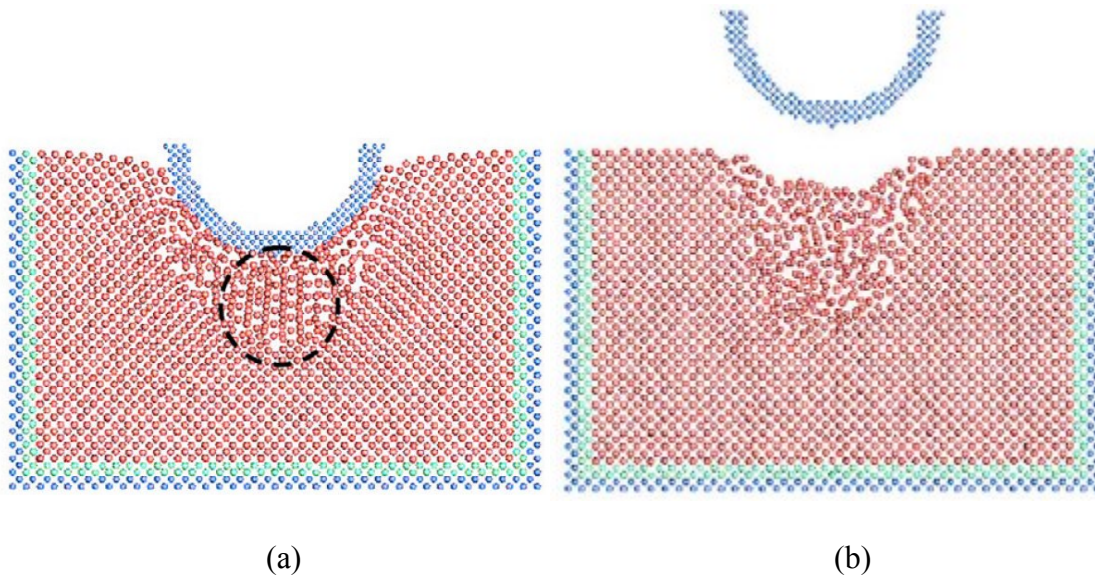


Figure 2.6. Silicon phase transformation (a) at maximum indentation, atoms beneath the indenter (circled by the dotted line) have a crystalline order different from that of the original diamond cubic structure; (b) crystalline to amorphous transition upon unloading (Cheong & Zhang, 2000)

Tang and Zhang (2005) study the effect of water on the phase transformation during nano-indentation process, and find that the presence of water leads to the formation of more  $\beta$ -silicon. In the work of Kim and Oh (2006), the effect of crystal anisotropy on phase transformation in nano-indentation is investigated. The anisotropic behavior of structural phase transformation, depending upon the crystallographic orientation, is observed as shown in Figure 2.7.

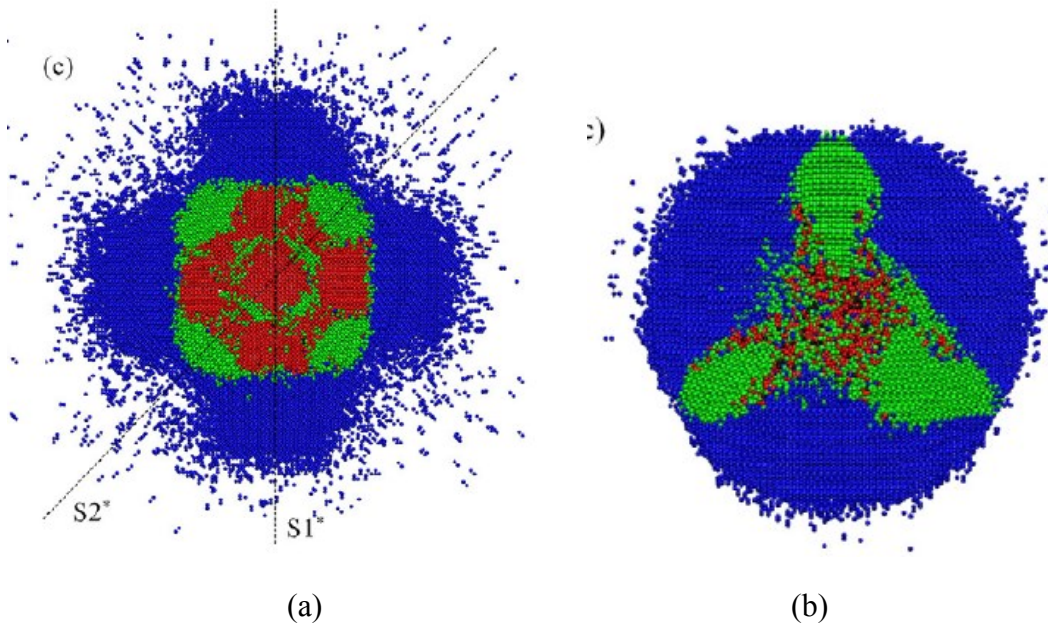


Figure 2.7. Effect of crystal anisotropy on phase transformation in nano-indentation (a) nanoindentation on Si (100) surface (b) nanoindentation on Si (111) surface.

\*Red color indicates Si-II ( $\beta$ -silicon), Green color indicates bct-5 Si. (Kim & Oh, 2006)

Mylvaganam et al. (2009) discover a new six coordinated silicon phase, namely, Si-XIII that transforms directly from Si-I during nano-indentation, as well as a distorted diamond structure (DDS) silicon upon unloading. It also observed that during unloading, the size of DDS increases as the tip radius increases. Lin et al. (2007) simulate the nano-indentation process with spherical (radius 5nm) and Berkovich indenters. It is discovered that the distributions of phase transformation induced by Berkovich indenter and spherical indenter are similar.

#### 2.4.2. MD simulation in nano-machining of silicon

Phase transformations of silicon are also extensively discussed in other more complex tool-based manufacturing process (e.g., machining and sliding), by using MD simulation. For example, the nano-scale cutting simulation conducted by (Tang and Chen, 2006) shows that diamond cubic phase transforms to  $\beta$ -silicon upon loading due to the localized high pressure and temperature, and this phase transformation prevents the formation of dislocation. Mylvaganam and Zhang (2012) confirm that the stable bct-5 silicon phase could be produced in the subsurface by nano-scratching and the resistance of bct-5 silicon to indentation is higher than amorphous silicon while lower than diamond silicon. The phase transformation makes machining of brittle silicon in ductile mode possible. Fang et al. (2007) discover that the silicon chips have amorphous structure in ductile mode cutting and polycrystalline structure in brittle mode cutting.

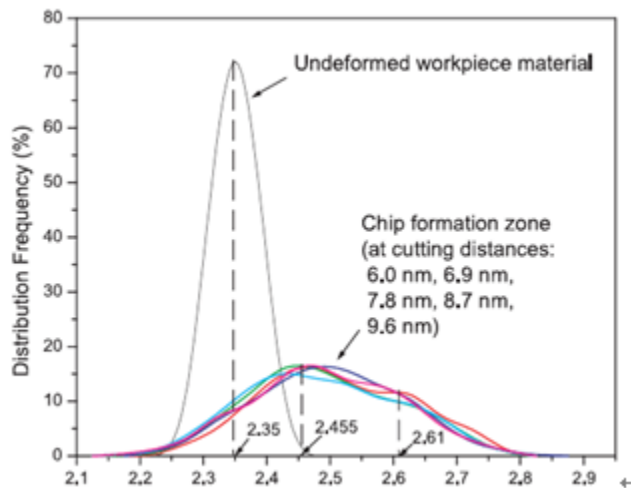


Figure 2.8. Distribution frequency of interatomic bond length in undeformed silicon workpiece material in chip formation zone at different cutting distances (Cai et al., 2007)

Cai et al. (2007) adopt the radial distribution function to analyze phase transition in the nano-machining process of silicon, as presented in Figure 2.8. It is found that with the increase of the tool edge radius, the decrease of shear stress around the cutting edge is observed and finally the transition of cutting chip from ductile to brittle starts to occur. In another study (Cai et al., 2007), the same group of researchers confirms the existence of “dynamic hard particles” in the chip formation zone, as a result of monocrystalline to amorphous phase transformation of silicon. Zhang and Tanaka (1998) employ MD simulation to study the deformation of silicon in two-body and three-body sliding processes, and confirm that the dominate phenomenon in this process is the Si-I to amorphous transformation. Han et al. (2009) apply MD simulation to study the phase transformation in nano-scratching process. The high hydrostatic pressure is believed to be the reason of breaking up ideal chemical bond interactions, and this in turn drives the transition of classical silicon-I to metallic  $\beta$ -silicon. Wang and Shi (2013) simulate the nano-cutting process of silicon. It is revealed that negative rake angle produces deeper layer of amorphous silicon in machined surface associated more compressive surface residual stress, as shown in Figure 2.9.

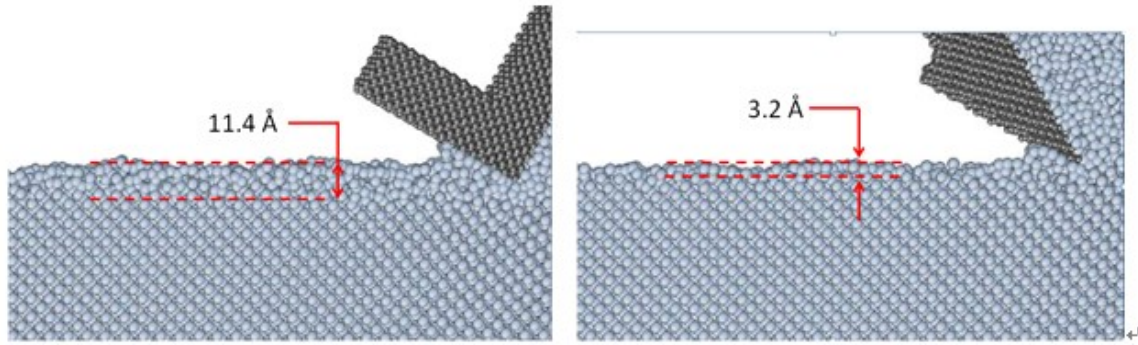


Figure 2.9. Si-I to amorphous phase transition during nano-machining process (a) with negative rake angle (b) with positive rake angle. (Wang & Shi, 2013)

### **CHAPTER 3. MOLECULAR DYNAMICS SIMULATION MODEL**

MD simulation calculates the motion of each individual molecule in the modelling of solids, liquids and gas. More specifically, MD simulation makes precise estimation of atoms condition with dynamic manner as it calculates atoms velocity, positions, accelerations and motion direction over the simulation process. MD simulation is able to provide essentially the exact results for statistical mechanics problems which can only be solved by other approximate methods.

MD simulation is usually carried out in the following steps. First, the initial positions of particles or atoms are specified to the simulation box. These particles interact via potential, which determines the extent to which simulation results represent the system of interest. Second, by applying the second Newton's law:  $F_I = m_i a_i$ , the particles move around in the simulation box, and their new positions are updated every preset interval. Third, the physical quantities or property are measured as functions of particle positions and status. These instantaneous measurements are then interpreted to equilibrium properties via statistical mechanics, whose basic theory is that a macroscopic property of a system is an average of the overall possible quantum states of that property. Therefore, the macroscopic property of a system can be calculated by taking the average of measurements in MD simulation.

### **3.1. Energy calculation**

Energy is the most important consideration in all MD simulations. In MD simulation, generally two types of energy are considered, kinetic energy and potential energy, the total energy of MD simulation is the summation of kinetic energy and potential energy of all atoms. The transition between potential energy and kinetic energy is always calculated in the MD simulation process.

#### **3.1.1. Potential energy function**

Potential energy refers to the energy at each atomic site as a continuous function of positions of all surrounding atoms (Schaible, 1999). A specific potential energy must be selected to perform intermolecular energy calculation before conducting MD simulation. The potential is able to calculate interatomic force with continuous change of atom positions. The atomic force can be either attractive or repulsive depending on the distance between the two involved atoms. Repulsive force is dominant when atomic distance is short while attractive force becomes dominant for long-ranged atoms. The atomic force can be neglected when the distance becomes too far, and the distance at where interaction is neglected is so called the cut-off distance.

Until now, there is no potential that is able to describe atomic interactions for all types of materials. Different potentials functions are developed for different types of materials, according to the physical and chemical properties of materials. Generally

potential energy functions are classified into two categories, namely pair-potential function and multi-body potential function. The general model for total energy as the function of atomic positions is the resemblance to the Taylor expansion:

$$U(\mathbf{r}^N) = \sum_i u(r_i) + \sum_i \sum_{j>i} u(r_i, r_j) + \sum_i \sum_{j>i} \sum_{k>j} u(r_i, r_j, r_k) + \dots \quad (3.1)$$

where  $\mathbf{r}^N = (r_1, r_2, \dots, r_N)$  stands for the complete set of  $3N$  particle coordinates,  $u(r_i)$  represents the effect of an external field (including the container walls),  $u(r_i, r_j)$  represents pairwise interactions, and  $u(r_i, r_j, r_k)$  represents three-body interactions. Most applications consider only pairwise interactions, since their contribution is the most significant. The potential energy is then written as

$$U(\mathbf{r}^N) = \sum_i \sum_{j>i} u(r_{ij}) \quad (3.2)$$

Besides the pairwise or three-body potential functions, there are four-body or more multi-body potential energy functions for describing material atomic interactions. However, it should be noted that when more bodies-functions are used in MD simulation model, more computational resources are required. Due to this reason, researchers need to compromise between the computational efficiency and simulation accuracy.

### 3.1.2. Kinetic energy and temperature modelling

Total kinetic energy is the summation of kinetic energy of all related atoms in the simulation system. The follow equation is used in calculating kinetic energy:

$$KE = \sum_1^N \frac{1}{2} m v_i^2 \quad (3.3)$$

where  $N$  is the numbers of atoms,  $m$  is the atom mass and  $v$  is the atom velocity. The system temperature and local temperature are decided by the kinetic energy. Note that the kinetic energy changes in the local area and the entire system is helpful for investigating heat generation during the simulation process.

The system and local temperature is determined by the kinetic energy of the simulation system, in another words, the temperature control of the entire simulation system or any parts of the simulation system can be achieved by scaling the atom velocities. The simulation system is always assumed to be in an environment with a constant temperature, such as the room temperature of 300K. Certain functions are introduced to maintain the temperature around constant value. The relationship between temperature and atom velocity is expressed as following:

$$\langle K \rangle = \left\langle \frac{1}{2} m v^2 \right\rangle = \frac{3}{2} k T \quad (3.4)$$

where  $k$  is the Boltzmann's constant with value of  $1.38 \times 10^{-23}$  J/K. This equation is suitable for any cluster of atoms in thermal equilibrium. The system temperature or local temperature can be derived from kinetic energy. Heat generation and distribution can be modeled by understanding kinetic energy changes in the system.

### 3.1.3. Temperature control

Thermostat is often applied to a specific group of atoms to help maintain the MD simulation system temperature around a desired range. In another words, atoms in the thermostat group aim to stabilize the temperature of entire simulation box by transferring heat to outer space. As such, temperature control for the atoms thermostat group is important and this is done by scaling the atom velocities to desired temperature. The function is given below:

$$V_{new} = V_{original} \sqrt{\frac{fNKT}{\sum_1^N mv_i^2}} \quad (3.5)$$

where  $V_{original}$  is the velocity of the atom to be scaled,  $V_{new}$  is scaled velocity,  $N$  is number of atoms,  $f$  is degree of freedom for the system,  $K$  is Boltzmann's constant, and  $T$  is desired temperature. Note that Equation (3.5) is actually derived from Equation (3.4).

Based on the temperature calculation method, with the desired initial temperature  $T_c$ , the initial condition of an atom is defined by giving its velocity:

$$v = \sqrt{3k_B T_c / m} \quad (3.6)$$

### 3.3. MD simulation model and parameter selection

In this study, the MD simulation model for nano-indentation, the single crystal silicon has the dimension of  $400 \times 300 \times 300 \text{ \AA}^3$ , which contains around 1,800,000 atoms, and the hemispherical diamond indenter has a radius of  $100 \text{ \AA}$ , which contains around

100,000 atoms. In the simulation of monocrystal silicon indentation, the indentation is made on the (100) plane of silicon.

### 3.3.1. General model construction

The schematic of the base MD simulation model (i.e., single crystalline silicon) is shown in Figure 3.1.

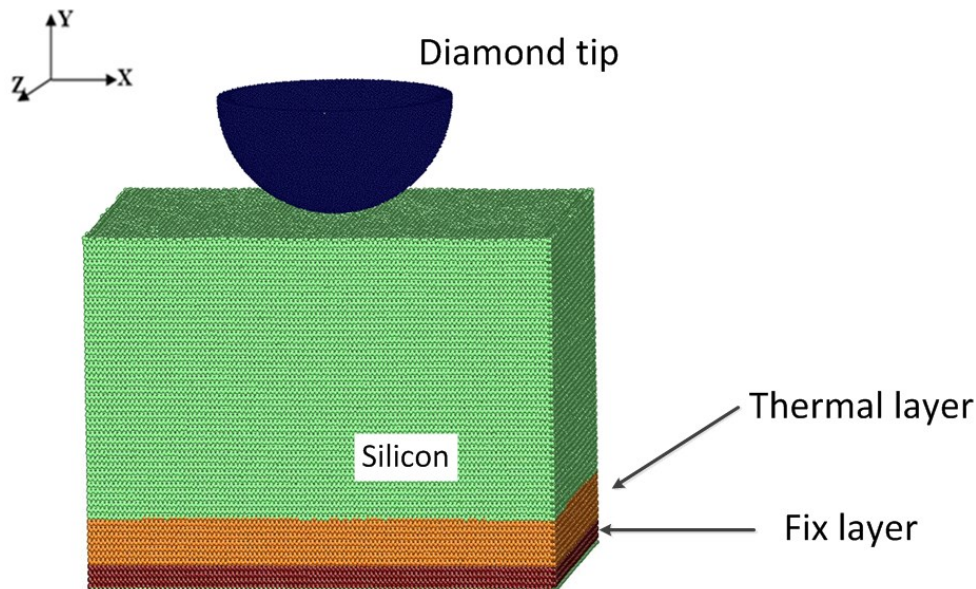


Figure 3.1. Schematic of MD simulation model construction

There are two special layers within the silicon workpiece, namely, thermal layer and fix layer. The fix layer acts as a base thus avoids the displacement of silicon workpiece during the indentation process. The atoms in the thermal layer are configured with a constant temperature so that they are able to constantly absorb heat generated by material deformation and dissipate the heat to outer space. Due to the fact that the

workpiece in this simulation system is very small compared to practical nanoindentation experiments, and significant boundary effect could make the overall simulation results biased. In an attempt to solve this problem, periodic boundary conditions are applied along X and Z direction so that the simulation box is replicated throughout the space to form an infinite lattice. The semi-sphere indenter is set as perfectly rigid so it does not deform during the indentation. The periodic boundary conditions are widely applied to mitigate spurious size effect when investigating behavior of isolated system. The basic assumption of periodic boundary conditions is that each atom interacts with the nearest atom image in the periodic array. In another words, the supercell is surrounded by infinite replicates and periodic images of itself. During the simulation, not only the atoms in original simulation box, but also the atoms in the surrounding replicated boxes should be considered. Figure 3.2 illustrates the concept of periodic boundary conditions. By adopting periodic boundary conditions, the simulation box is viewed as a small part of a much bigger system. As such, the boundary effects due to fixed boundary condition can be mitigated.

Tersoff potential is used in this study to describe the interaction between the silicon atoms in the work material. First proposed by Tershoff (Tersoff, 1986), this potential energy formulation is capable of predicting behaviors of stable phases of diamond cubic silicon and body-centred tetragonal  $\beta$ -silicon, and has become widely

adopted to study the properties and deformation behaviors of silicon in MD simulation (Ohira et al., 1994; Cheong & Zhang, 2000; Moura & Amaral, 2005).

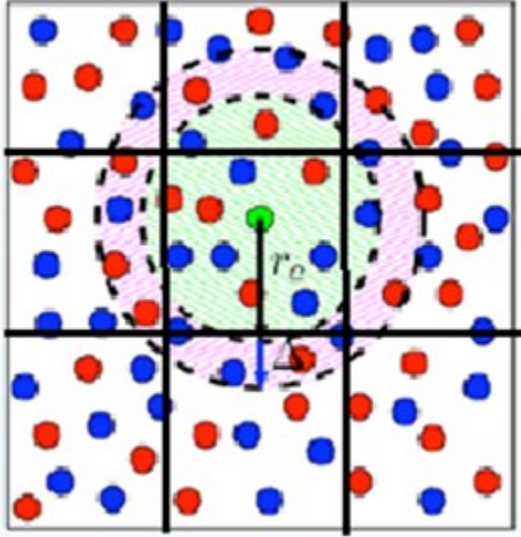


Figure 3.2. Periodic boundary conditions. The center box (white) is shown along with its first periodic images. The circle round green color atom is of radius  $l_{box}/2$  while the box encompasses the nearest periodic image of each of the other molecules (Cheung, 2002).

Based on the concept of bond order, the bond strength is determined by where the electronic charge is sitting in covalent bonding rather than by the coordination of the atoms. The Tersoff potential model for the interactions between atoms can be expressed as follows:

$$E = \sum_i E_i = \frac{1}{2} \sum_{i \neq j} V_{ij} \quad (3.7)$$

$$V_{ij} = f_c(r_{ij}) [f_R(r_{ij}) + b_{ij} f_A(r_{ij})] \quad (3.8)$$

$$f_R(r_{ij}) = A_{ij} \exp(-\lambda_{ij} r_{ij}) \quad (3.9)$$

$$f_A(r_{ij}) = -B_{ij} \exp(-\mu_{ij} r_{ij}) \quad (3.10)$$

$$f_C(r_{ij}) = \begin{cases} 1.0, & r_{ij} < R_{ij} \\ \frac{1}{2} + \frac{1}{2} \cos \left[ \frac{\pi(r_{ij}-R_{ij})}{(S_{ij}-R_{ij})} \right], & R_{ij} < r_{ij} < S_{ij} \\ 0.0, & r_{ij} > S_{ij} \end{cases} \quad (3.11)$$

$$b_{ij} = \left( 1 + \beta_{ij}^{n_{ij}} \zeta_{ij}^{n_{ij}} \right)^{-1/2n_{ij}} \quad (3.12)$$

$$\zeta_{ij} = \sum_{k \neq i, j} f_C(r_{ik}) g(\theta_{ijk}) \quad (3.13)$$

$$g(\theta_{ijk}) = 1 + \frac{c_i^2}{d_i^2} - \frac{c_i^2}{[d_i^2 + (h_i - \cos \theta_{ijk})^2]} \quad (3.14)$$

In the above equations,  $E$  stands for the total energy of the system, namely, the summation of the all the  $i$ th site energy  $E_i$ .  $f_R$  and  $f_A$  represent the repulsive pair potential and attractive pair potential respectively.  $f_C$  is the cut-off function.  $b_{ij}$  is the bond order parameter, which reflects the multi-body characteristics of this potential.  $\zeta_{ij}$  is the number of effective coordination. Only the first shell of neighbors is included by introducing  $R$  and  $S$ . The bond angle between bond  $ij$  and  $ik$  is expressed by  $\theta_{ijk}$ , and  $r_{ij}$  is the distance between atoms. Other arguments are fitting parameters.

Since Tersoff potential is a three-body potential function that explicitly includes an angular contribution of the force, three elements must be mapped in each entry, which includes all the potential parameters. Thus, an entry for Si-C-C means a Si atom bonded to a C atom with another C atom influencing the bond. In general, the parameters for Si-C-Si and Si-Si-C entries are not the same. Thus, in this study, 8 entries (for Si-Si-Si, Si-Si-C, Si-C-Si, Si-C-C, C-Si-Si, C-Si-C, C-C-Si, C-C-C) must be contained in order to specify all permutations of the two elements interacting in three-body configurations.

Detailed parameters are summarized in Table 3.1.

Table 3.1. Tersoff parameters for atom interactions in silicon indentation by diamond tools (Tersoff, 1986; Tersoff, 1988)

Parameters	Unit	C-C-C	Si-Si-Si	Si-Si-C	Si-C-C	C-Si-Si	C-Si-C	C-C-Si	Si-C-Si
$c_i$		38049	100390	100390	100390	38049	38049	38049	100390
$d_i$		4.3484	16.217	16.217	16.217	4.3484	4.3484	4.3484	16.217
$h_i$		-0.57058	-0.59852	-0.59825	-0.59825	-0.57058	-0.57058	-0.57058	-0.59825
$n_{ij}$		0.72751	0.7873	0	0.787340	0.72751	0	0	0
$\beta_{ij}$		$1.5724 \times 10^{-7}$	$1.1 \times 10^{-6}$	0	$1.1 \times 10^{-6}$	$1.5724 \times 10^{-7}$	0	0	0
$\mu_{ij}$	$\text{\AA}^{-1}$	2.2119	1.73222	0	1.97205	1.97205	0	0	0
$B_{ij}$	$eV$	346.7	471.18	0	395.126	395.126	0	0	0
$R_{ij}$	$\text{\AA}$	1.95	2.85	2.36	2.36	2.36	1.95	2.36	2.85
$S_{ij}$	$\text{\AA}$	0.15	0.15	0.15	0.15	0.15	0.15	0.15	0.15
$\lambda_{ij}$	$\text{\AA}^{-1}$	3.4879	2.4799	0	2.9839	2.9839	0	0	0
$A_{ij}$	$eV$	1393.6	1830.8	0	1597.311	1597.311	0	0	0

### 3.3.2. MD model for indentation of polycrystalline indentation

The MD model for polycrystalline silicon is constructed based on Voronoi scheme. The basic step of constructing polycrystalline silicon model is described as follows. First, seeds are put down in the mono-crystalline silicon workpiece, associated with each seed there is a rotation matrix with random direction. Secondly, a copy of original mono-crystalline (assumed to infinite replicated) is rotated about the seed. Thirdly, material is cut out by the Voronoi polygon around these seeds and finally pasted together. A simple schematic of Voronoi Diagram is shown in Figure 3.3. Note that these seeds can take ordered positions, such as fcc (face centered cubic) arrangement, in which case grains with rhombic dodecahedron shape can be obtained, or bcc (body centered cubic) arrangement, in which case grains have truncated octahedron shape. In this study, all polycrystalline silicon models are constructed by defining seeds as fcc arranged, so the

grains have rhombic dodecahedron shape. The “Voronoirized” polycrystalline silicon model with a grain size of 20.48 nm is shown in Figure 3.4.

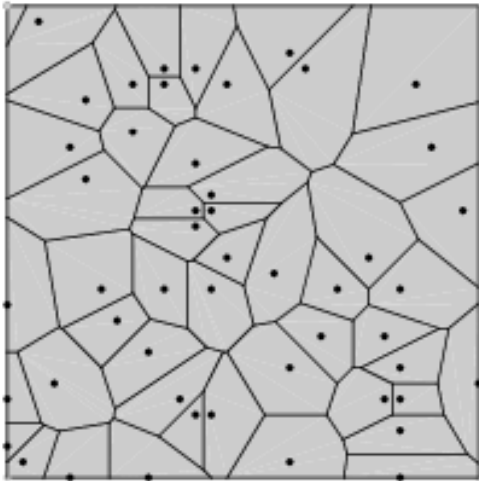


Figure 3.3. Schematic of Voronoi polygons

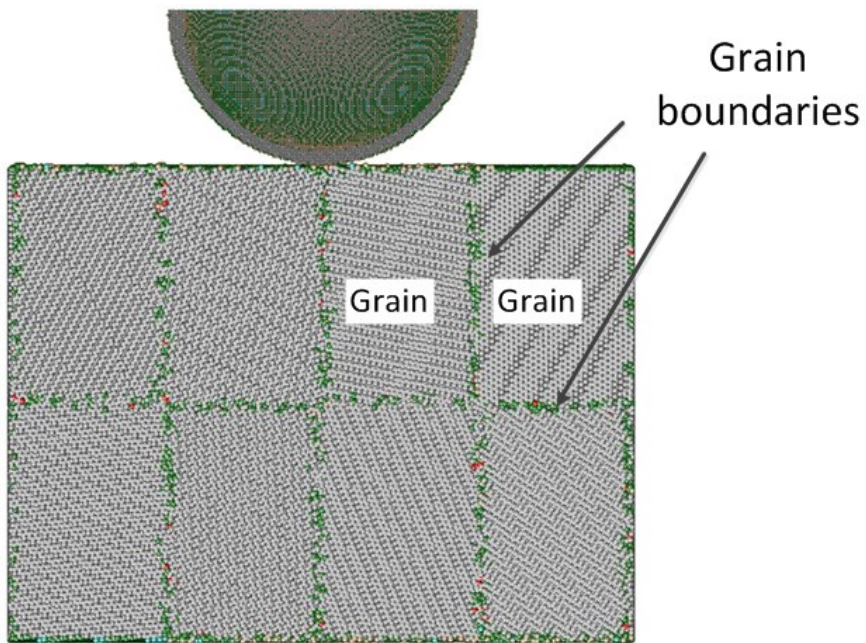


Figure 3.4. Schematic of MD simulation model for indentation of polycrystalline silicon (grain size 20.48nm)

### 3.3.3. Simulation cases details

A total of ten cases with different grain sizes and temperature conditions are simulated to study the effects of these parameters. The detailed simulation parameters are presented in Table 3.2. Each simulation case takes about 50 hours to finish by 50 computation nodes of Intel i7 Quad-Core processors.

Table 3.2. Nano-indentation parameters for all simulation cases

Case	Temperature	Grain size (nm)	Indentation depth (nm)
1	30K	monocrystal	8
2	100K	monocrystal	8
3	300K	monocrystal	8
4	500K	monocrystal	8
5	700K	monocrystal	8
6	300K	20.48	8
7	300K	12.9	8
8	300K	10.24	8
9	300K	7.81	8
10	300K	6.45	8

### 3.4. Indentation force and stress calculation

Indentation force is calculated by summing up the forces acting on every carbon atoms in the indenter, the forces of neighbor atoms of specific atom are also summed,

$$F = \sum_{i=1}^{N_r} \sum_j f_{ij} \quad (3.15)$$

$$f_{ij} = \frac{\partial U(r_{ij})}{\partial r_{ij}} \quad (3.16)$$

where  $N_T$  is the number of carbon atoms in the diamond indenter, and  $f_{ij}$  is the individual interaction force from atom  $j$  acting on atom  $i$ .

The investigation of stress distribution inside material is important in that it provides the insight of characteristics such as deformation mechanism or phase transition of material subject to loading. It also provides information about material yield prediction under processing. Meanwhile, finite scale materials should not be considered as continuum and the conventional continuum mechanics theorem does not hold true in MD simulation (Zhang & Tanaka, 1999).

Each of the stress components  $S_{xx}$ ,  $S_{yy}$ ,  $S_{zz}$ ,  $S_{xy}$ ,  $S_{xz}$ , and  $S_{yz}$  of each atom is calculated during the indentation process.  $\chi$  represents the virial stress components of each atom:

$$\chi = \frac{1}{\Omega} \sum_i^N (m_i v_i \otimes v_i + \frac{1}{2} \sum_{i \neq j} r_{ij} \otimes f_{ij}) \quad (3.17)$$

where  $\Omega$  is the volume domain within the cut-off distance of atom  $i$ ,  $v_i$  is the velocity of atom  $i$ , the sign  $\otimes$  means the tensor product of vectors, and  $N$  is the total number of atoms in the domain. In addition, the equivalent stress can be calculated by following equation:

$$S = \sqrt{3(S_{xy}^2 + S_{yz}^2 + S_{xz}^2) + \frac{1}{2}[(S_{xx} - S_{yy})^2 + (S_{xx} - S_{zz})^2 + (S_{yy} - S_{zz})^2]} \quad (3.18)$$

### 3.5. Indenter/workpiece interface stress distribution

To investigate the effect of temperature and grain size on the tribology performance of indenter/workpiece interface, the normal force and tangential force distributions along the indenter/work material interface are obtained. As shown in Figure 3.5, a thin surface layer of the indenter is considered, and the atoms in this layer are

evenly divided into 8 groups. Each group contains about 1,300 carbon atoms and the force acting on each atom group is individually computed. Note that each group is identical, so the groups have the same contact area. As such, the force distributions along the indenter/work material interface are actually equivalent to the stress distributions.

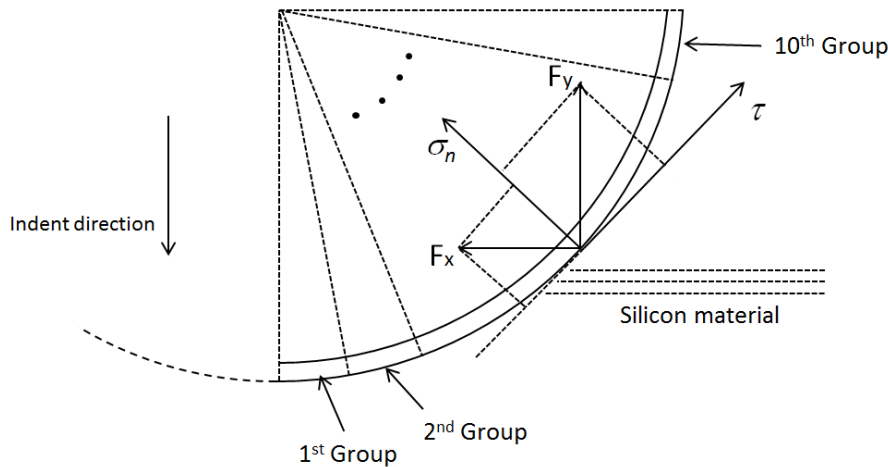


Figure 3.5. Atom grouping for stress distribution analysis along the indenter/work interface

The tangential force  $\tau$  and the normal force  $\sigma_n$  acting on each group is calculated by the following equation,

$$\sigma_n = F_y \cos \alpha + F_x \sin \alpha \quad (3.19)$$

$$\tau = F_y \sin \alpha + F_x \cos \alpha \quad (3.20)$$

where  $F_x$  and  $F_y$  are the average horizontal and vertical force components of each group.

### **3.6. Procedures of MD simulation of nano-indentation process**

There are three major phases of the simulation work, namely initialization, production, and post-analysis. Figure 3.5 shows the simulation flow diagram of the nano-indentation process.

In the initialization process, initial atom positions and velocities and other parameters are assigned at time step 0. The initial atom positions for indenter and workpiece are always set according to their molecular structures (e.g., crystalline diamond and silicon). The initial velocities follow Maxwell-Boltzmann distribution based on initial temperatures and then scaled to desired temperature by applying Equation (3.6). Then the simulation system relaxes from the initial position and velocity since all the system parameters are set artificially and there is a need to achieve equilibrium state. In the production state, the indenter starts to penetrate toward the workpiece surface. All atoms positions, velocities, acceleration and other related parameters are updated every time step. Throughout this stage, the desired data containing atoms information are dumped, and the information includes atoms velocities, force components acting on indenter atoms and stress components of workpiece atoms. At the post-analysis stage, the dumped data are used to conduct temperature distribution analysis, indentation force calculation, equivalent stress distribution and so forth.

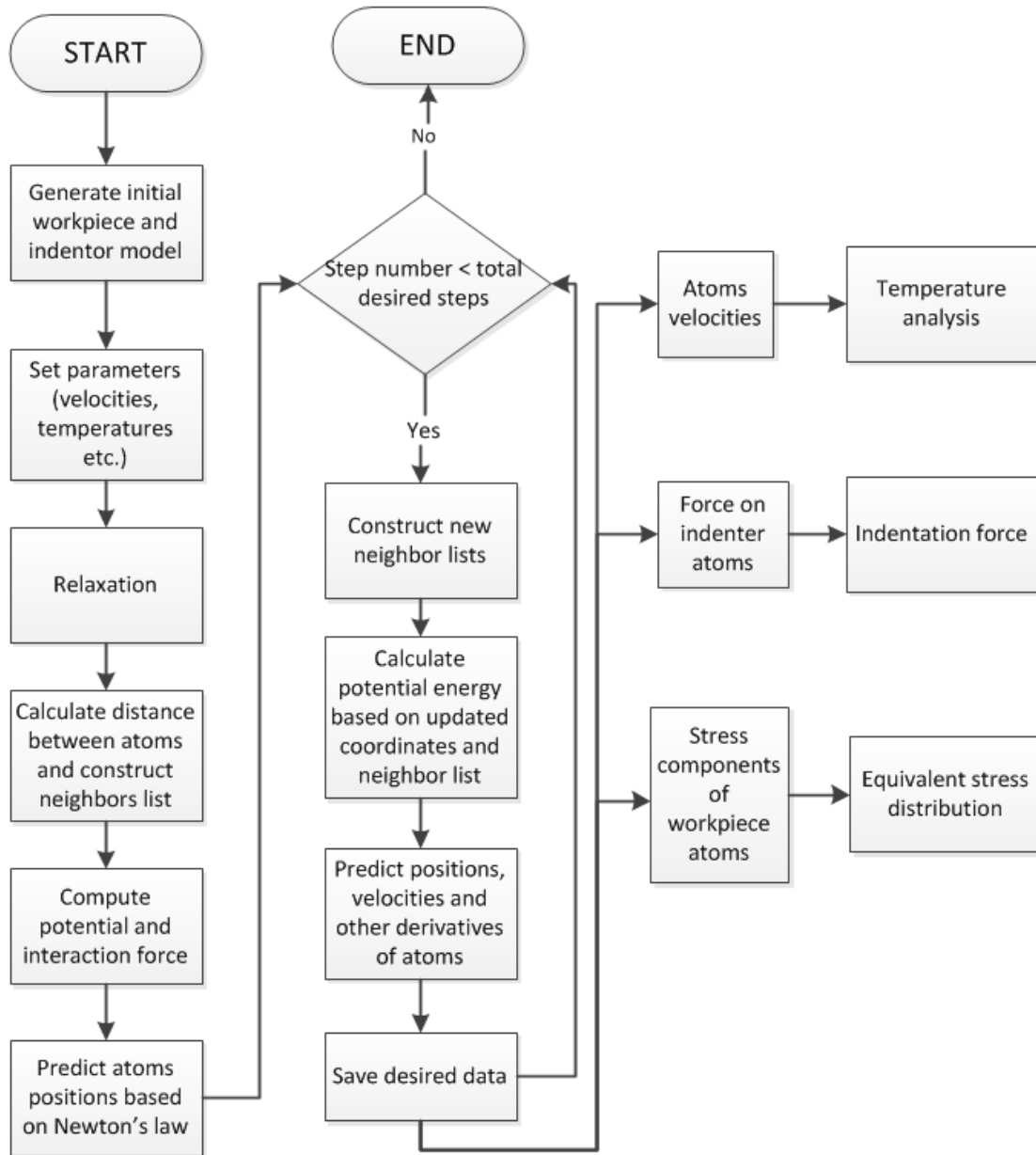


Figure 3.6. Flow diagram of MD simulation for nano-indentation process

### 3.7. Software package

MD simulations in the research is performed by adopting the Large-scale Atomic/Molecular Massively Parallel Simulator (LAMMPS), which is an open source software written in C++ and developed by Sandia National Labs (Plimpton, 1995).

In-house FORTRAN codes are used to carry out post analysis on the output data in order to compute the physical properties of interest, including stress distribution, indentation force, and temperature distribution. Visualization of the MD simulation process is realized by using Atomeye software.

LAMMPS is able to model the atomic biological, polyatomic, metallic, or granular microscopic systems. The source code of LAMMPS has hardware compatibility that can be compiled on a variety of computer architectures. Users can easily customize LAMMPS by adding optional packages for specific simulation needs. LAMMPS performs efficient calculation as it works with MPI (Message Passing Library), which allows for parallel processing when the size of problem becomes very big (e.g. a system containing more than 1,000,000 atoms).

Atomeye is a free atomistic visualization software developed by Li (2003). In the study, this code is used for the same purpose. Atomeye only runs under Linux system and is capable of visualizing system containing more than 2,000,000 atoms. Multiple types of files are supported by Atomeye, including PDB (Protein Data Bank) file as well as CFG format file. PDB format is generally used for storing atomic coordinates for proteins and other biological macromolecules. CFG format is preferred in this study for the reason of ease of visualization. Atomeye eye also provides additional function such as 3D navigation of simulation box, customizable atom radii and coloring schemes, JPEG, PNG and EPS snapshot and movie making. All snapshots taken in the research are produced by Atomeye.

## **CHAPTER 4. NANO-INDENTATION EXPERIMENT**

### **VERIFICATION**

#### **4.1. Brief introduction of AFM**

AFM (Atomic Force Microscopy) nano-indentation experiment is performed to verify the accuracy of MD simulation model construction and potential parameters selection. An AFM is a scanning probe microscopy with very high resolution (in the order of fractions of a nanometer), which is more than 1,000 times better than the optical diffraction limit. It consists of a cantilever with a tip located at the end, and the tip has the radius of curvature on the order of nanometer and is used to scan and interact with sample surface. The cantilever is usually made of silicon or silicon nitride, and the interaction force between sample surface and tip leads to the deflection of cantilever according to Hooke's law. During the scanning process, the deflection of cantilever is measured by a laser beam reflected by the end of the cantilever. The deflected laser signal is then redirected to an array of photodiodes which is connected to feedback electronics. Finally, the surface morphology is recorded. Figure 4.1 gives an illustrative schematic of AFM scanning.

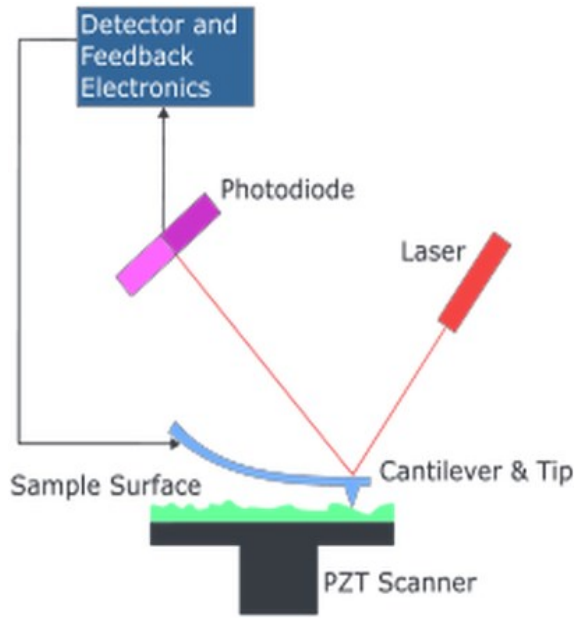


Figure 4.1. Schematic of AFM scanning

## 4.2. Experimental preparation and real-size MD simulation

In this experimental verification, a pyramid diamond indentation tip is adopted and seven indentations are made on a (100) silicon wafer in a row, with indentation loads increased from  $10 \mu\text{N}$  to  $27.5 \mu\text{N}$ . The surface profile is scanned right after the indentations are made. The nano-scratching experiments are conducted on a commercial polished (100) Si wafer, which has an electric conductivity of  $900 \Omega\text{-cm}$ , a radius of 2 inches, and a thickness of  $400 \mu\text{m}$ . Ethanol is used to clean the silicon surface before scratching. All AFM indentations are made at room temperature and under ambient pressure. The pyramid diamond tip has an apex radius of  $40 \text{ nm}$  and is attached on the cantilever of the AFM machine. The cantilever has a spring constant of cantilever of  $196 \text{ N/m}$ . A

commercial AFM machine, model Veeco Dimension™ 3000, is used in this research, as shown in Figure 4.2.

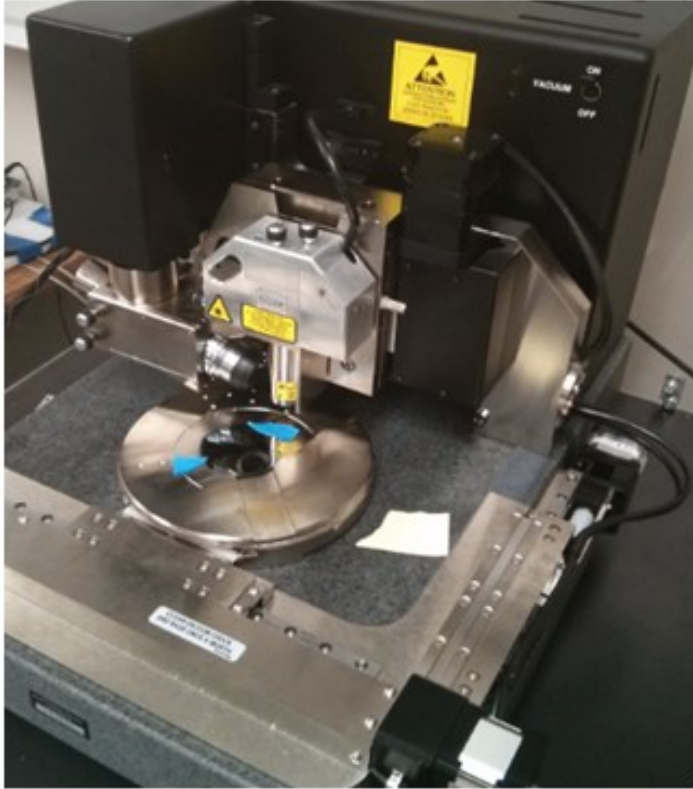


Figure 4.2. AFM nano-indentation experimental set-up

The MD simulation model constructed for verification represents the real AFM nanoindentation configuration, which means the dimension of the indenter modeled is identical to the diamond indenter (within the range of engaged tip depth) used in AFM nano-indentation. In this MD simulation model, the silicon work piece has the dimension of  $500 \times 400 \times 500 \text{ \AA}^3$ , consisting of 5,037,994 silicon atoms. The diamond indenter has a

pyramid shape, with a height of 100 Å and a bottom edge length of 250 Å. The tip of indenter is rounded with a radius of 400 Å; and the indenter consists of 859,205 carbon atoms, as shown in Figure 4.3.

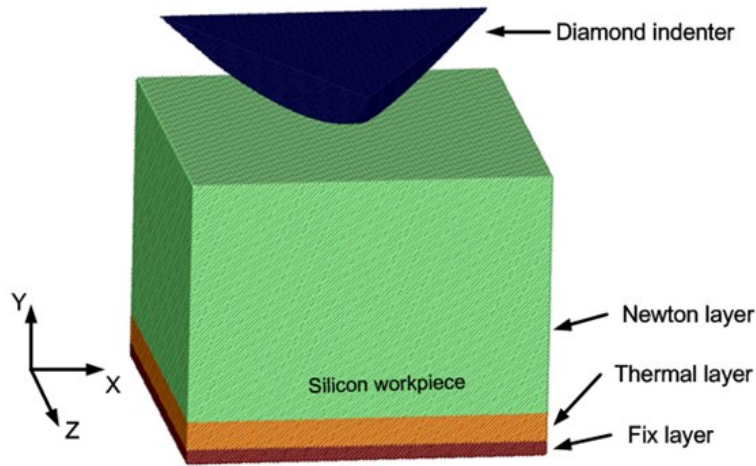


Figure 4.3. MD simulation model for AFM nano-indentation verification

### 4.3. Comparison between experiment and MD simulation model

In the simulation, nine individual indentation simulations are carried out with indentation depths increasing from 2 nm to 10 nm. The indenter is retracted after indentation and the residual indentation depth is measured. Meanwhile, seven AFM nano-indentation operations are performed at the indentation loads of 10, 12.5, 15, 17.5, 20, 22.5, and 25  $\mu\text{N}$ . The seven indents on silicon wafer and corresponding cross sectional analysis are presented in Figure 4.4. From the residual indents made by AFM, it can be seen that as indentation force increases from 10 $\mu\text{N}$  to 25 $\mu\text{N}$ , the size and residual indent depth increase.

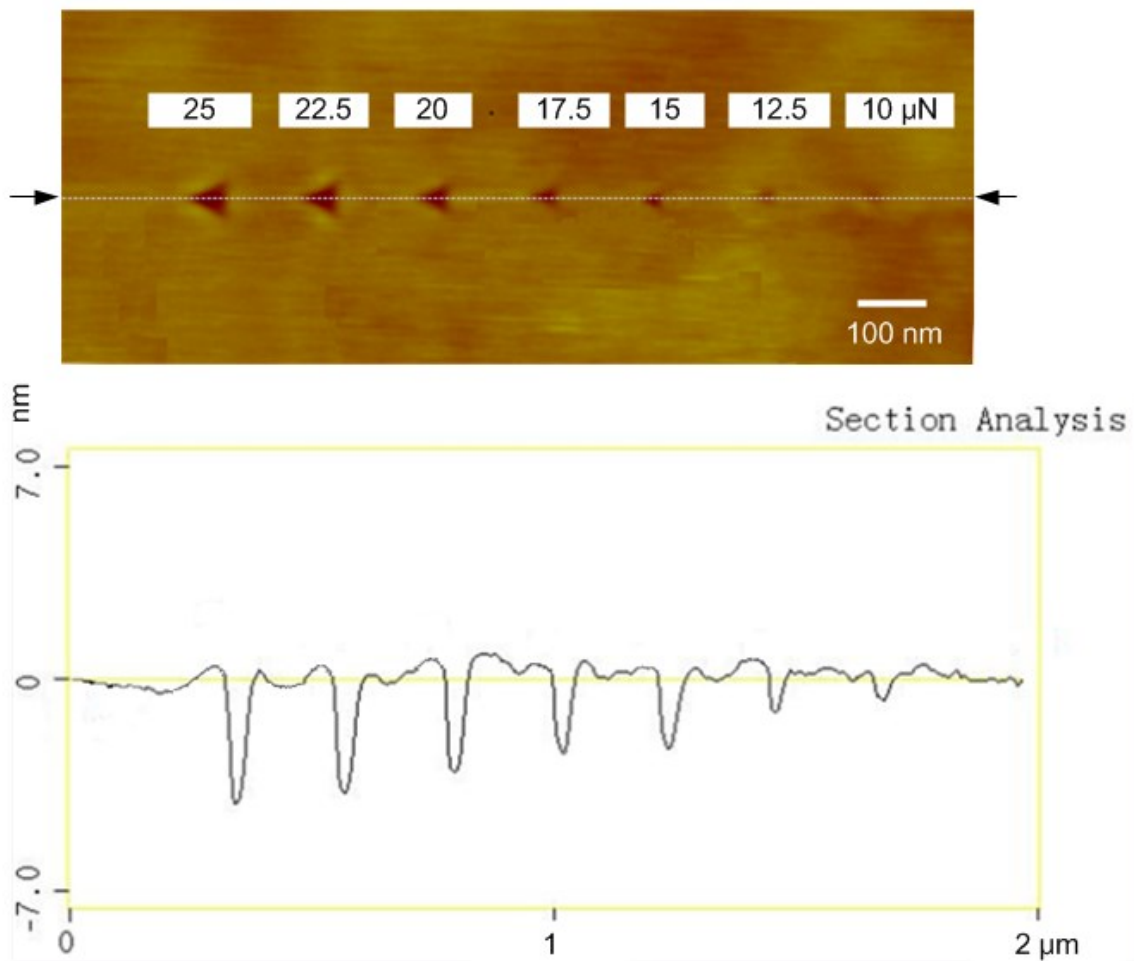
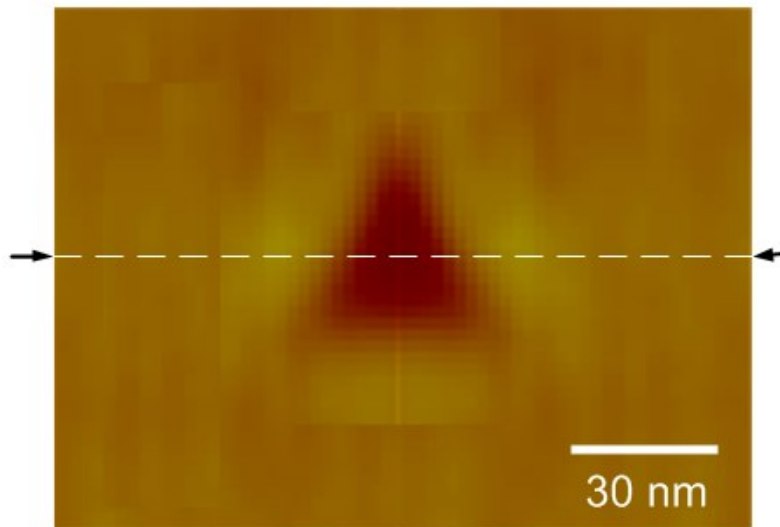


Figure 4.4. AFM nano-indentation and cross section analysis

The comparison of cross sectional views of residual indentation made by MD simulation and AFM indentation at 10nm indentation depth is presented by Figure 4.5. It is found that the two profiles agree fairly well by comparing the maximum residual indentation depth and pile up around the indentation. Both MD simulation and AFM

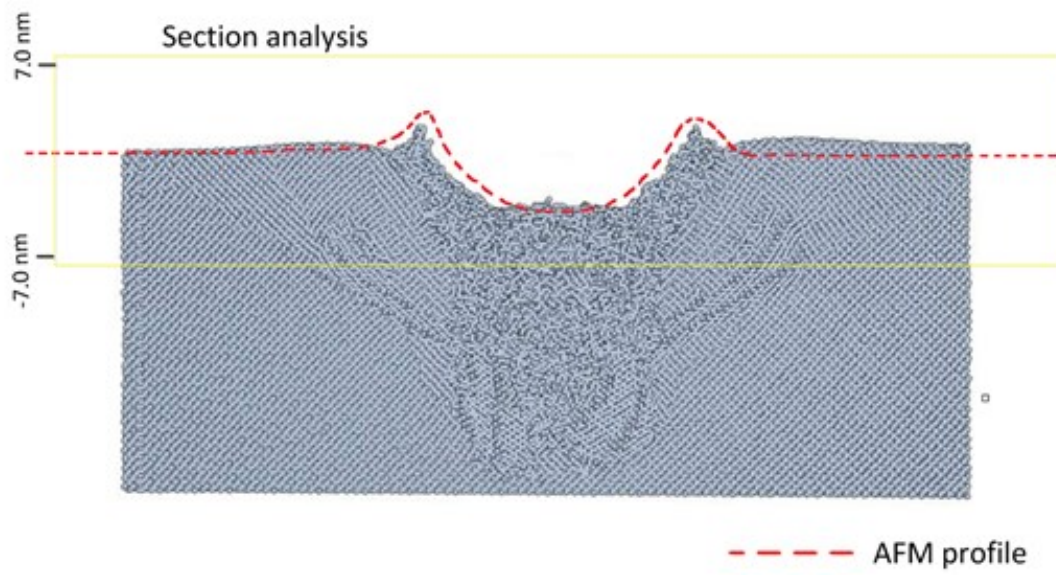
scanning profiles indicate that the depth of indentation is around 4 nm and the pile-up height is around 2 nm.

Indentation force with respect to residual indentation depth under a series of different loads is also plotted, as shown in Figure 4.6. It can be seen that the curves obtained from MD simulation and AFM indentation experiment again are very close. The results verify that the MD model construction and potential parameter selection in this simulation study are accurate and capable of reflecting real material deformation mechanism in the nano-indentation experiment.



(a)

Figure 4.5. Comparison of cross-section profile for MD simulation and AFM scanning: (a) AFM nano-indentation made at 25  $\mu\text{N}$ , (b) cross section analysis comparison of AFM and MD nano-indentation



(b)

Figure 4.5. Comparison of cross-section profile for MD simulation and AFM scanning: (a) AFM nano-indentation made at 25  $\mu\text{N}$ , (b) cross section analysis comparison of AFM and MD nano-indentation (Continued)

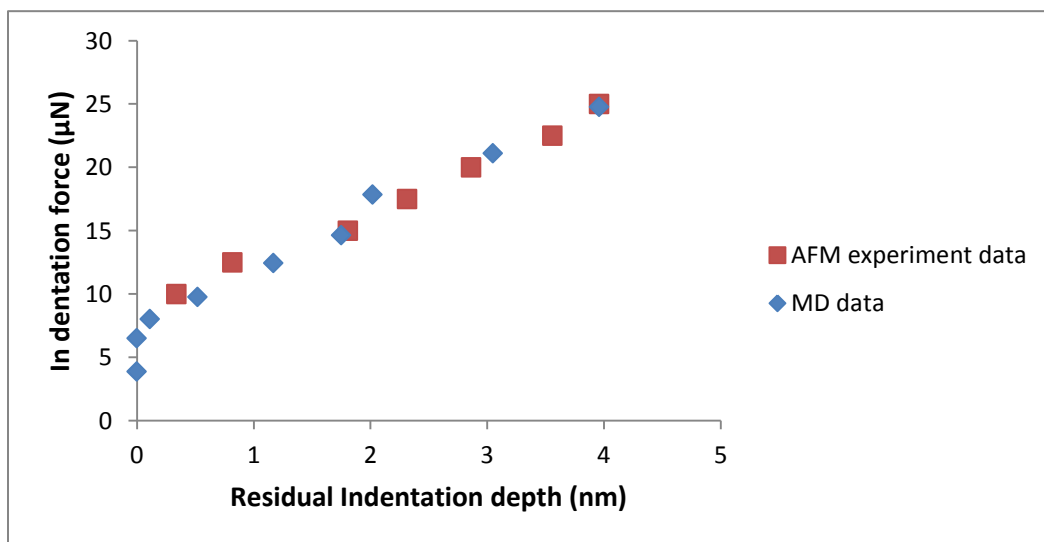


Figure 4.6. Force with respect to residual indent depth for MD simulation and AFM nano-indentation experiment

## CHAPTER 5. TEMPERATURE EFFECT ON NANO-INDENTATION OF MONOCRYSTALLINE SILICON

The two phases formed inside the indented region during the indentation process are identified with the aid of radial distribution function (RDF) analysis, which is also widely adopted in literature. Diamond cubic silicon is four-fold coordinated with all of the four neighbors at distance of 2.35 Å. Bct-5 silicon has five-fold coordination structure with one neighbor atom at distance of 2.31 Å and other four at 2.44 Å.  $\beta$ -silicon is six-fold coordinated with four nearest neighbors at distance of 2.42 Å and two at the slightly larger distance of 2.57 Å.

### 5.1. Phase transformation during nano-indentation process

Figure 5.1 shows the (110) cross-sectional views of bct-5 silicon and  $\beta$ -silicon phase distributions at various indentation depths when the initial temperature is 300K. Red atoms represent the bct-5 silicon phase and green atoms represent  $\beta$ -silicon. Grey atoms represent original diamond cubic silicon or other possible metastable phases with four-fold coordination. Very few amounts of higher-coordinated atoms and surface atoms are labeled by cyan. Snapshots corresponding to the occurrence of bct-5 silicon,  $\beta$ -silicon, and at the maximum indentation position are shown in Figure 5.1 (a), (b), and (c) respectively. It is found that bct-5 silicon forms in the subsurface at the indentation depth of 28 Å. Note that there is a layer of silicon atoms with original four-fold structure

directly beneath the indenter and this layer of original four-fold silicon structure exists during the entire indentation process. As the indenter keeps advancing,  $\beta$ -silicon starts to appear at the indentation depth of 50 Å. It is located in the center of phase transformed region, surrounded by the five-fold bct-5 silicon. With the increase of indentation depth, the sizes of bct-5 silicon and  $\beta$ -silicon region keep increasing. Overall, the distributions of phase transformation exhibit anisotropic and symmetric patterns. By examining Figure 5.1 (d), it is found that  $\beta$ -silicon concentrates at the center of phase transformation region and also occupies a large area around the center, while bct-5 silicon forms along  $\langle 110 \rangle$  crystal direction and divides the surrounding  $\beta$ -silicon into four separate regions.

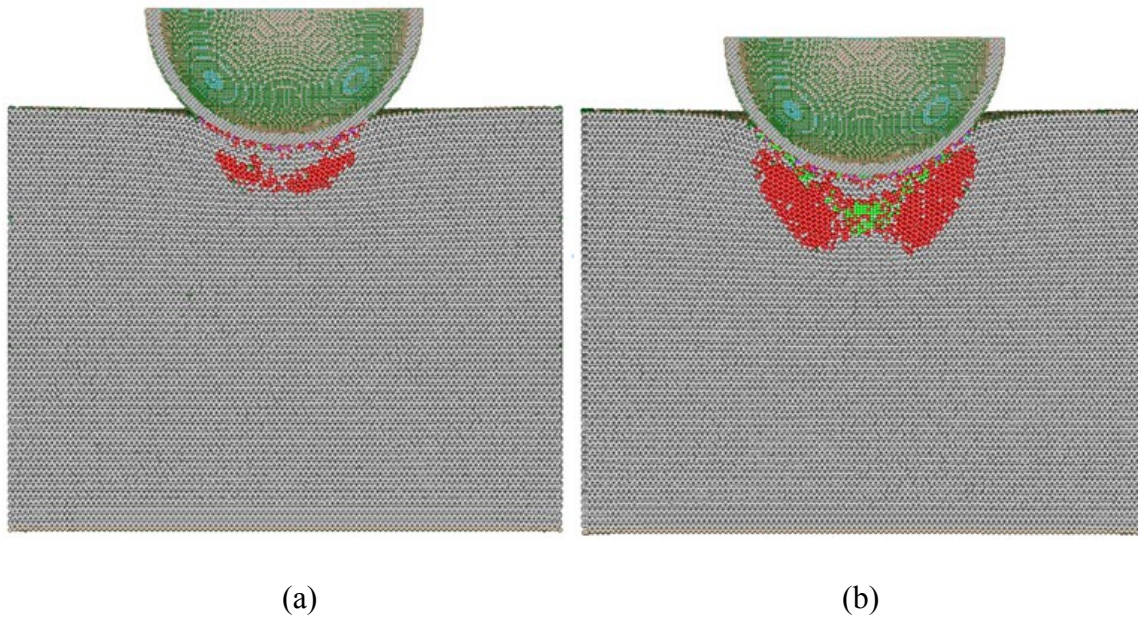


Figure 5.1. Three side cross-sectional views of phase transformation distribution at indentation depths of (a) 28 Å, (b) 50 Å, (c) 77 Å and (d) the corresponding top cross-sectional view  $ss'$

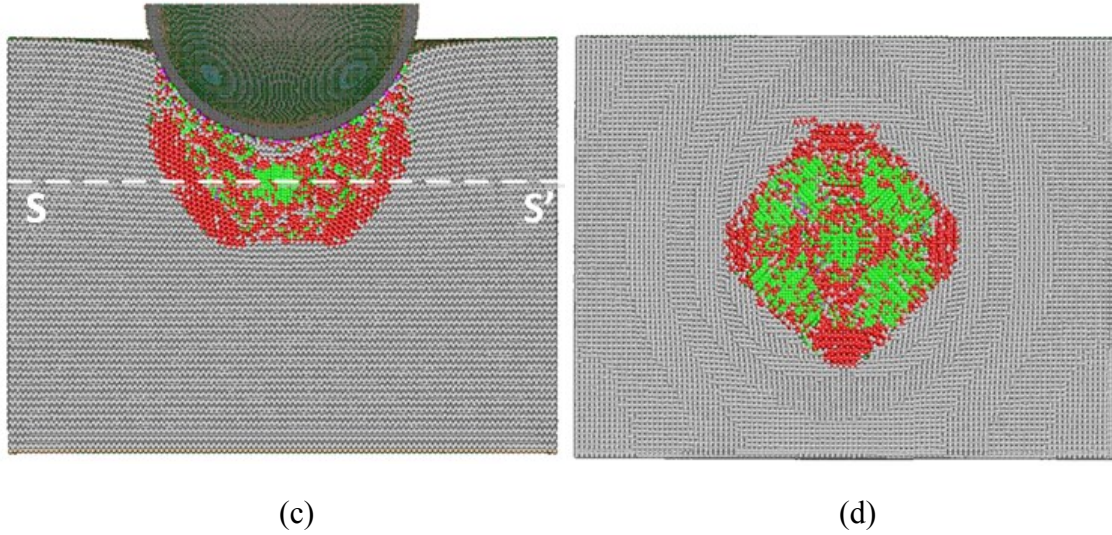


Figure 5.1. Three side cross-sectional views of phase transformation distribution at indentation depths of (a) 28 Å, (b) 50 Å, (c) 77 Å and (d) the corresponding top cross-sectional view  $ss'$  (Continued)

The phase transformation evolutions as the increase of indentation stress are also plotted, as shown in Figure 5.2 (for the case of 300K initial temperature). The overall indentation stress can be calculated as the ratio between indentation load  $P$  and projected contact area  $A_c$  between the indenter and workpiece,.

$$\sigma = \frac{P}{A_c} \quad (5.1)$$

The indentation stress is monitored during the entire indentation process and its magnitude increases with the increase of indentation depth. Figure 5.2 indicates that the increase of indentation stress leads to the phase transformation of silicon, and the threshold indentation stress for both types of silicon phase transformation (original silicon to bct-5 silicon and  $\beta$ -silicon) is around 5 GPa. Once formed, the amount of bct-5

silicon atoms increases almost linearly for the rest of indentation process. While the increase of  $\beta$ -silicon atom number is much slower at beginning, it becomes more drastic when indentation stress reaches 9.2 GPa. Its slope reduces again when the indentation stress becomes greater than 11 GPa.

In order to present the temperature effect on silicon phase transformation, the amounts of both types of silicon atoms with the indentation stress of 13 GPa for various initial temperatures are compared, as shown in Figure 5.3. It is found that  $\beta$ -silicon formation is significantly affected by temperature, and a downward trend is observed as the temperature increases. However, the formation of bct-5 silicon seems to be less temperature sensitive, which means the amount keeps almost unchanged as the temperature changes from 30K to 700K.

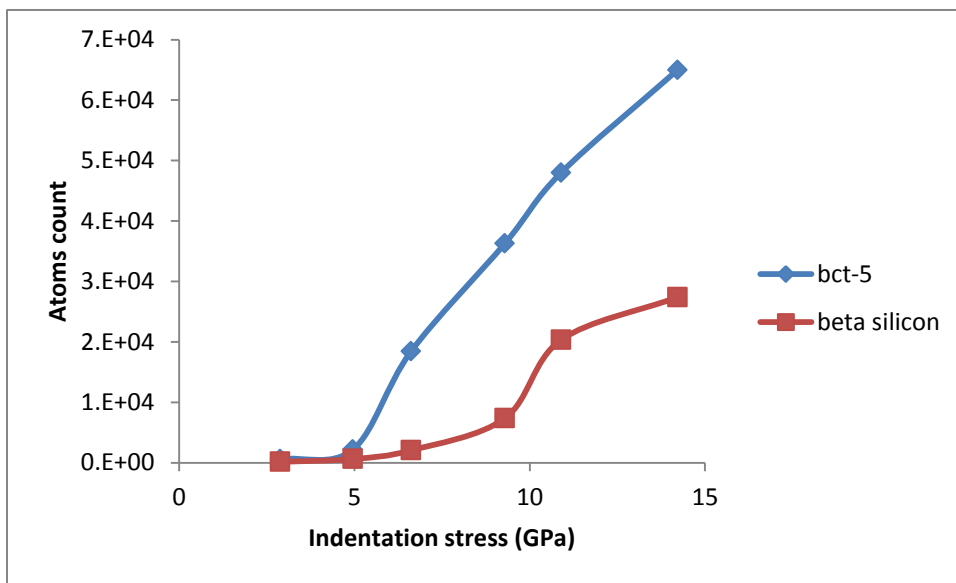


Figure 5.2. Phase transformation evolution with respect to indentation stress for 300K initial temperature

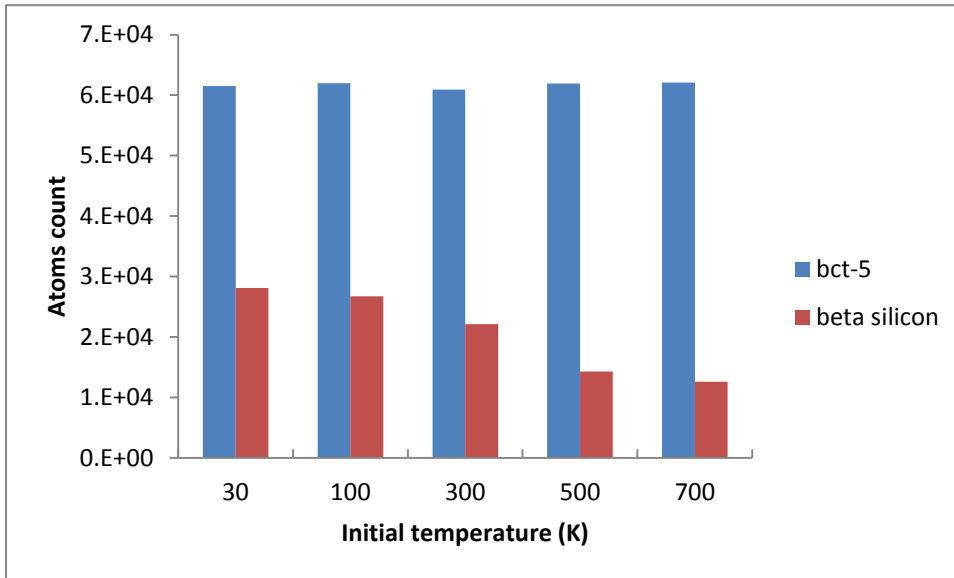


Figure 5.3. Phase transformation comparison for various initial temperatures (data is taken at indentation stress of 13 GPa)

## 5.2. Equivalent stress distribution during nano-indentation

The equivalent stress distributions corresponding to the initial appearances of bct-5 and  $\beta$ -silicon are shown in Figure 5.4 (a) and (b). The analysis reveals that bct-5 and  $\beta$ -silicon initially form at the equivalent stresses of 43 and 39 GPa, respectively. Similarly, the stress distributions shown in Figure 5.4 (c) and (d) are obtained at the same time moment and along the same cross-section planes as Figure 5.1 (c) and (d). In general, compared with the phase transformation area, the stressed affected area is deeper and wider in each snapshot. Meanwhile, the cross sectional view indicates that the equivalent stress can somehow define the distribution of bct-5 silicon and  $\beta$ -silicon. During the entire indentation process, the maximum stress is located along the indenter/workpiece

interface and its magnitude increases as the penetration of indenter progresses. The maximum equivalent stresses are 73 GPa, 77 GPa, and 80 GPa for indentation depth of 28 Å, 50 Å, and 77 Å respectively.  $\beta$ -silicon region has overall lower stress levels than bct-5 silicon region. Bct-5 silicon has the stress range of 45-55 GPa, while  $\beta$ -silicon exists at the equivalent stress of 30-40 GPa.

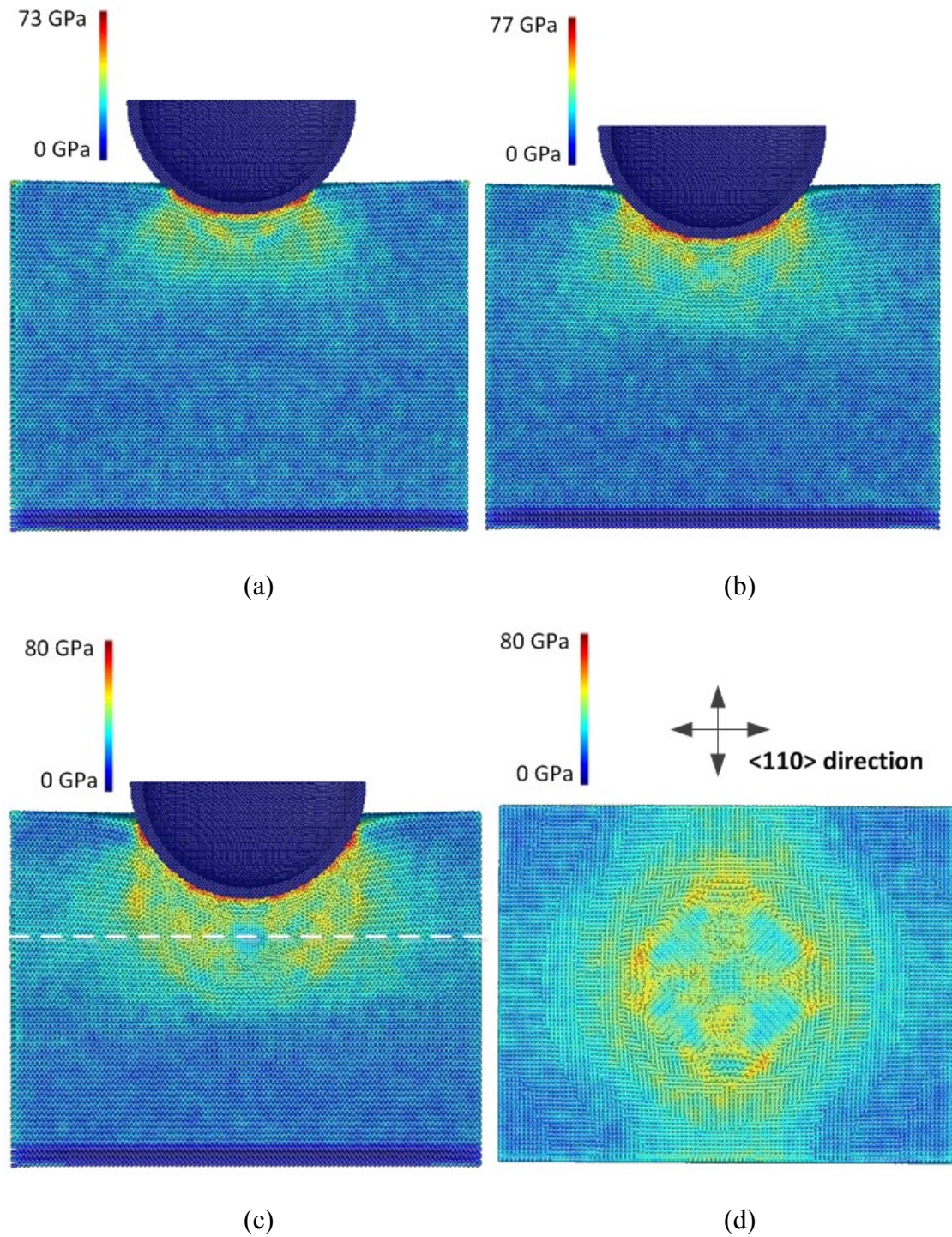


Figure 5.4. Three side cross-sectional views of equivalent stress distribution at indentation depths of (a) 28 Å, (b) 50 Å, (c) 77 Å, as well as (d) one top cross-sectional view at the depth of 77 Å

### 5.3. Temperature distribution

Temperature distribution inside silicon workpiece at the maximum indentation depth is shown in Figure 5.5 for the five levels of initial temperatures. Obviously, for all initial temperature configurations, the penetration of indenter leads to significant local temperature rise inside workpiece beneath indenter. For the rest of work material other than the local region of higher temperature, the distribution of temperature is overall uniform. The temperatures of phase transformation region are estimated to be 110K, 230K, 450K, 650K, and 850K for the initial temperatures of 30K, 100K, 300K, 500K, and 700K, respectively.

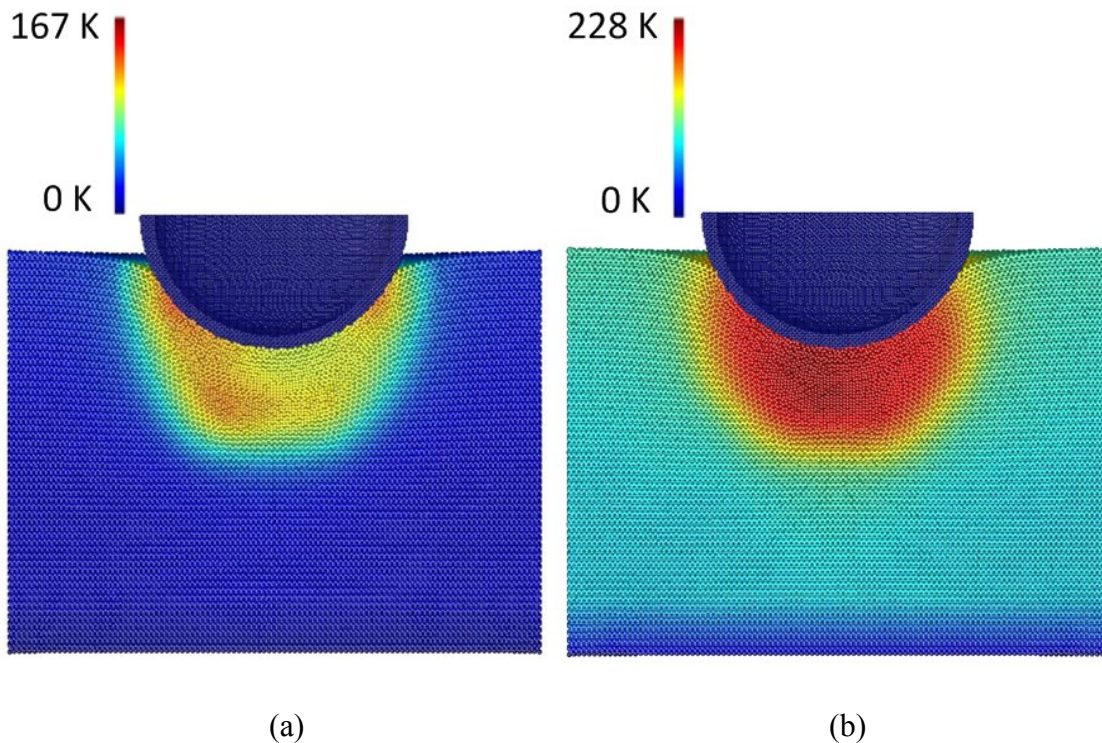


Figure 5.5. Temperature distributions at the maximum indentation depth at the initial temperatures of (a) 30K, (b) 100K, (c) 300K, (d) 500K, and (e) 700K

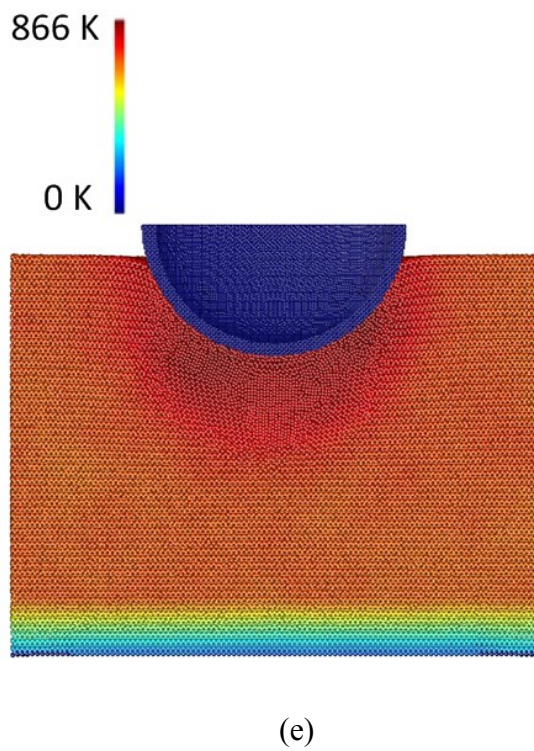
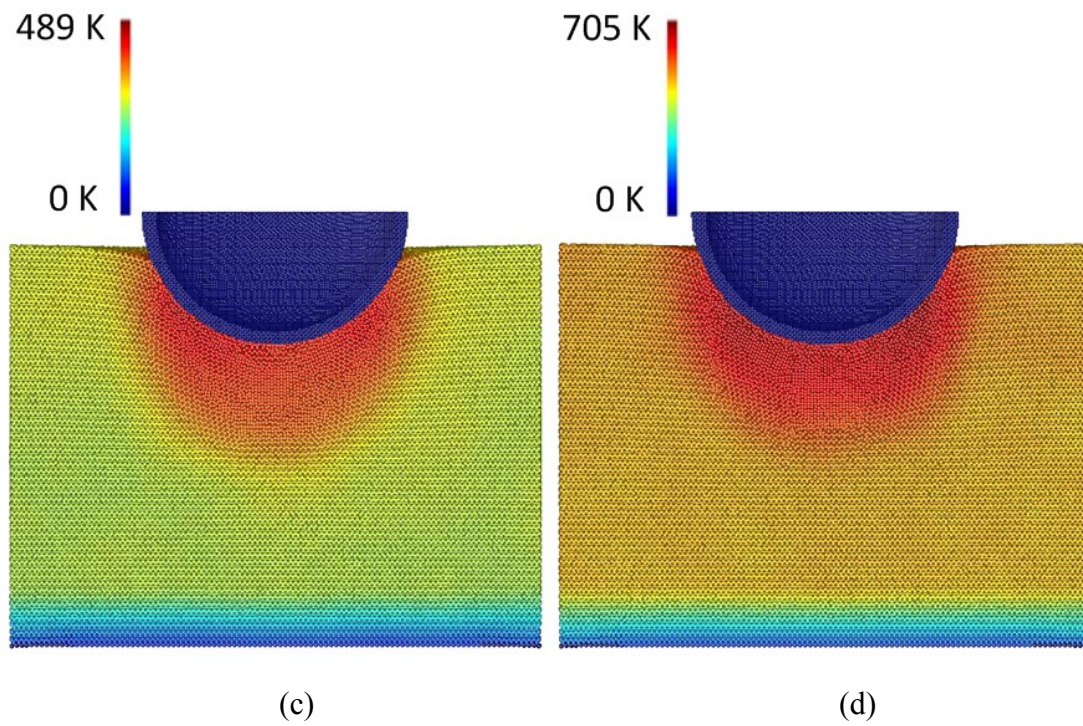


Figure 5.5. Temperature distributions at the maximum indentation depth at the initial temperatures of (a) 30K, (b) 100K, (c) 300K, (d) 500K, and (e) 700K (Continued)

#### 5.4. Temperature effect on phase transformation

Figure 5.6 depicts the indentation force evolution at the five different temperatures. It can be seen from the figure that there is no significant difference in indentation force among the 5 cases when the indentation depth is less than 50 Å. As the indentation depth further increases, the indentation force becomes smaller at higher temperatures. At the maximum indentation depth, the indentation forces are 5059 eV/Å and 3995 eV/Å for the 30 K and 700 K cases, respectively. This represents a relative decrease of 21% in indentation force. More importantly, the number of bct-5 silicon atoms with respect to the indentation depth is obtained for all the simulation cases, as shown in Figure 5.7. All cases have similar trends – once bct-5 silicon forms, and the number of bct-5 atoms increases almost linearly with the indentation depth. More important analysis should be on the difference among the cases. Clearly, the indentation depth required for the occurrence of bct-5 silicon decreases with the increase of the initial temperature. For example, for the case with the initial temperature of 700 K, bct-5 silicon phase starts to form at the indentation depth of 22.5 Å; while for the case with the initial temperature of 30K, phase transformation to bct-5 silicon does not start until the indentation depth reaches 40.5 Å. This is because the stress in phase transformation zone increases more rapidly at higher temperatures, and this significantly facilitates the bct-5 silicon phase transformation. Note that it is observed that the stress required for bct-5 silicon transformation is hardly dependent on the initial temperature, and the threshold

pressure for bct-5 phase transformation is around 44 GPa for all the cases. Figure 5.10 shows the comparison of stress distributions between the cases of 30K and 700K at the indentation depth of 40.5 Å. The patterns in the two cases are not alike, and the 700K case has overall higher stress levels than the 30K case.

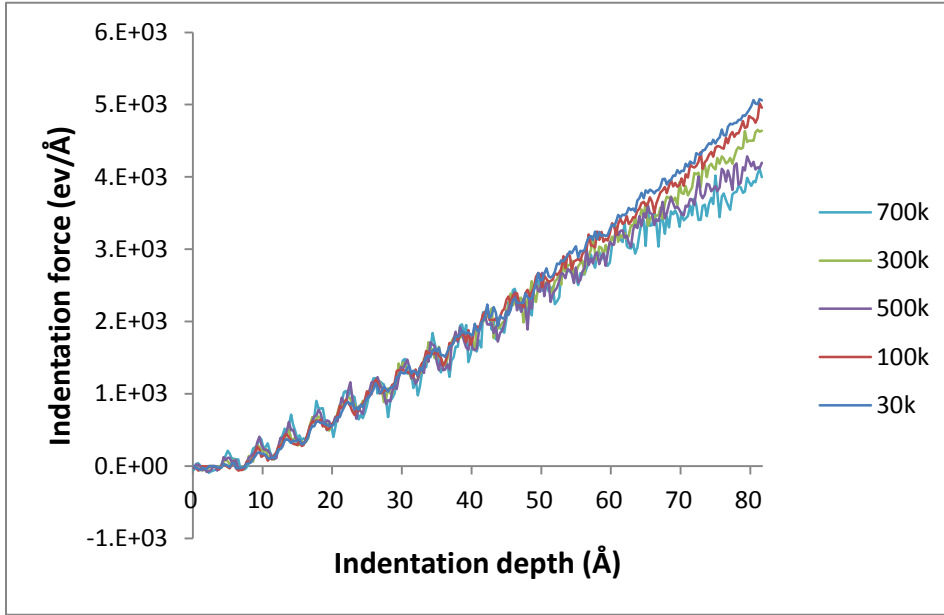


Figure 5.6. Indentation force evolution at different initial temperatures

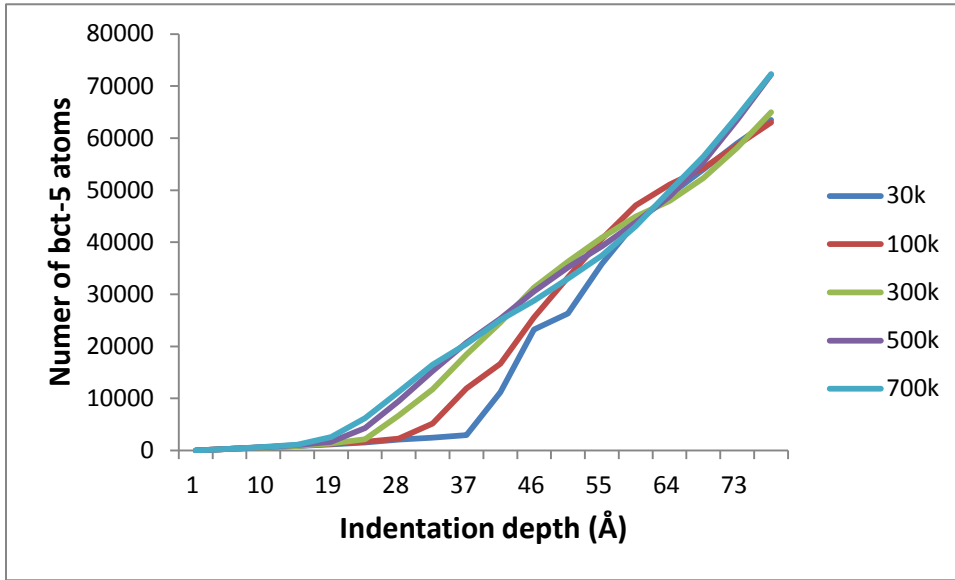


Figure 5.7. Number of atoms with bct-5 silicon phase structure with respect to indentation depth

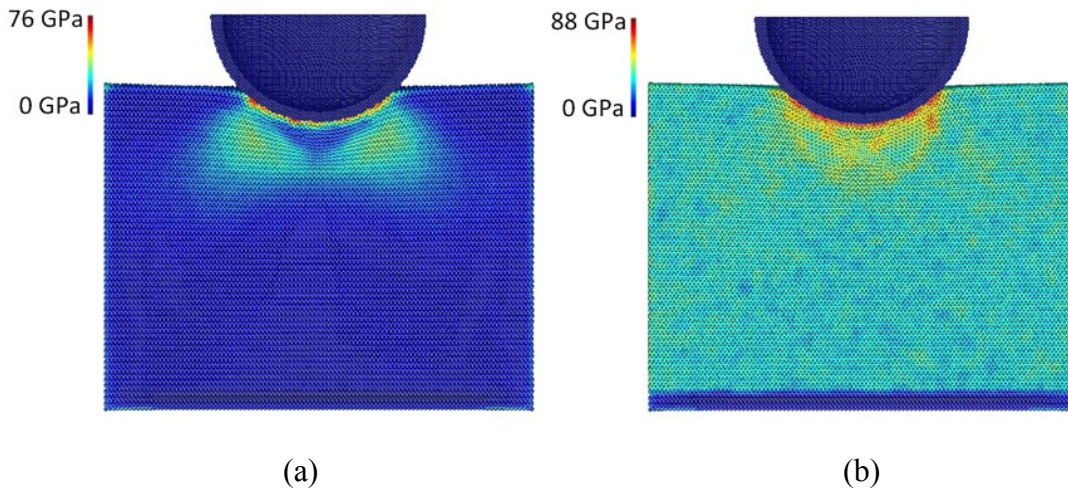


Figure 5.8. Stress distribution at indentation depth of 40.5 Å for the initial temperatures of (a) 30K and (b) 700K

Figure 5.9 presents the number of six-fold  $\beta$ -silicon atoms during the loading process with respect to different initial temperatures. With the indentation depth less than 20 Å, it is found that in all cases, the number of six-fold  $\beta$ -silicon atoms gradually

increases in an overlapping pattern. As the indentation depth increases, similar to the evolution of amount  $\beta$ -5 silicon, more  $\beta$ -silicon atoms are formed at higher initial temperatures. This is caused by quicker stress elevation at the loading process in the higher temperature cases. However, as the indentation depth exceeds 50 Å, the higher temperature cases exhibit slower rates of  $\beta$ -silicon growth compared with the lower temperature cases. As a result, at the maximum indentation depth, the number of  $\beta$ -silicon atoms is found to be reversely related to the initial temperature. The 30K case has about 33,000  $\beta$ -silicon atoms, while the 700K case has only around 12,000  $\beta$ -silicon atoms.

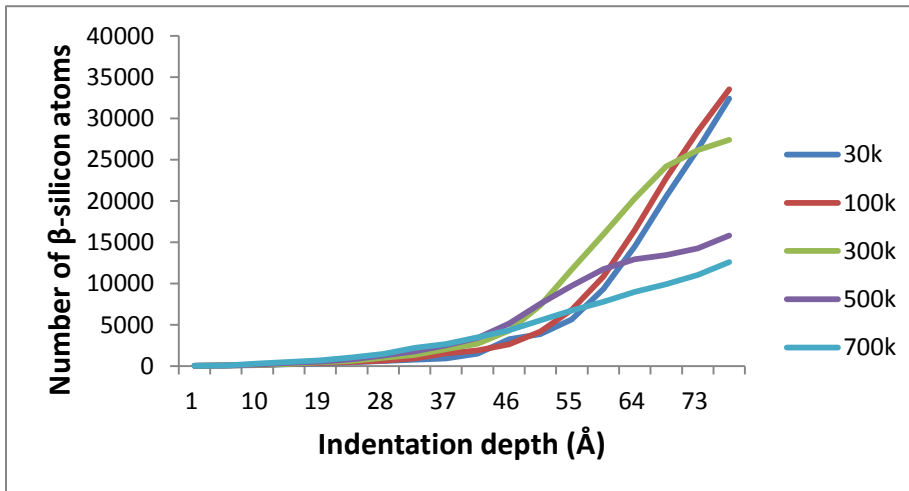
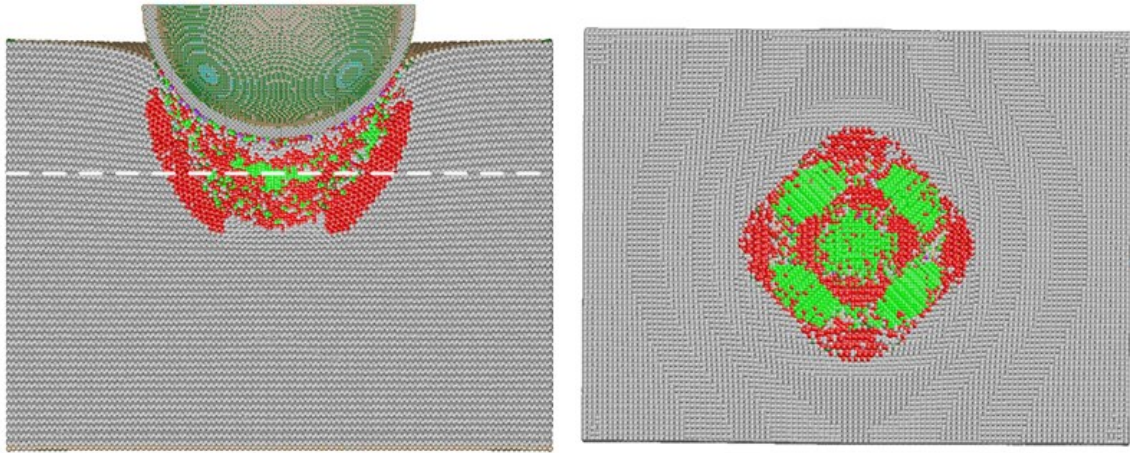


Figure 5.9. Number of atoms with  $\beta$ -silicon phase structure vs. indentation depth

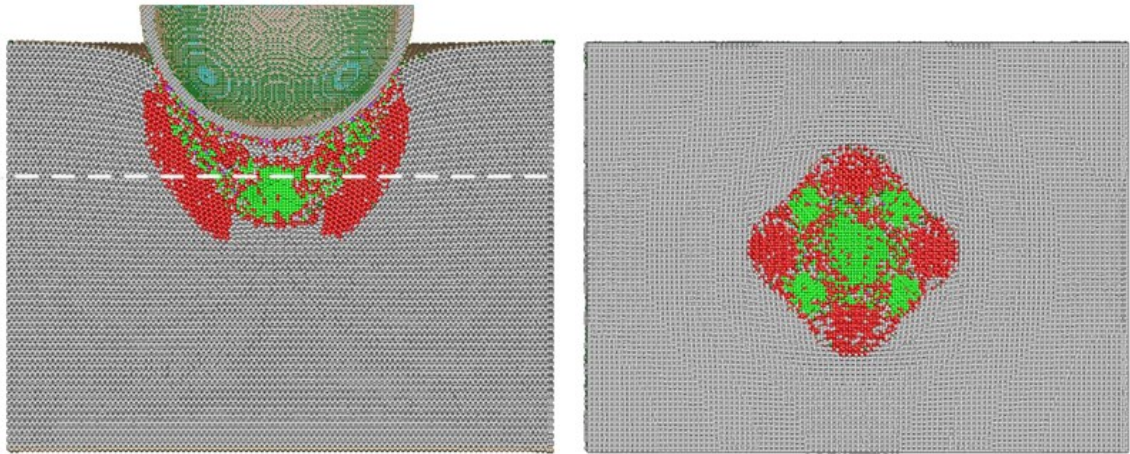
The (110) side view and (100) top view of phase transformation at the maximum indentation depth are shown in Figure 5.10. It can be seen that all indentation cases with different initial temperatures have similar shapes but different sizes, with the maximum

width approximately equal to the indenter diameter and the maximum depth approximately equal to the indenter radius. At the initial temperature of 30K, the phase transformation region in the (100) top view has a rectangular shape with  $\beta$ -silicon being symmetrically surrounded by bct-5 silicon. At the initial temperature of 700K, the distribution of the two metastable phases exhibits more randomness, and the boundary between  $\beta$ -silicon and bct-5 silicon can be hardly seen.

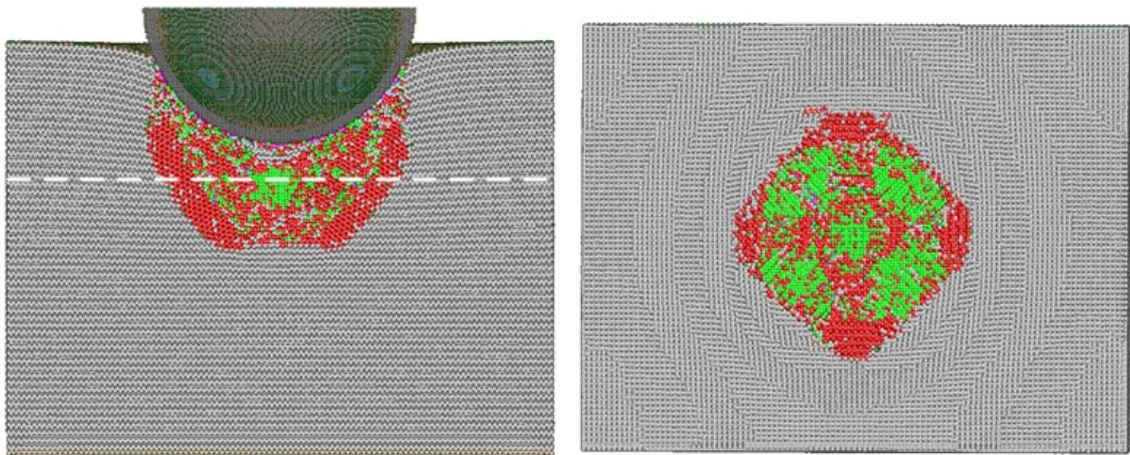
The corresponding equivalent stress distributions are obtained and shown in Figure 5.11. It can be seen that the maximum equivalent stresses are all within the range of 80-84 GPa for all the cases. Overall, the equivalent stress in bct-5 silicon is in the range of 45-55 GPa, which is higher than that of 30-40 GPa in  $\beta$ -silicon. By retrieving the formation stress of  $\beta$ -silicon phase in all the cases, it is found that  $\beta$ -silicon formation stress is positively proportional to the initial temperature. This is different from the bct-5 silicon phase, which is almost independent of the initial temperature. The formation stresses for  $\beta$ -silicon phase are determined to be 34, 36, 39, 43, and 46 GPa for the cases simulated at the initial temperatures of 30, 100, 300, 500, and 700K, respectively. Higher formation stress requirement is believed to be the cause of less amount of  $\beta$ -silicon phase formed at higher temperatures. This certainly makes sense. The silicon phase diagram indicates that in the range of 0 – 1000 °C, higher pressure is required for silicon to transform into metallic phase (Bundy, 1964).



(a)

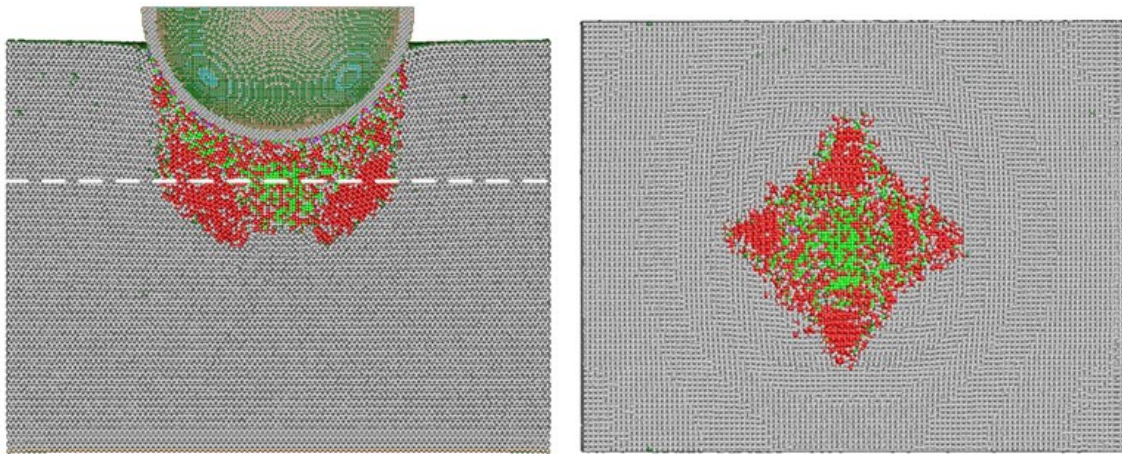


(b)

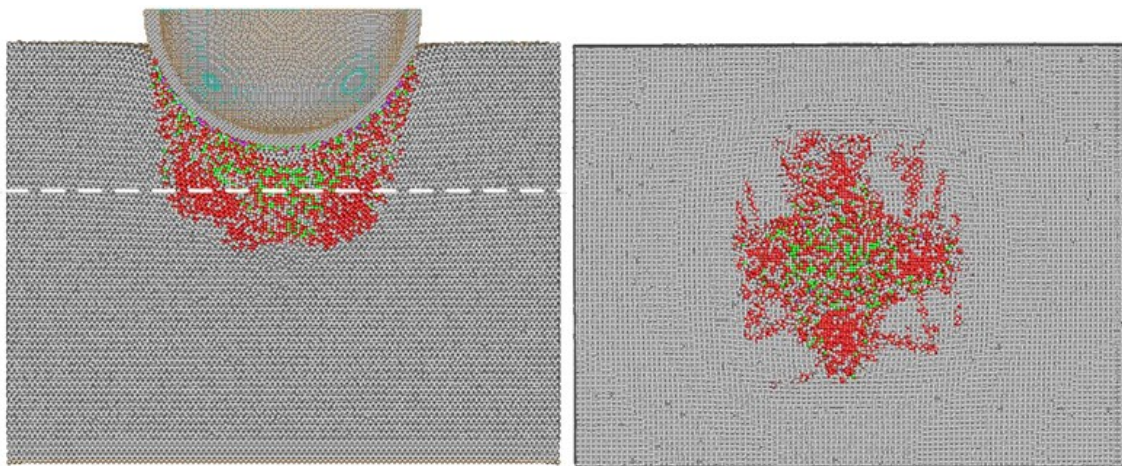


(c)

Figure 5.10. Phase transformation distribution at the maximum indentation depth at the initial temperatures of (a) 30K (b) 100K (c) 300K (d) 500K and (e) 700K



(d)



(e)

Figure 5.10. Phase transformation distribution at the maximum indentation depth at the initial temperatures of (a) 30K (b) 100K (c) 300K (d) 500K and (e) 700K (Continued)

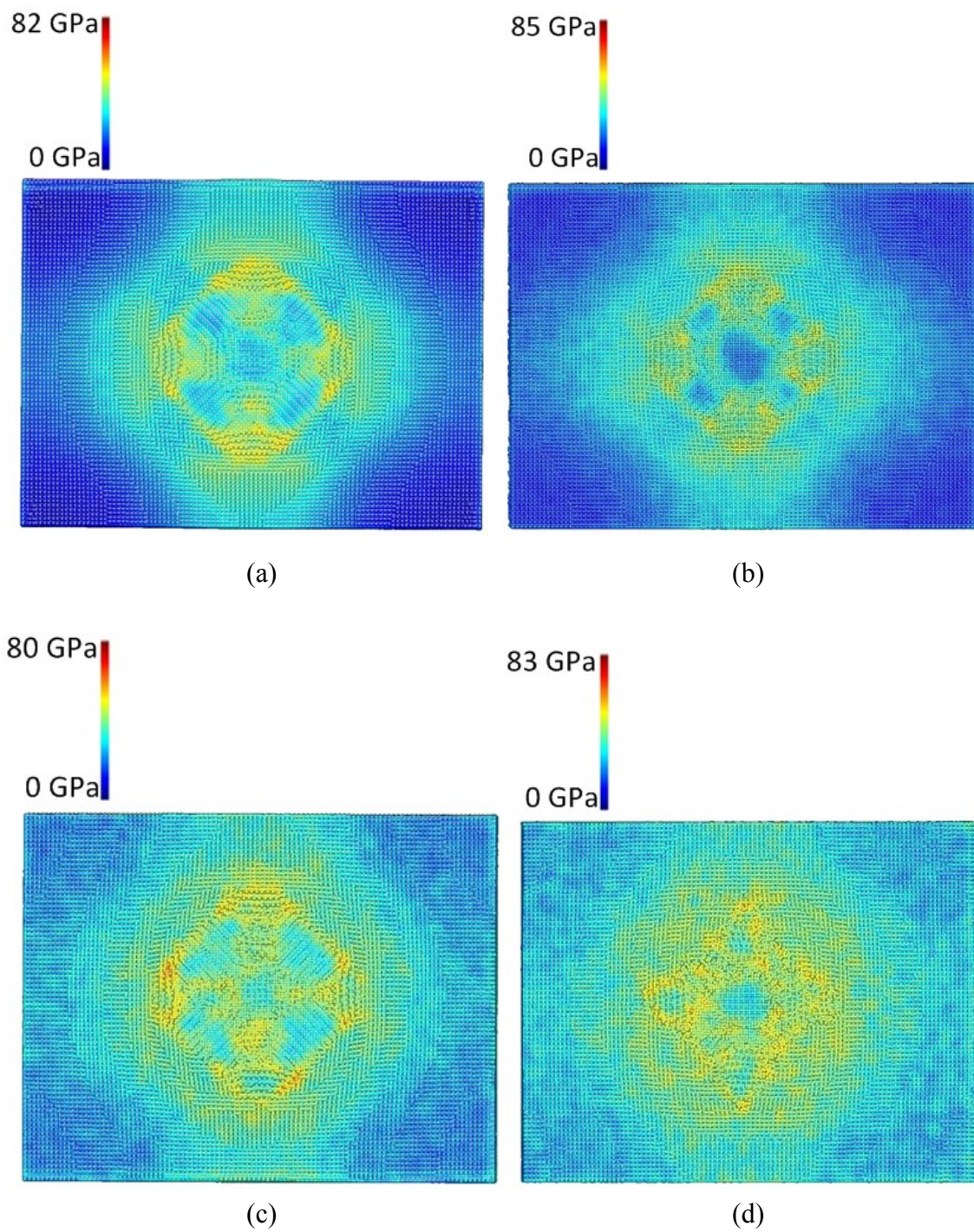
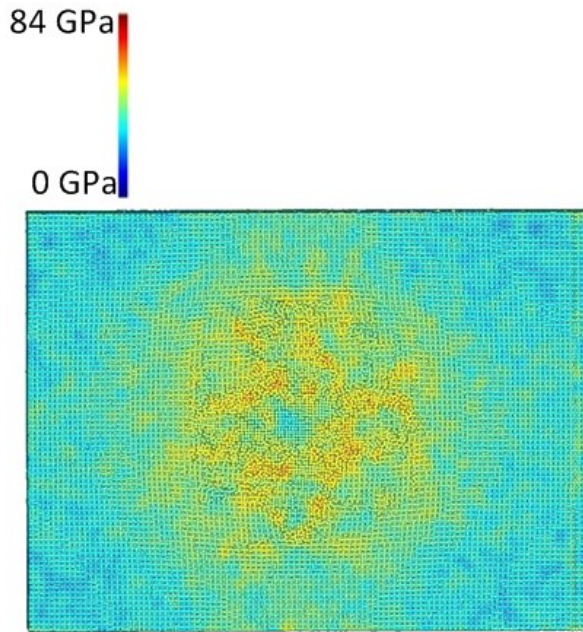


Figure 5.11. Equivalent stress distributions at the maximum indentation depth at the initial temperatures of (a) 30K (b) 100K (c) 300K (d) 500K and (e) 700K



(e)

Figure 5.11. Equivalent stress distributions at the maximum indentation depth at the initial temperatures of (a) 30K (b) 100K (c) 300K (d) 500K and (e) 700K (Continued)

### 5.5. Temperature effect on stress distribution on indenter/workpiece interface

The distributions of normal force at different temperature are presented in Figure 5.12. The five curves exhibit similar trends with the increase of “arc distance to the indenter tip”, namely, the normal force increases along the interface at beginning and then gradually decreases to zero. For the cases of 30K and 100K, the maximum force occurs at around half length of the entire interface. While for other higher temperature cases, the maximum normal force appears at a shorter distance from the tip, about the length of only one atom group. Overall, the normal force decreases with the increase of initial temperature along the entire interface. Also, for each case, the normal force gradually decreases to zero along the interface when the work material and indenter cease

to be in contact. Meanwhile, the tangential force distributions along the indenter/work interface at different initial temperatures are obtained as well, as shown in Figure 5.13. Obviously, the tangential distributions exhibit more randomness and fluctuation, in which the case of 700K initial temperature is most difficult to categorize. For other cases, a general trend exists - the tangential force increases from the indenter tip along the interface until a maximum value is reached. Also, for all the cases, it can still be observed that the total tangential force along the interface is generally higher when the initial temperature is lower.

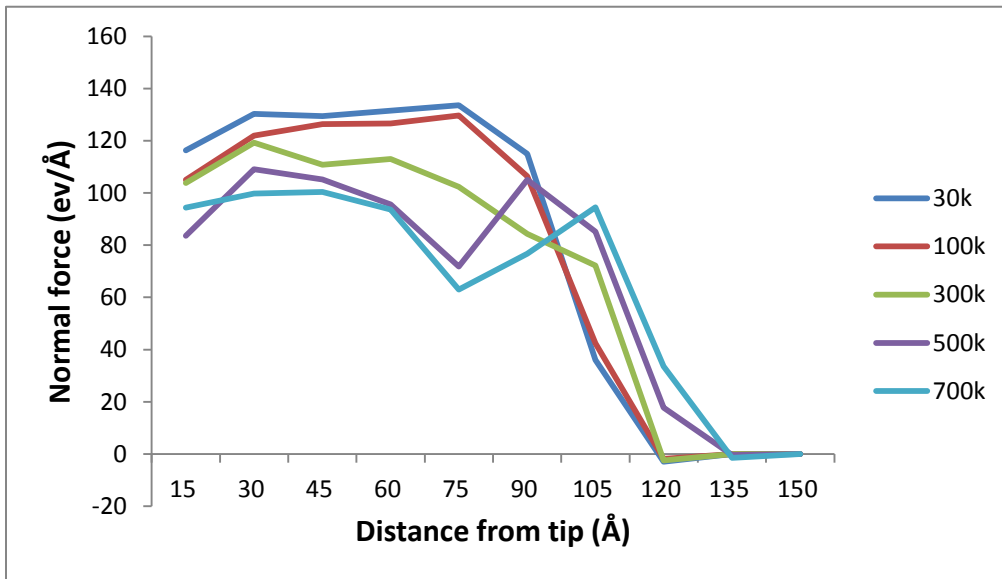


Figure 5. 12. Temperature effect on the normal force distribution on indenter/workpiece interface

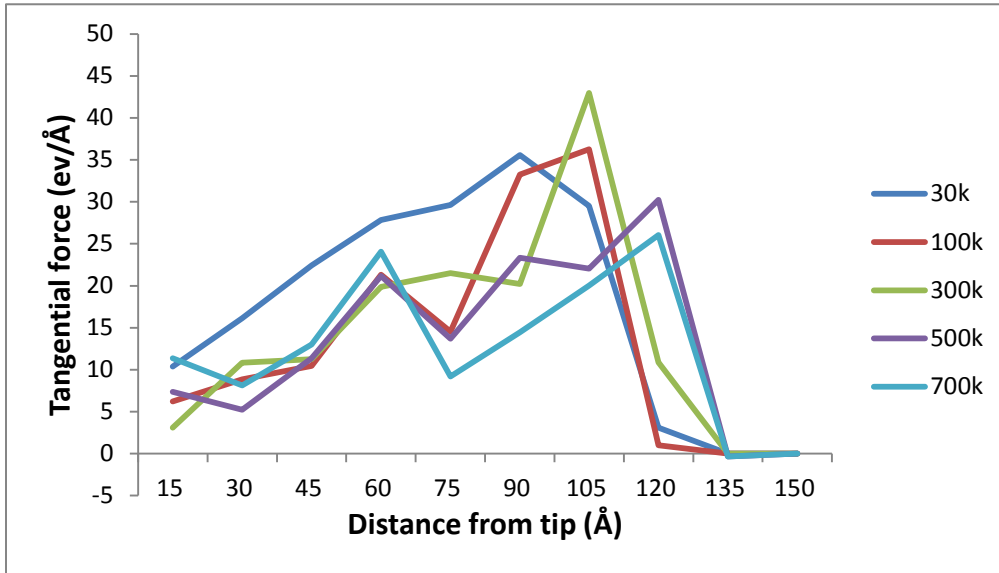


Figure 5.13. Temperature effect on the tangential force distribution on indenter/workpiece interface

### 5.6. Temperature effect on unloading process

Figure 5.14 illustrates the effect of temperature on indentation force during the tool retraction process. For all different temperatures, the indentation force decreases quickly at the beginning and reaches the equilibrium state (no force acting on indenter) at the retraction distance of about 2.2 nm. Before reaching the equilibrium state, the indenter-material interaction is repulsive, while the interaction between indenter and workpiece becomes adhesive as indenter further retracts. This is to the result of atomic adhesive effects between carbon atoms and silicon atoms. After the equilibrium state, the indentation force reduces to zero as the indenter is withdrawn to its original position. It can be seen from the unloading curves that the initial temperature significantly affects the indenter/workpiece adhesion during unloading process. For all cases presented in Fig.

5.11, the magnitude of peak adhesive force is about 1500 ev/Å. But the peak adhesive force occurs at different indenter retraction distances. Overall, the maximum adhesive force happens at longer retraction distances for higher temperatures. To be more specific, the maximum adhesive force occurs at 41 Å, 42 Å, 44 Å, 56 Å, and 61 Å for the cases of 30K, 100K, 300K, 500K, and 700K, respectively. More importantly, with a higher temperature, the adhesion region is wider and the decrease of adhesive force is slower. This implies that lower temperature can significantly reduce the attraction effect between carbon and copper atoms. The indenter retraction distances where adhesive force decreases to zero are 43 Å, 50 Å, 65 Å, 68 Å, and 70 Å for the cases of 30K, 100K, 300K, 500K, and 700K, respectively.

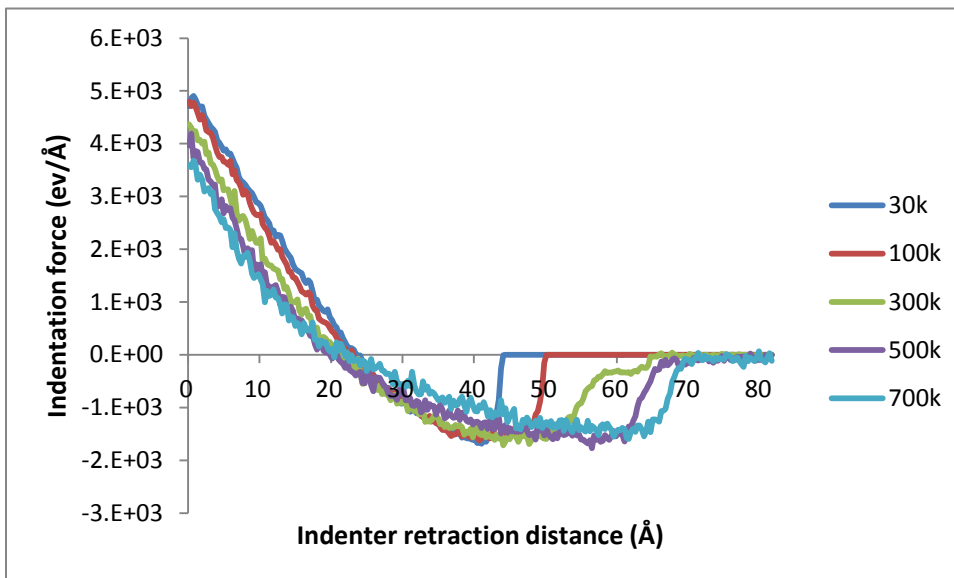


Figure 5.14. Indentation force with respect to retraction distance during the unloading process with respect to the initial temperature

The number of bct-5 silicon atoms with respect to the tool retraction distance is obtained for all cases with varying temperature, as shown in Figure 5.15. It can be found that all curves exhibit similar trends at the beginning of unloading process, and the amount of bct-5 silicon atoms decreases as the indenter starts to retract. For each case, the amount of bct-5 silicon atoms reaches a stable value at different retraction distances. The figure shows that for higher temperatures, longer retraction distances are required for reaching the stable state of bct-5 silicon. Meanwhile, the initial temperature has significant effect on the amount of bct-5 silicon atoms in the residual indents - higher temperatures result in less amount of residual bct-5 atoms. The numbers of residual bct-5 atoms are 41930, 38655, 26660, 15695, and 11594 for the five cases with the initial temperature in ascending order.

Similarly, the number of  $\beta$ -silicon atoms with respect to the tool retraction distance is obtained for all the cases, as shown in Figure 5.16. For all the cases, the amount of  $\beta$ -silicon atoms decreases as the indenter starts to retract and reaches a stable value at different retraction distance. Similar to the evolution of amount of bct-5 atoms, longer retraction distances are required for reaching the stable state under higher temperatures. Also, the effect of temperature on the amount of residual  $\beta$ -silicon is similar to its effect on bct-5 atoms. Higher temperatures result in less amount of residual  $\beta$ -silicon atoms. The numbers of residual  $\beta$ -silicon atoms are 15124, 5306, 1316, 583, and 639 for the five cases with the initial temperature in ascending order. The result presented

here is consistent with the finding that  $\beta$ -silicon transforms back to the original Si-I and amorphous phase during the rapid unloading process (Kim and Oh, 2006).

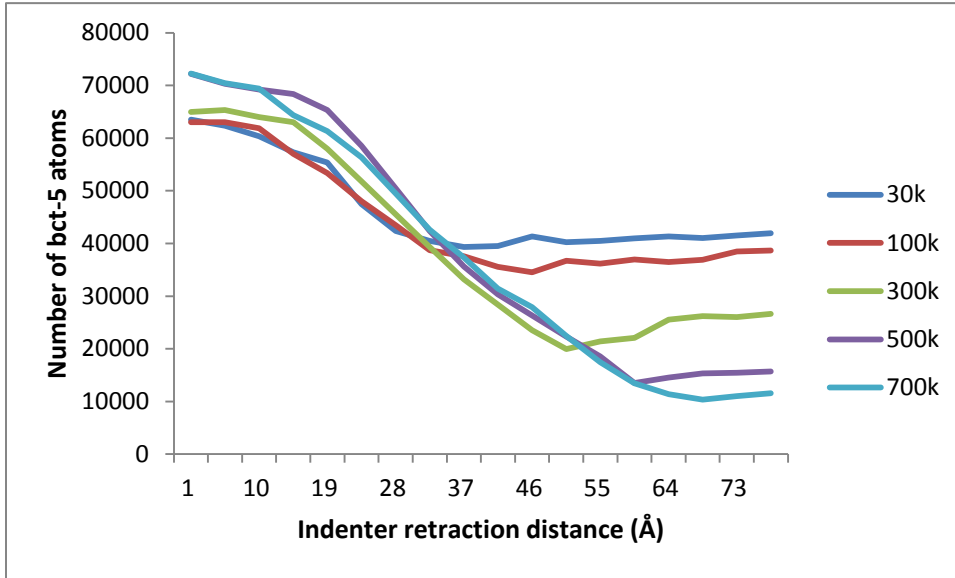


Figure 5.15. Number of atoms with bct-5 silicon phase structure with respect to indenter retraction distance

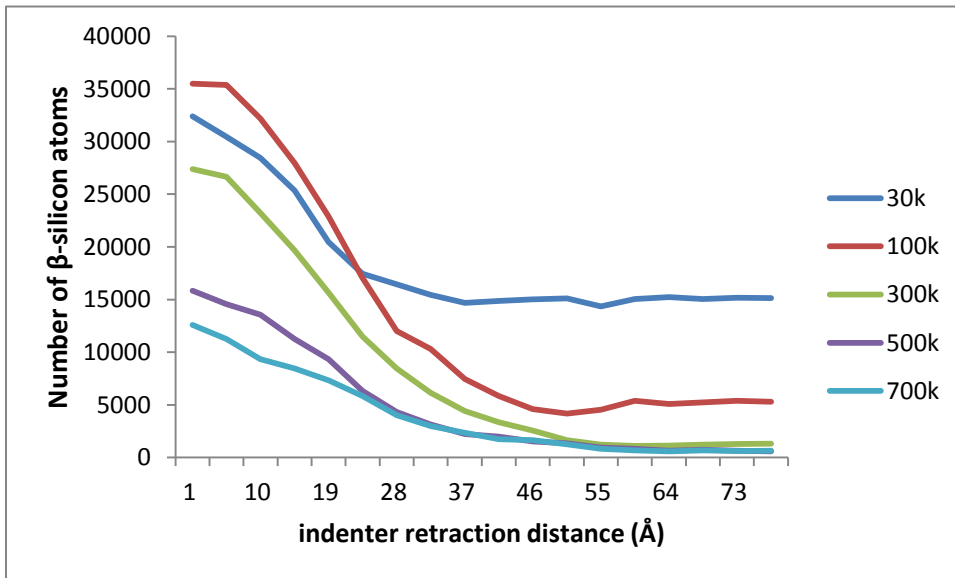


Figure 5.16. Number of atoms with  $\beta$ -silicon phase structure with respect to indenter retraction distance

Indentation morphology and phase transformation distribution after the indenter is fully retracted are shown in Figure 5.17. The comparison can be established among the cases of different initial temperature. First, the residual indentation at 30K has the largest bct-5 region. This indicates that lower temperatures are helpful in preserving bct-5 phase during unloading. More interestingly, there is a region of silicon atoms with very similar structure of original Si-I formed right underneath the indenter at fully retracted position, as circles by the black dotted line in Fig. 5.12 (a). Similar findings are discussed in literature (Mylvaganam et al., 2009; Kausala 2008). This small region of diamond structure silicon diminishes as the temperature increases. It is noted that for all the temperatures,  $\beta$ -silicon atoms no longer concentrates underneath indenter as observed from the maximum indentation position. Instead,  $\beta$ -silicon atoms are mixed with bct-5 atoms, Si-I and few amount of other low-coordinated silicon atoms (labeled by dark green color). A mixture of these silicon atoms does not own a fixed crystalline arrangement structure or a long-range order, and thus it is considered as amorphous silicon. Residual indentations under higher temperatures exhibit more significant amorphous characteristics.

The residual indentation depth is also found to be temperature dependent. For the five cases with the initial temperature in ascending order, the residual indentation depths are measured to be 36 Å, 28 Å, 23 Å, 22 Å, and 19 Å, respectively. The reduction of residual indentation depth is believed to be caused by the indenter/workpiece adhesive

effect, because the obvious material/indenter sticking phenomenon is seen for 500K and 700K. The implication is that low temperatures are helpful to preserve the indentation geometry during tool retraction by reducing the atom adhesion effect between the indenter and work piece. This finding might be of interest for the tool-based ultra-precision manufacturing, where the tight control of deformation geometry is often called for.

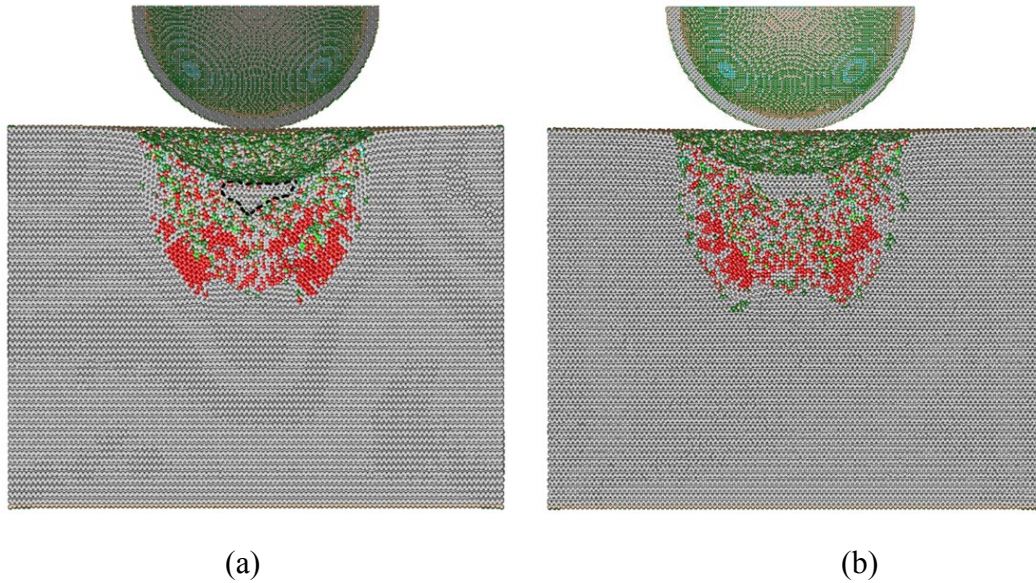


Figure 5.17. Residual indentation morphologies and phase transformation distributions at the initial temperatures of (a) 30K, (b) 100K, (c) 300K, (d) 500K, and (e) 700K

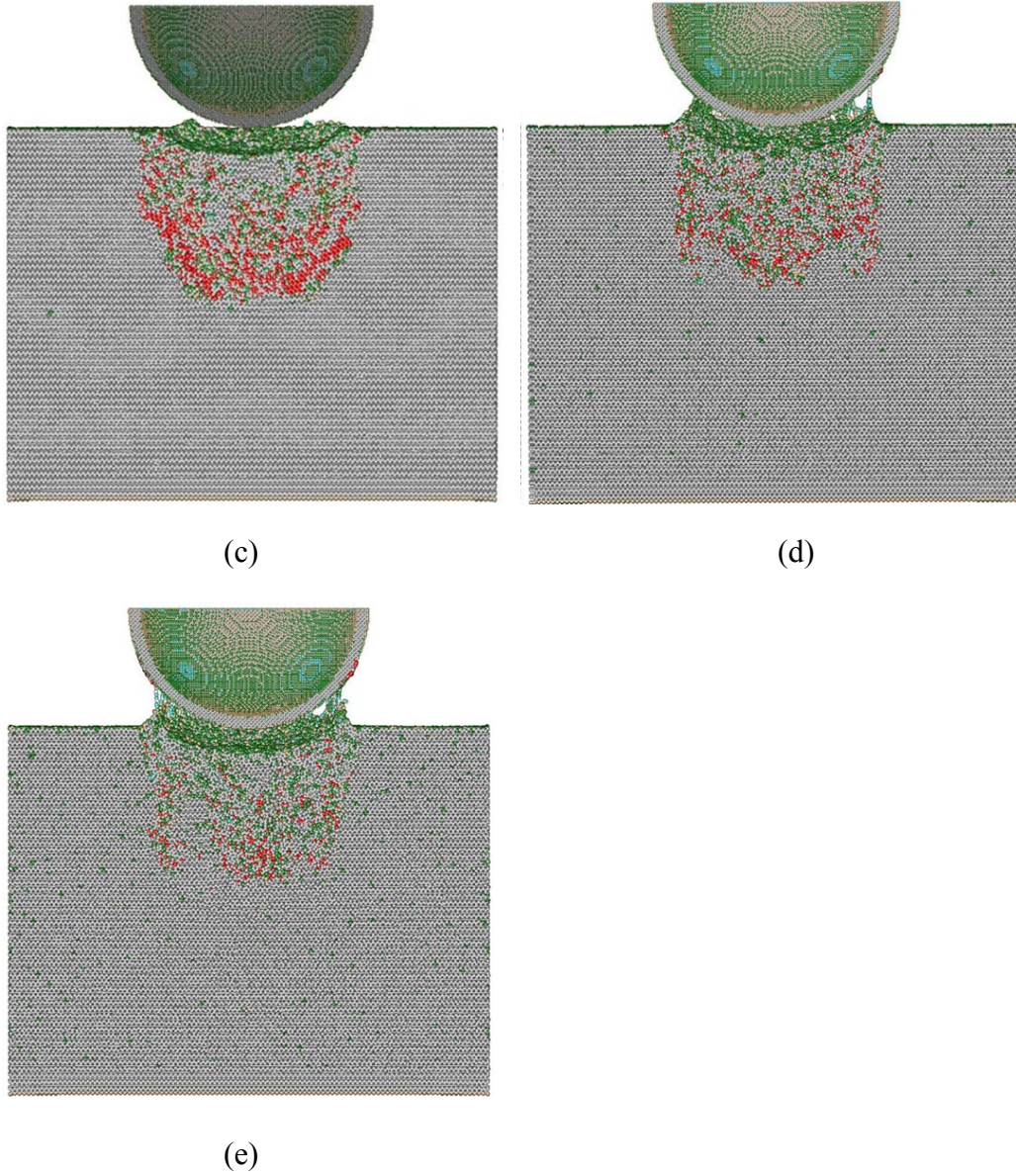


Figure. 5.17. Residual indentation morphologies and phase transformation distributions at the initial temperatures of (a) 30K, (b) 100K, (c) 300K, (d) 500K, and (e) 700K (Continued)

## CHAPTER 6. GRAIN SIZE EFFECT ON NANO-INDENTATION OF POLYCRYSTALLINE SILICON

In this chapter, the effect of grain size on the indentation force and phase transformation is discussed. Five polycrystalline silicon workpieces with various grain sizes are constructed. By applying the Voronoi grain division scheme, the five polycrystalline silicon workpieces contain 8, 32, 64, 144, and 256 grains, respectively. With the identical dimension of  $40 \times 30 \times 30 \text{ nm}^3$ , the equivalent grain sizes for the five cases can be calculated as 20.48, 12.9, 10.24, 7.81, and 6.45 nm. The corresponding ratios between boundary atoms and bulk atoms are 1.4%, 4.2%, 7.9%, 12.3%, and 14.3%. The detailed specification of each polycrystalline silicon workpiece is shown in Table 6.1. The comparison between the results of polycrystalline and monocrystalline silicon under the same indentation condition is also performed. The initial temperature is set at 300K. The identical indentation depth is used for all simulation cases.

Table 6.1. Structural information for polycrystalline copper workpieces

Number of grains	8	32	64	144	256
Total Atoms	1,845,842	1,839,081	1,834,926	1,828,228	1,822,040
% grain atoms	98.6	95.8	92.1	87.7	85.7
$\frac{\text{GrainBoundaryAtoms}}{\text{BulkAtoms}}$	1.4	4.2	7.9	12.3	14.3

### 6.1. Effect of grain size on indentation force

Figure 6.1 depicts the indentation force evolution for polycrystalline silicon with varying grain sizes (20.48 nm, 12.9nm, 10.24nm, 7.81nm, 6.45nm) and monocrystalline silicon. It can be observed that for all the cases, the indentation force stays around zero within the indenter offset distance ( $5\text{\AA}$ ), and then it almost increases linearly throughout the entire indentation process. However, the grain size has significant effect on the magnitude of indentation force. The maximum indentation force is inversely proportional to the grain size, and the monocrystal case produces the largest maximum indentation force. The maximum indentation force is calculated by averaging all data points of last 1nm of indentation depth, the results are presented in Figure 6.2. The maximum indentation force of  $4300\text{ ev/\AA}$  is obtained for the case of monocrystal silicon, while the polycrystalline cases with the grain sizes of 20.48nm, 12.9nm, 10.24nm, 7.81nm, and 6.45nm results in the indentation forces of 3958, 3789, 3765 and  $3591\text{ ev/\AA}$ , respectively.

For most metals, Hall-Petch relation has been reported - material yield stress increases as grain size decreases. However, this phenomenon is not seen in our simulation of silicon indentation. Shi et al. (2013) adopt MD simulation method to investigate the grain size effect in the nano-machining process of copper, and observe the Hall-Petch to inverse Hall-Petch transition at the critical grain size of about 14 nm. When the grain size is larger than 14 nm, the cutting force increases as the grain size decreases; while when grain size becomes less than 14 nm, the cutting force decreases as the grain

size further decreases. In their study, the dislocation-grain boundary interaction shows that the resistance of grain boundary to dislocation movement is the fundamental mechanism of the Hall-Petch relation, while the grain boundary diffusion and movement is the driving force for the inverse Hall-Petch relation. Similarly, experimental studies for most metals reveal that the critical grain size of Hall-Petch to inverse Hall-Petch transition is in the range of 10-15 nm. However, for silicon, a typical brittle non-metal material, there is a lack of investigation about the dependence of material strength on grain size, especially when grain size reduces to nano-scale.

In the present study of nano-indentation of silicon, the normal Hall-Petch relation part is not seen for grain sizes ranging from 20nm to 6.45 nm - the indentation force continuously decreases as the grain size decreases. The reason why normal Hall-Petch does not occur is that the stress induced phase transformation of polycrystalline silicon impedes the formation of dislocations, and thus there is no dislocation-grain boundary interaction, which is the fundamental cause of grain boundary strengthening in most metal materials. Similar observation is reported by Shi (2006), in which the phase transformation as observed in silicon cutting process is the distinguishing difference between silicon machining and copper machining.

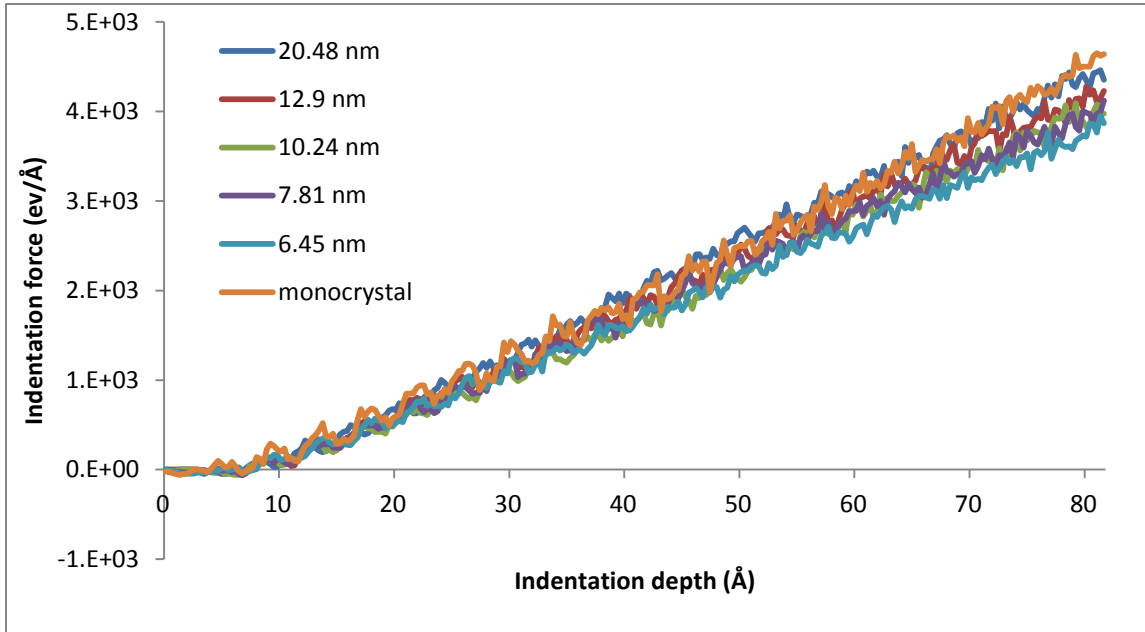


Figure 6.1. Indentation force with respect to indentation depth for different grain sizes

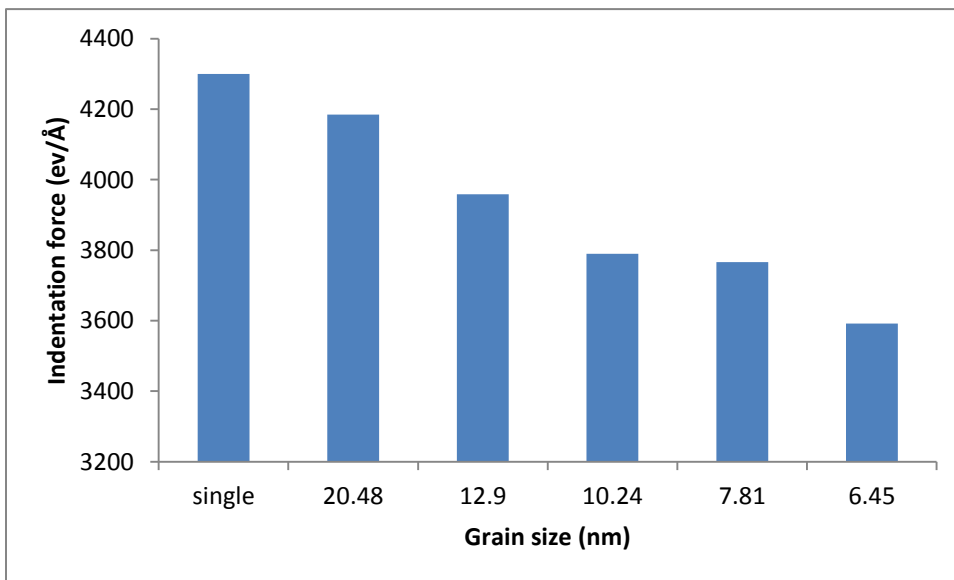


Figure 6.2. Maximum indentation force with respect to grain size

## 6.2. Effect of grain size on equivalent stress

Figure 6.3 presents the snapshots (maximum indentation depth) of equivalent stress distribution for the five polycrystalline cases with different grain sizes. For all the cases, the maximum equivalent stress is found to be in the vicinity of indenter/workpiece interface, and it takes the values of 83, 86, 82, 82, and 83 GPa for the cases with the grain sizes of 20.48, 12.9, 10.24, 7.81, and 6.45nm respectively. The dependence of maximum equivalent stress on grain size seems to be insignificant, and the small deviation of maximum equivalent stress might be induced by different crystal orientations within the grains. Also, the magnitude of stress value change is less drastic compared to the indentation force. Meanwhile, the results indicate that the equivalent stress on grain boundaries is generally 30%-60% higher than the stress inside the grains. Note that the difference of equivalent stress in grain boundaries and inside grain is not only caused by the exertion of indentation force. It is believed that the crystallographic orientation of grains could introduce stress concentration nearby boundaries. Literature also indicates that higher amount of stress and lattice distortion can develop nearby the grain boundaries (Nieh, 2005).

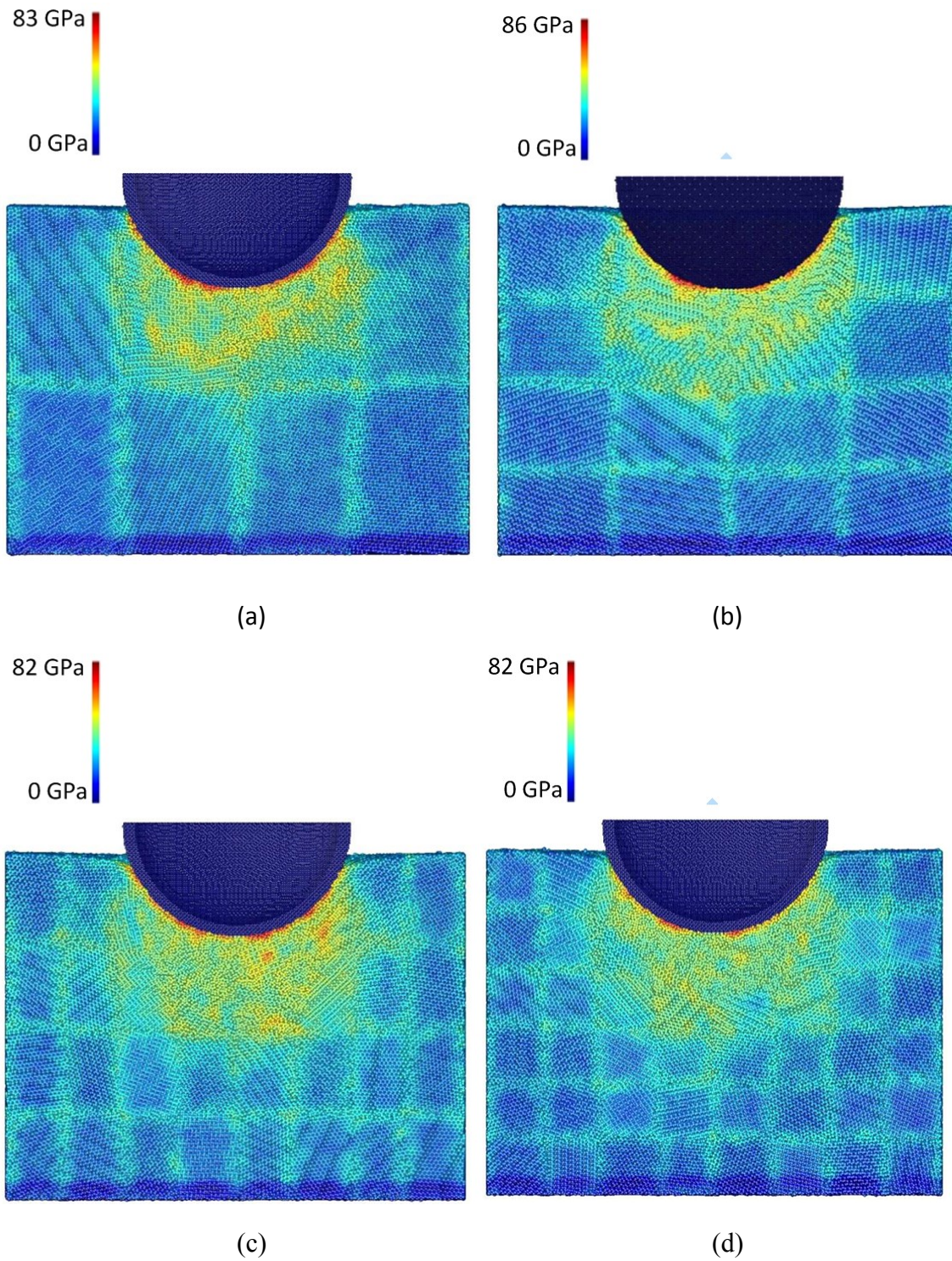
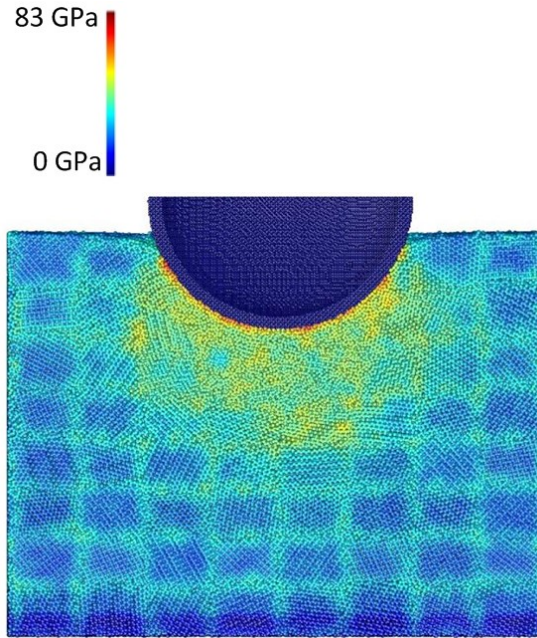


Figure 6.3. Equivalent stress distributions in indentation polycrystalline silicon with different grain sizes: (a) 20.48nm (b) 12.9nm (c) 10.24nm (d) 7.81nm and (e) 6.45nm



(e)

Figure 6.3. Equivalent stress distributions in indentation polycrystalline silicon with different grain sizes: (a) 20.48nm (b) 12.9nm (c) 10.24nm (d) 7.81nm and (e) 6.45nm (Continued)

### 6.3. Effect of grain size on phase transformation

Fig 6.3 shows the distribution of bct-5 silicon and  $\beta$ -silicon under maximum indentation. It can be found that phase transformation inside polycrystalline silicon is different from that inside monocrystal silicon, as compared with Figure 5.7 (c). In the indentation of monocrystal silicon,  $\beta$ -silicon mainly concentrates at the center of phase transformation region, about 10 - 20 Å underneath the indenter, surrounded by large amount of bct-5 silicon atoms. However in case of polycrystalline silicon indentation, the distribution of  $\beta$ -silicon atoms exhibits more random characteristic, they no longer concentrate at the center of phase transformation zone. More importantly, in all

polycrystalline cases, although all the  $\beta$ -silicon atoms are characterized based on RDF, they do not exhibit long-range order. Instead, they are mixed with Si-I atoms, bct-5 atoms and grain boundary atoms. As a result, the mixture of different silicon phases is considered amorphous silicon. Meanwhile, Figure 6.4 shows that the distribution of bct-5 silicon atoms significantly depends upon the grain size because the bct-5 silicon concentration region has different sizes and shapes for different grain sizes. In the phase transformation region, more concentration of bct-5 silicon is observed with the increase of grain size. Stress and crystal orientation variation in the vicinity of grain boundaries are believed to cause the variation in formation and distribution of bct-5 silicon.

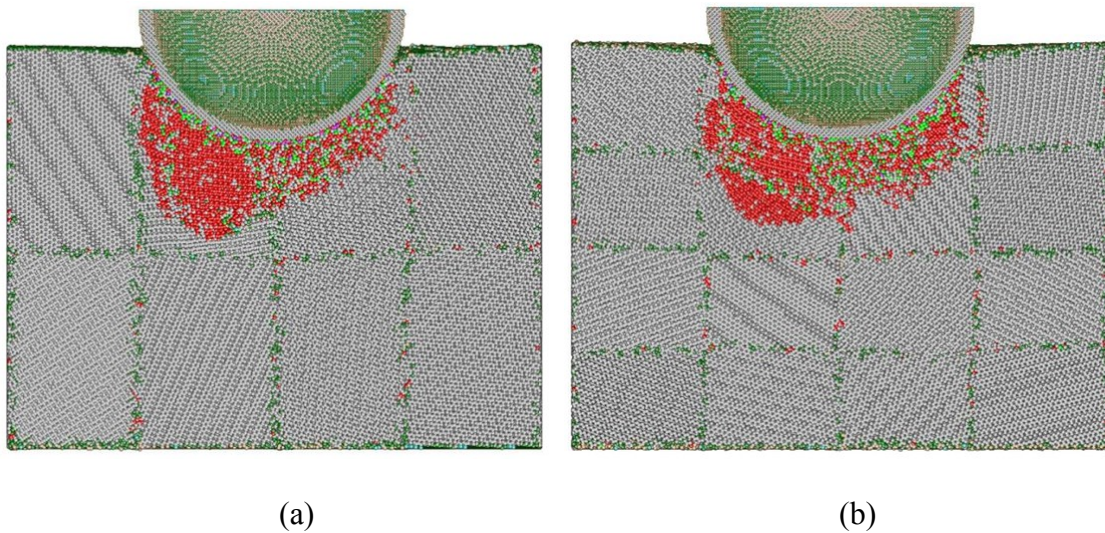
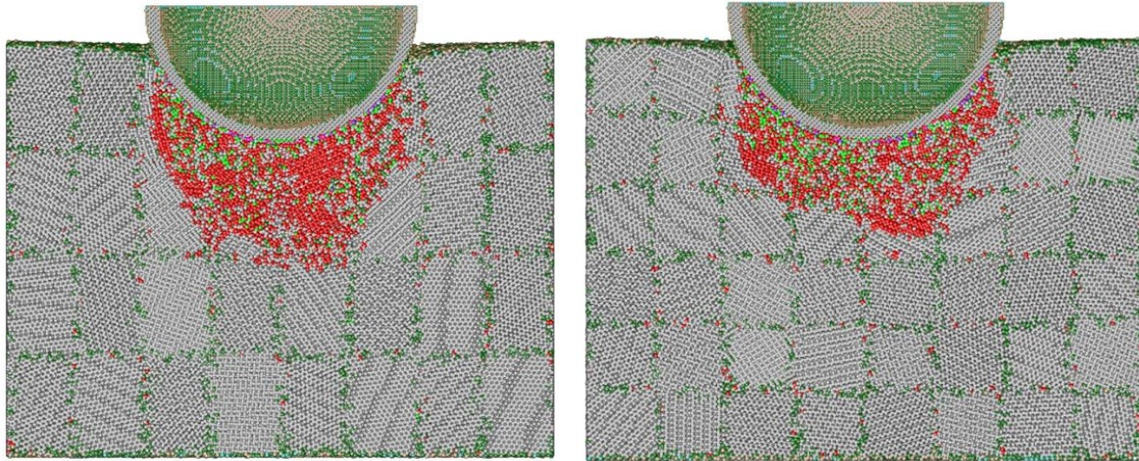
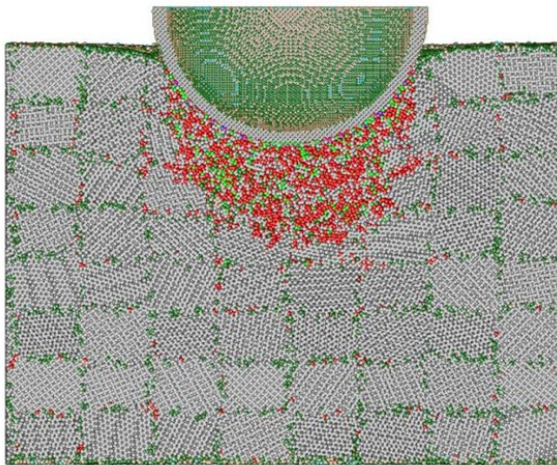


Figure 6.4. Phase transformation in indentation process of polycrystalline silicon workpieces with different grain sizes, (a) 20.48nm, (b) 12.9nm, (c) 10.24nm, (d) 7.81nm, and (e) 6.45nm \*Red color indicates bct-5 atoms and green color indicates  $\beta$ -silicon atoms.



(c)

(d)



(e)

Figure 6.4. Phase transformation in indentation process of polycrystalline silicon workpieces with different grain sizes, (a) 20.48nm, (b) 12.9nm, (c) 10.24nm, (d) 7.81nm, and (e) 6.45nm \*Red color indicates bct-5 atoms and green color indicates  $\beta$ -silicon atoms (Continued)

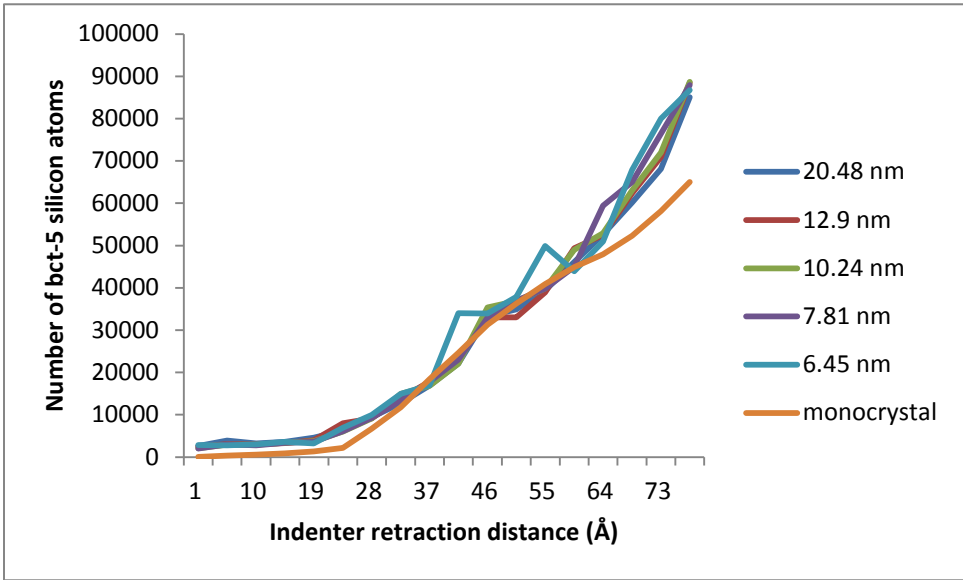


Figure 6.5. Effect of grain size on the formation of bct-5 silicon during loading

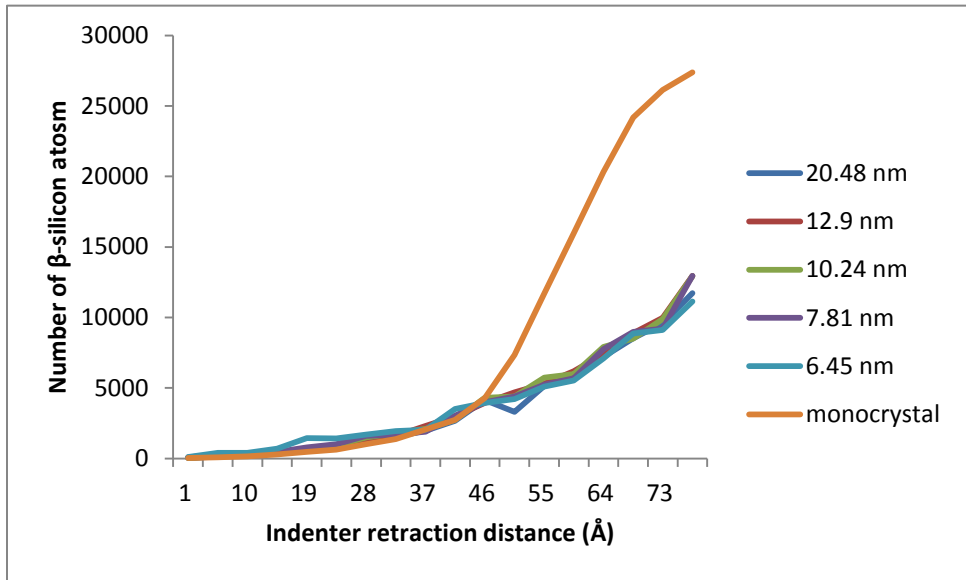


Figure 6.6. Effect of grain size on the formation of  $\beta$ -silicon atoms during loading

Figure 6.5 presents the effect of grain size on the formation of bct-5 atoms during the entire loading process. In all the cases of polycrystalline silicon indentation, there is

no significant deviation in terms of the amount of bct-5 silicon atoms. The polycrystalline silicon with a grain size of 10.24 nm has the highest number of bct-5 atoms and that with a grain size of 20.2 nm has the lowest bct-5 atom number. For all the polycrystalline cases, the number of bct-5 atoms is in the range of 76,000 to 80,000. However, for the indentation made on monocrystal silicon, the number of bct-5 atoms is about 65,000, which is 14-18% less than those of polycrystalline workpieces. Meanwhile, the number of  $\beta$ -silicon atoms is also obtained and shown in Figure 6.6. For the polycrystalline silicon cases, the trend of  $\beta$ -silicon evolution is similar to that of bct-5 silicon. The grain size of 10.24 nm corresponds to the highest number of  $\beta$ -silicon atoms and the grain size of 20.2 nm corresponds to the lowest. The number of  $\beta$ -silicon atoms is in the range of 11,000 to 12,800. However, the number of  $\beta$ -silicon in the monocrystal silicon is the largest, which is 110% more than the  $\beta$ -silicon number in the polycrystal silicon cases.

The stress difference is believed to cause the deviation in the amount of phase transformation during the indentations of monocrystal and polycrystalline silicon. Figure 6.7 presents the cross sectional views of stress distribution taken from 20 Å underneath the indenter for two cases, namely a polycrystalline silicon case (grain size 20.48 nm) and the monocrystal silicon case. There is slight difference of the maximum equivalent stress. However, the distribution of equivalent stress is different. In the indentation of monocrystal silicon, the local low-stress zones can be clearly seen. They are the small low-stress zone at the center, and the four surrounding low-stress zones. However, in the

indentation of polycrystalline silicon, no local low-stress zone is found underneath the indenter. It might be attributed to the existence of grain boundaries. The grain boundaries between adjacent grains impede the deformation of materials under indentation, and this results in stress elevation inside work material. Meanwhile, based on the analysis in the previous chapter, it is already known that  $\beta$ -silicon forms at the equivalent stress of around 39 GPa, and bct-5 silicon forms at the higher equivalent stress of 45-55 GPa at 300K. It is clear that the stress elevation causes the reduction of  $\beta$ -silicon phase and the increase of bct-5 silicon phase.

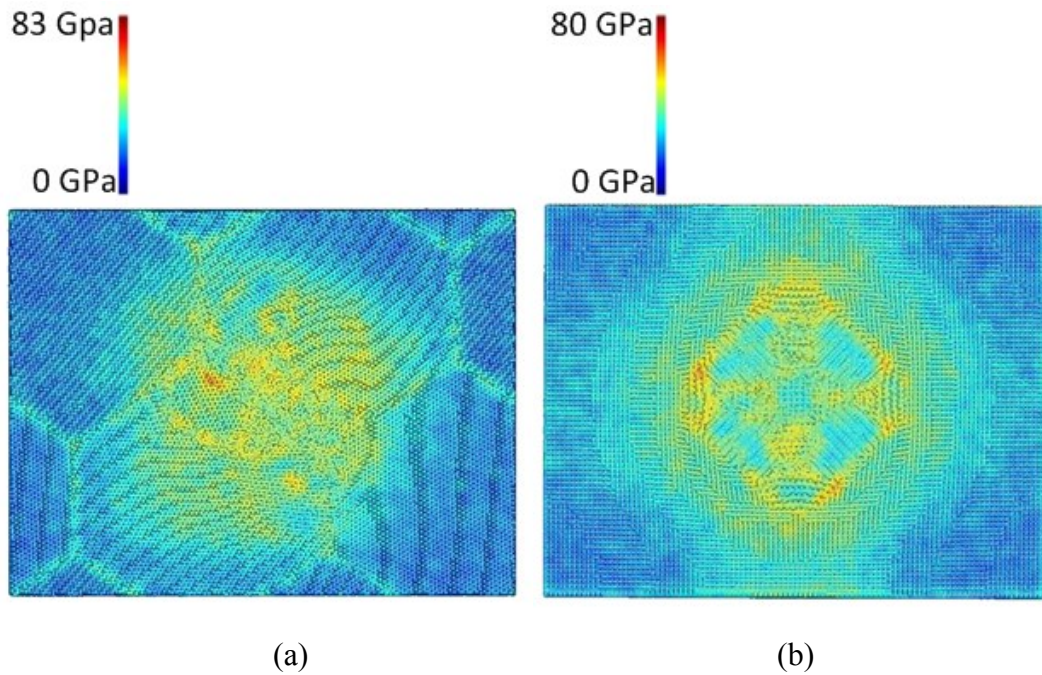


Figure 6.7. Comparison of equivalent stress distributions for (a) polycrystalline silicon with grain size of 20.48 nm (b) monocrystalline silicon

#### **6.4. Grain size effect on stress distribution on indenter/workpiece interface**

The distributions of tangential force with respect to different grain size are presented in Figure 6.8. The six curves exhibit similar trends with the increase of “arc distance to the indenter tip”, normal force first increases along the interface and then quickly decreases to zero when the work material and indenter cease to be in contact. Overall, the normal force decreases with the decrease of grain size along the entire interface.

Meanwhile, the tangential force distributions along the indenter/work interface at maximum indentation depth with respect to different grain sizes are obtained as well, as shown in Figure 6.9. Compared to the normal force distribution, the tangential force distributions exhibit more randomness and fluctuation, especially for the cases of larger grain sizes (e.g., 20.48 and 12.9 nm). Due to the anisotropy of crystalline materials, significant deviation of tribological performance among grains is believed to be the reason of tangential force fluctuation on the contact interface. Meanwhile, further decrease of grain size in a way alleviates the crystal anisotropy so that less fluctuation of tangential force is seen on the interface. The effect of grain size on the maximum tangential force is insignificant.

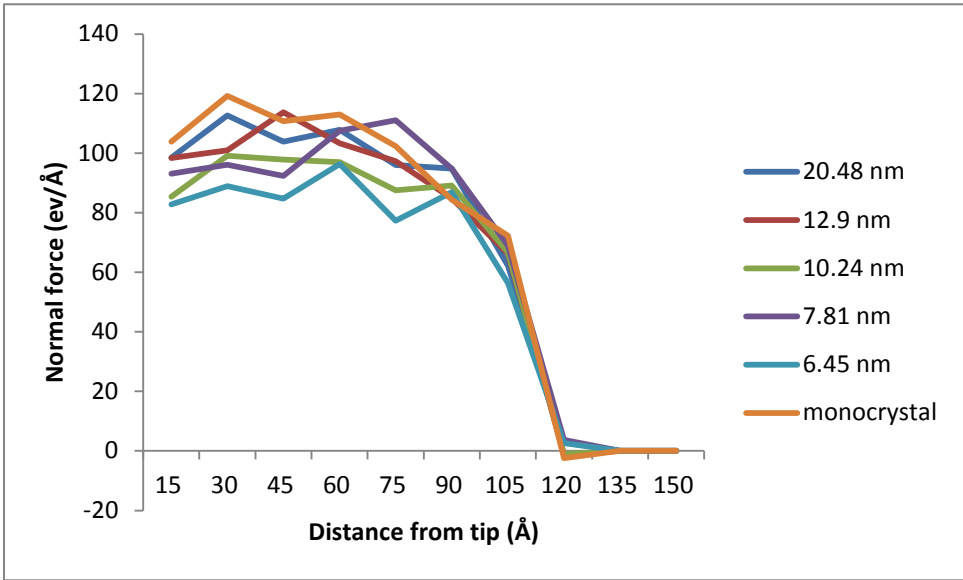


Figure 6.8. Grain size effect on the normal force distribution on the indenter/workpiece interface

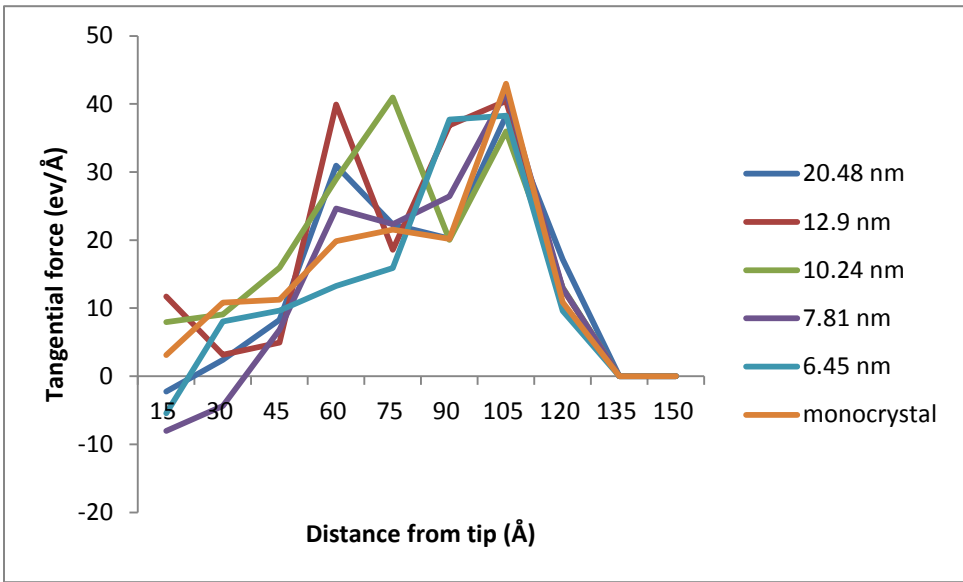


Figure 6.9. Grain size effect on the tangential force distribution on the indenter/workpiece interface

### 6.5. Grain size effect on unloading process

Figure 6.10 presents the indentation force evolutions for the cases of different grain sizes during unloading process at the initial temperature of 300K. It is seen that for all the polycrystalline cases, the evolution of indentation force during unloading is similar - the indentation force decreases almost linearly as the indenter starts to retract and reaches equilibrium state at the retraction distance of about 20 Å. The indentation force turns to be adhesive as the indenter further retracts, and the maximum adhesive force of 1,700 ev/Å occurs at the retraction distance of around 47 Å. Thereafter, the adhesive force quickly decreases to zero at around 55 Å.

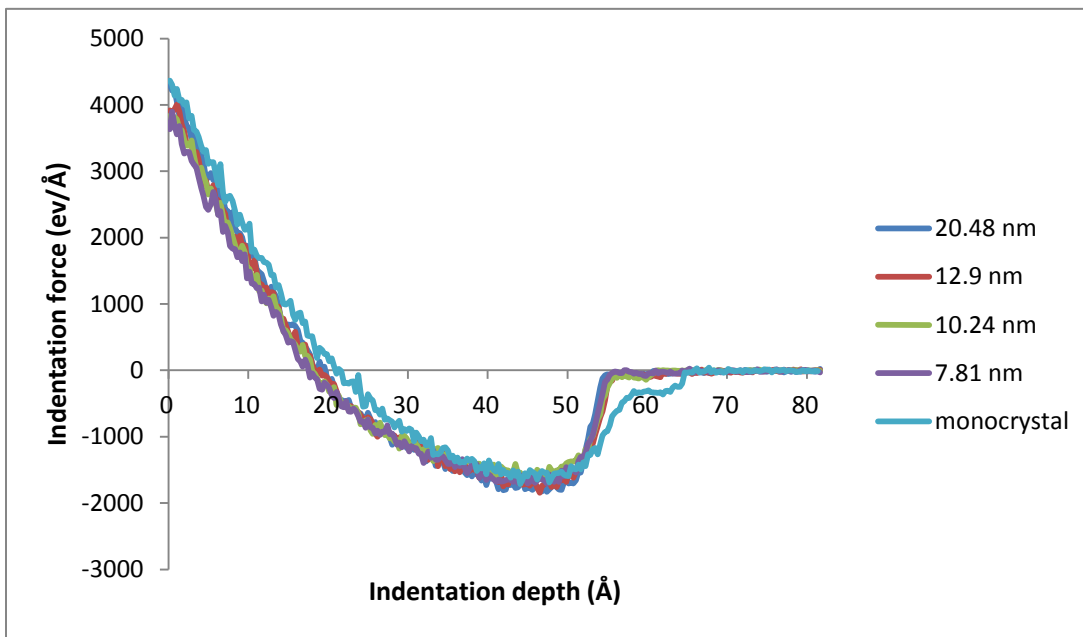


Figure 6.10. Indentation force vs. depth during unloading process with respect to different grain size

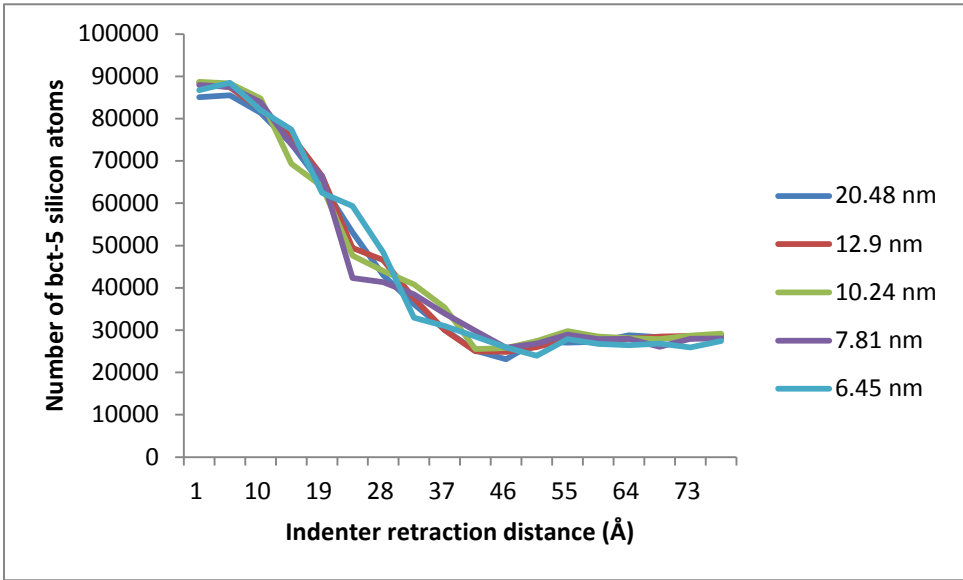


Figure 6.11. Effect of grain size on the formation of bct-5 silicon during unloading

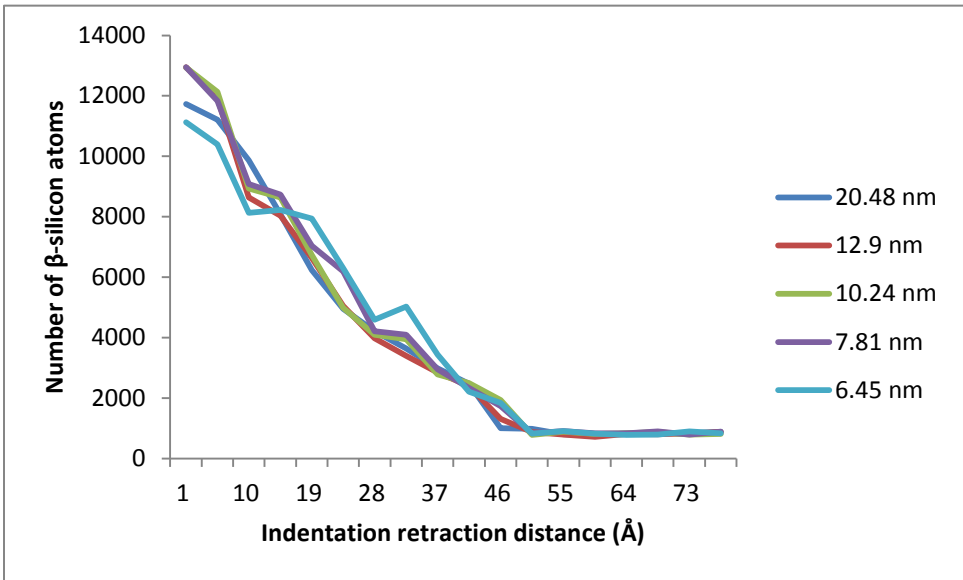


Figure 6.12. Effect of grain size on the formation of beta-silicon during unloading

Figures 6.11 and 6.12 illustrate the evolutions of bct-5 silicon and beta-silicon atom numbers, respectively. Both figures show good consistency for all curves - the number of

bct-5 silicon atoms decreases to a stable value of about 28,000 at the tool travel distance of 47 Å, and the amount of  $\beta$ -silicon atoms decreases to around 800 at the same tool travel distance. Overall, the grain size ranging from 6.45 nm to 20.48 nm hardly affects the phase transformation during loading and unloading process. However, compared with the monocrystal silicon, the grain boundaries of polycrystalline silicon help increase the local stress, thus decrease the formation of  $\beta$ -silicon.

## CHAPTER 7. CONCLUSIONS AND FUTURE RESEARCH

### 7.1. Conclusions

This thesis research mainly employs MD simulation to study the nano-indentation process of silicon materials. First of all, AFM nano-indentation experiment is performed to verify the capability of MD simulation in modeling nano-indentation of silicon. The indentation forces obtained from AFM nano-indentation experiment and MD simulation show good agreement. The residual indentation morphologies produced by MD simulation and AFM experiment are also consistent. The comparison results successfully validate the accuracy of MD model in simulating the nano-indentation of silicon.

Thereafter, the simulation is configured with five different initial temperatures, namely, 30K, 100K, 300K, 500K and 700K. Meanwhile, the research also investigates the effect of grain size on the nano-indentation process. For this purpose, five simulation cases are constructed for the polycrystalline structures with equivalent grain sizes of 20.48, 12.9, 10.24, 7.81, and 6.45 nm, respectively. The major findings are summarized as follows,

#### 1. Temperature effect

- i. When the initial temperature is lower than 500K, the distribution of phase transformation exhibits obvious anisotropic and symmetric patterns.  $\beta$ -silicon concentrates in the center of phase transformation region and several larger areas around the center. Bct-5 silicon forms along  $\langle 110 \rangle$  crystal direction and divides the surrounding  $\beta$ -silicon into four separate regions. Above 500K, the

distributions of the two metastable phases exhibit more randomness, and a mixture of the two phases is observed in the phase transformation zone.

- ii. By comparing the phase transformation and equivalent stress distributions, it is found that the equivalent stress distribution can approximately define the distributions of bct-5 silicon and the  $\beta$ -silicon.
- iii. Higher initial temperature results in the earlier formation of bct-5 silicon and  $\beta$ -silicon. At the maximum indentation position, the numbers of bct-5 silicon atoms under different temperatures do not deviate much. However,  $\beta$ -silicon atoms are significantly less at higher temperatures.
- iv. The critical equivalent stress for the formation of bct-5 silicon is around 44 GPa, independent of temperature. However, the critical stress for the formation of  $\beta$ -silicon is significantly affected by the initial temperature, and the values are 34, 36, 39, 43, and 46 GPa for the simulation cases of 30, 100, 300, 500, and 700K, respectively.
- v. In the unloading process, it is observed that lower temperatures can eliminate the sticking phenomenon on the indenter/workpiece interface. This is helpful to the preservation of residual indentation morphology.
- vi.  $\beta$ -silicon and bct-5 silicon transform to the original Si-I and amorphous structure upon unloading, and this transition can be restrained under low temperatures.

## 2. Grain size effect

- i. The highest indentation force is seen in the indentation of monocrystal silicon compared with all the polycrystalline silicon materials. The indentation force decreases as the grain size decreases. The stress induced phase transformation of polycrystalline silicon impedes the formation of dislocations, thus eliminates dislocation-grain boundary interaction.
- ii. The distribution of bct-5 silicon atoms exhibits significant grain size dependency. In the phase transformation region, higher concentration of bct-5 silicon is observed in larger grains. The stress and crystal orientation variations in the vicinity of grain boundaries are believed to cause the variation of formation and distribution of bct-5 silicon.
- iii. There is no significant deviation in terms of the number of bct-5 silicon atoms at the maximum indentation position for all polycrystalline cases. However, for the indentation of monocrystal silicon, the number of bct-5 atoms is 14-18% less than those of polycrystalline workpieces.
- iv. The distribution of  $\beta$ -silicon atoms exhibits more random characteristics. For instance,  $\beta$ -silicon atoms no longer concentrate in the center of phase transformation zone. The number of  $\beta$ -silicon atoms formed in the indentation of polycrystalline silicon is 110-120% less than that formed in monocrystal silicon.

- v. Stress elevation caused by grain boundaries is the cause of less formation of  $\beta$ -silicon and slightly more bct-5 silicon in the indentation of polycrystalline silicon.

## 7.2. Future research

Based on the findings obtained in the thesis research, we believe that the following items deserve consideration to further advance the understanding of silicon phase transformation in nano-manufacturing process.

- i. Although the stress distribution and phase transformation are studied in depth for nano-indentation process, there is a need for further investigation in more complex manufacturing processes, such as nano-machining and nano-scratching.
- ii. More experimental validation is expected in validating the distribution of  $\beta$ -silicon and bct-5 silicon.
- iii. In the nano-manufacturing processes of brittle materials, a link between phase transformation and surface residual stress should be established.
- iv. Further research is needed to reveal the grain size effect on the mechanical properties of polycrystalline silicon with grain size larger than 20 nm.
- v. Due to the limit of computational resources, MD simulation can only be applied in the investigation under nano/atomistic scale. A combination of MD simulation

and other conventional modelling tools (e.g., FEM) is called for more effectively analyzing the manufacturing processes at larger scales.

## REFERENCES

- Alder, B. J., & Wainwright, T. (1957). Phase transition for a hard sphere system. *The Journal of Chemical Physics*, 27(5), 1208-1209.
- Bradby, J. E., Williams, J. S., Wong-Leung, J., Swain, M. V., & Munroe, P. (2000). Transmission electron microscopy observation of deformation microstructure under spherical indentation in silicon. *Applied Physics Letters*, 77(23), 3749-3751.
- Bundy, F. P. (1964). Phase diagrams of silicon and germanium to 200 kbar, 1000 C. *The Journal of Chemical Physics*, 41, 3809.
- Crain, J., Ackland, G. J., Maclean, J. R., Piltz, R. O., Hatton, P. D., & Pawley, G. S. (1994). Reversible pressure-induced structural transitions between metastable phases of silicon. *Physical Review B*, 50(17), 13043.
- Cheong, W. C. D., & Zhang, L. C. (2000). Molecular dynamics simulation of phase transformations in silicon monocrystals due to nano-indentation. *Nanotechnology*, 11(3), 173.
- Cai, M. B., Li, X. P., & Rahman, M. (2007). Characteristics of “dynamic hard particles” in nanoscale ductile mode cutting of monocrystalline silicon with diamond tools in relation to tool groove wear. *Wear*, 263(7), 1459-1466.
- Cai, M. B., Li, X. P., & Rahman, M. (2007). High-pressure phase transformation as the mechanism of ductile chip formation in nanoscale cutting of silicon wafer. *Proceedings of the Institution of Mechanical Engineers, Part B: Journal of Engineering Manufacture*, 221(10), 1511-1519.
- Cai, M. B., Li, X. P., & Rahman, M. (2007). Study of the temperature and stress in nanoscale ductile mode cutting of silicon using molecular dynamics simulation. *Journal of materials processing technology*, 192, 607-612.
- Cheung, D. L. G. (2002). Structures and properties of liquid crystals and related molecules from computer simulation (Doctoral dissertation, Durham University).
- Donadio, D., & Galli, G. (2010). Temperature dependence of the thermal conductivity of thin silicon nanowires. *Nano letters*, 10(3), 847-851.

- Fang, F. Z., Wu, H., Zhou, W., & Hu, X. T. (2007). A study on mechanism of nano-cutting single crystal silicon. *Journal of materials processing technology*, 184(1), 407-410.
- Gradeen, A. G., Spelt, J. K., & Papini, M. (2012). Cryogenic abrasive jet machining of polydimethylsiloxane at different temperatures. *Wear*, 274, 335-344.
- Gridneva, I. V., Milman, Y. V., & Trefilov, V. I. (1972). Phase transition in diamond - structure crystals during hardness measurements. *Physica status solidi (a)*, 14(1), 177-182.
- Gerbig, Y. B., Stranick, S. J., & Cook, R. F. (2011). Direct observation of phase transformation anisotropy in indented silicon studied by confocal Raman spectroscopy. *Physical Review B*, 83(20), 205209.
- Gerbig, Y. B., Stranick, S. J., & Cook, R. F. (2010). Measurement of residual stress field anisotropy at indentations in silicon. *Scripta Materialia*, 63(5), 512-515.
- Hu, J. Z., Merkle, L. D., Menoni, C. S., & Spain, I. L. (1986). Crystal data for high-pressure phases of silicon. *Physical Review B*, 34(7), 4679.
- Hu, J. Z., & Spain, I. L. (1984). Phases of silicon at high pressure. *Solid state communications*, 51(5), 263-266.
- Han, X., Hu, Y., & Yu, S. (2009). Investigation of material removal mechanism of silicon wafer in the chemical mechanical polishing process using molecular dynamics simulation method. *Applied Physics A*, 95(3), 899-905.
- Jamieson, J. C. (1963). Crystal structures at high pressures of metallic modifications of silicon and germanium. *Science*, 139(3556), 762-764.
- Jang, H., & Farkas, D. (2007). Interaction of lattice dislocations with a grain boundary during nanoindentation simulation. *Materials Letters*, 61(3), 868-871.
- Khayyat, M. M., Banini, G. K., Hasko, D. G., & Chaudhri, M. M. (2003). Raman microscopy investigations of structural phase transformations in crystalline and amorphous silicon due to indentation with a Vickers diamond at room temperature and at 77 K. *Journal of Physics D: Applied Physics*, 36(11), 1300.

- Kunz, R. R., Nitishin, P. M., Clark, H. R., Rothschild, M., & Ahern, B. (1995). Observation of a nanocrystalline - to - amorphous phase transition in luminescent porous silicon. *Applied physics letters*, 67(12), 1766-1768.
- Kim, D. E., & Oh, S. I. (2006). Atomistic simulation of structural phase transformations in monocrystalline silicon induced by nanoindentation. *Nanotechnology*, 17(9), 2259.
- Koch, C. C. (2003). Optimization of strength and ductility in nanocrystalline and ultrafine grained metals. *Scripta Materialia*, 49(7), 657-662.
- Kim, J., Park, S., Lee, J. E., Jin, S. M., Lee, J. H., Lee, I. S., & Hyeon, T. (2006). Designed fabrication of multifunctional magnetic gold nanoshells and their application to magnetic resonance imaging and photothermal therapy. *Angewandte Chemie*, 118(46), 7918-7922.
- Lin, Y. H., Chen, T. C., Yang, P. F., Jian, S. R., & Lai, Y. S. (2007). Atomic-level simulations of nanoindentation-induced phase transformation in mono-crystalline silicon. *Applied Surface Science*, 254(5), 1415-1422.
- Li, M., & Reece, M. J. (2000). Influence of Grain Size on the Indentation - Fatigue Behavior of Alumina. *Journal of the American Ceramic Society*, 83(4), 967-970.
- Lim, Y. Y., & Chaudhri, M. M. (2002). The influence of grain size on the indentation hardness of high-purity copper and aluminium. *Philosophical Magazine A*, 82(10), 2071-2080.
- Lu, K., & Sui, M. L. (1993). An explanation to the abnormal Hall-Petch relation in nanocrystalline materials. *Scripta metallurgica et materialia*, 28(12), 1465-1470.
- Li, J. (2003). "AtomEye: an efficient atomistic configuration viewer." *Modeling and Simulation in Materials Science and Engineering* 11: 173-177.
- Leach, A. M., McDowell, M., & Gall, K. (2007). Deformation of Top - Down and Bottom - Up Silver Nanowires. *Advanced Functional Materials*, 17(1), 43-53.
- Misiuk, A. (2000). High pressure-high temperature treatment to create oxygen nano-clusters and defects in single crystalline silicon. *Mater. Phys. Mech*, 1, 119-126.

- Mylvaganam, K., Zhang, L. C., Eyben, P., Mody, J., & Vandervorst, W. (2009). Evolution of metastable phases in silicon during nanoindentation: mechanism analysis and experimental verification. *Nanotechnology*, 20(30), 305705.
- Mylvaganam, K., & Zhang, L. C. (2012). Effect of bct-5 Si on the Indentation of Monocrystalline Silicon. *Applied Mechanics and Materials*, 117, 666-669.
- Mohammadabadi, A. S., & Dehghani, K. (2008). A new model for inverse Hall-Petch relation of nanocrystalline materials. *Journal of Materials Engineering and Performance*, 17(5), 662-666.
- Morris J: The influence of grain size on the mechanical properties of steel. *Proceedings of International Symposium on Ultrafine Grained Steels, Japan, Tokyo, 2001*, Iron and Steel Institute of Japan: pp.34-41.
- Moura, C. S., & Amaral, L. (2005). Molecular dynamics simulation of silicon nanostructures. *Nuclear Instruments and Methods in Physics Research Section B: Beam Interactions with Materials and Atoms*, 228(1), 37-40.
- Narayan, J. (2000). Size and interface control of novel nanocrystalline materials using pulsed laser deposition. *Journal of Nanoparticle Research*, 2(1), 91-96.
- Nieh, T. G., & Wang, J. G. (2005). Hall-Petch relationship in nanocrystalline Ni and Be-B alloys. *Intermetallics*, 13(3), 377-385.
- Nath, N., & Chilkoti, A. (2002). A colorimetric gold nanoparticle sensor to interrogate biomolecular interactions in real time on a surface. *Analytical Chemistry*, 74(3), 504-509.
- Okonkwo, P. C., Kelly, G., Rolfe, B. F., & Pereira, M. P. (2012). The effect of temperature on sliding wear of steel-tool steel pairs. *Wear*, 282, 22-30.
- Ohira, T., Inamuro, T., & Adachi, T. (1994). Molecular dynamics simulation of amorphous silicon with Tersoff potential. *Solar energy materials and solar cells*, 34(1), 565-570.
- Pfrommer, B. G., Louie, S. G., & Cohen, M. L. (1997). Ab initio study of silicon in the R8 phase. *Physical Review B*, 56(11), 6662.
- Plimpton, S. J. (1995). "Fast Parallel Algorithms for Short-Range Molecular Dynamics." *Journal of Computational Physics* 117: 1-19.

- Qian, L., Li, M., Zhou, Z., Yang, H., & Shi, X. (2005). Comparison of nano-indentation hardness to microhardness. *Surface and Coatings Technology*, 195(2), 264-271.
- Ruffell, S., Bradby, J. E., Williams, J. S., Munoz-Paniagua, D., Tadayyon, S., Coatsworth, L. L., & Norton, P. R. (2009). Nanoindentation-induced phase transformations in silicon at elevated temperatures. *Nanotechnology*, 20(13), 135603.
- Rahman, A. (1964). Correlations in the Motion of Atoms in Liquid Argon. *Physical Review* 136(2A): A405.
- Rahman, A. and F. H. Stillinger (1974). Propagation of sound in water. A molecular-dynamics study. *Physical Review A* 10(1): 368.
- (Shi, Wang, Liu, 2004) ultra-low temperature machining
- Sun, S., Brandt, M., & Dargusch, M. S. (2010). Thermally enhanced machining of hard-to-machine materials—A review. *International Journal of Machine Tools and Manufacture*, 50(8), 663-680.
- Salehpour, B., & Omidfar, M. (2006). Temperature dependence of phase transformation pressure in silicon. *Iranian Journal of Science & Technology*, 30(A3).
- Shi, Y., (2006), A comprehensive evaluation of the nano machining process by using molecular dynamics simulation.
- Schiøtz, J., & Jacobsen, K. W. (2003). A maximum in the strength of nanocrystalline copper. *Science*, 301(5638), 1357-1359.
- Schiøtz, J. (2004). Atomic-scale modeling of plastic deformation of nanocrystalline copper. *Scripta materialia*, 51(8), 837-841.
- Sanders, P. G., Eastman, J. A., & Weertman, J. R. (1997). Elastic and tensile behavior of nanocrystalline copper and palladium. *Acta Materialia*, 45(10), 4019-4025.
- Schuh, C. A., & Nieh, T. G. (2002, January). Hardness and abrasion resistance of nanocrystalline nickel alloys near the Hall-Petch breakdown regime. In *MRS Proceedings* (Vol. 740, No. 1). Cambridge University Press.
- Schiøtz, J., Di Tolla, F. D., & Jacobsen, K. W. (1998). Softening of nanocrystalline metals at very small grain sizes. *Nature*, 391(6667), 561-563.

- Schaible, M. (1999). Empirical molecular dynamics modeling of silicon and silicon dioxide: a review. *Critical reviews in solid state and materials sciences*, 24(4), 265-323.
- Shi, J., Wang, Y. & Yang, X. (2013) Nanoscale machining of polycrystalline coppers – effects of grain size and machining parameters.
- Shi, Y. “A comprehensive evaluation of the nano machining process by using molecular dynamics simulation” MS thesis submitted to North Dakota State University, 2006
- Tang, Y., Bringa, E. M., & Meyers, M. A. (2013). Inverse Hall-Petch Relationship in Nanocrystalline Tantalum. *Materials Science and Engineering: A*.
- Tang, C. Y., & Zhang, L. C. (2005). A molecular dynamics analysis of the mechanical effect of water on the deformation of silicon monocrystals subjected to nano-indentation. *Nanotechnology*, 16(1), 15.
- Tang, Q., & Chen, F. (2006). MD simulation of phase transformations due to nanoscale cutting on silicon monocrystals with diamond tip. *Journal of Physics D: Applied Physics*, 39(16), 3674.
- Tersoff, J. (1986). New empirical model for the structural properties of silicon. *Physical Review Letters*, 56(6), 632-635.
- Tersoff, J. (1988). New empirical approach for the structure and energy of covalent systems. *Physical Review B*, 37(12), 6991.
- Urbanovich, L. I., Kramchenkov, E. M., & Chunosov, Y. N. (1992). Investigation of low-temperature gas-abrasive erosion. *Journal of Friction and Wear c/c of Trenieiznos*, 13, 80-80.
- Van Swygenhoven H, Derlet PM. (2001). Grain-boundary sliding in nanocrystalline fcc metals. *Physical Review B* 64(22):224105.
- Wang, Y., & Shi, J. (2013). A numerical study of residual stress induced in machined silicon surfaces by molecular dynamics simulation. *Applied Physics A*, DOI 10.1007/s0039-013-7977-8.
- Wei YJ, Anand L, (2004) Grain-boundary sliding and separation in polycrystalline metals: Application to nanocrystalline fcc metals. *Journal of the Mechanics and Physics of Solids*, 52(11), 2587-2616.

- Wolf, B., & Richter, A. (2003). The concept of differential hardness in depth sensing indentation. *New Journal of Physics*, 5(1), 15.
- Wang, Y., & Shi, J. (2013). Effects of water molecules on tribological behavior and property measurements in nano-indentation processes—a numerical analysis. *Nanoscale research letters*, 8(1), 1-14.
- Yang, B., & Vehoff, H. (2007). Dependence of nanohardness upon indentation size and grain size—a local examination of the interaction between dislocations and grain boundaries. *Acta materialia*, 55(3), 849-856.
- Zhang, K., Weertman, J. R., & Eastman, J. A. (2004). The influence of time, temperature, and grain size on indentation creep in high-purity nanocrystalline and ultrafine grain copper. *Applied physics letters*, 85(22), 5197-5199.
- Zapol, P., Sternberg, M., Curtiss, L. A., Frauenheim, T., & Gruen, D. M. (2001). Tight-binding molecular-dynamics simulation of impurities in ultrananocrystalline diamond grain boundaries. *Physical Review B*, 65(4), 045403.
- Zhang, L. L., Tanaka, H. H, (1998) Atomic scale deformation in silicon monocrystals induced by two-body and three-body contact sliding, *Tribology International*. 31, 425-434.
- Zhang, L. C., & Tanaka, H. (1999). On the mechanics and physics in the nano-indentation of silicon monocrystals. *JSME International Journal*, 42, 546-559.
- Zhang, L., Zhao, H., Ma, Z., Huang, H., Shi, C., & Zhang, W. (2012). A study on phase transformation of monocrystalline silicon due to ultra-precision polishing by molecular dynamics simulation. *AIP Advances*, 2(4), 042116-042116.
- Zhang, L. C., & Mylvaganam, K. (2009). Scale Effect of Nano-indentation of Silicon—A Molecular Dynamics Investigation. *Key Engineering Materials*, 389, 521-526.